



National Library
of Canada

Acquisitions and
Bibliographic Services Branch

395 Wellington Street
Ottawa, Ontario
K1A 0N4

Bibliothèque nationale
du Canada

Direction des acquisitions et
des services bibliographiques

395, rue Wellington
Ottawa (Ontario)
K1A 0N4

Your file Votre référence

Our file Notre référence

NOTICE

The quality of this microform is heavily dependent upon the quality of the original thesis submitted for microfilming. Every effort has been made to ensure the highest quality of reproduction possible.

If pages are missing, contact the university which granted the degree.

Some pages may have indistinct print especially if the original pages were typed with a poor typewriter ribbon or if the university sent us an inferior photocopy.

Reproduction in full or in part of this microform is governed by the Canadian Copyright Act, R.S.C. 1970, c. C-30, and subsequent amendments.

AVIS

La qualité de cette microforme dépend grandement de la qualité de la thèse soumise au microfilmage. Nous avons tout fait pour assurer une qualité supérieure de reproduction.

S'il manque des pages, veuillez communiquer avec l'université qui a conféré le grade.

La qualité d'impression de certaines pages peut laisser à désirer, surtout si les pages originales ont été dactylographiées à l'aide d'un ruban usé ou si l'université nous a fait parvenir une photocopie de qualité inférieure.

La reproduction, même partielle, de cette microforme est soumise à la Loi canadienne sur le droit d'auteur, SRC 1970, c. C-30, et ses amendements subséquents.

Canada

UNIVERSITY OF ALBERTA

CMOS ACTUATORS

BY

BING SHEN



A THESIS

SUBMITTED TO THE FACULTY OF GRADUATE STUDIES AND RESEARCH
IN PARTIAL FULFILLMENT OF THE REQUIREMENTS FOR THE DEGREE OF
DOCTOR OF PHILOSOPHY

DEPARTMENT OF ELECTRICAL ENGINEERING

EDMONTON, ALBERTA

SPRING 1996



National Library
of Canada

Acquisitions and
Bibliographic Services Branch

395 Wellington Street
Ottawa, Ontario
K1A 0N4

Bibliothèque nationale
du Canada

Direction des acquisitions et
des services bibliographiques

395, rue Wellington
Ottawa (Ontario)
K1A 0N4

Your file / Votre référence

Our file / Notre référence

The author has granted an irrevocable non-exclusive licence allowing the National Library of Canada to reproduce, loan, distribute or sell copies of his/her thesis by any means and in any form or format, making this thesis available to interested persons.

L'auteur a accordé une licence irrévocable et non exclusive permettant à la Bibliothèque nationale du Canada de reproduire, prêter, distribuer ou vendre des copies de sa thèse de quelque manière et sous quelque forme que ce soit pour mettre des exemplaires de cette thèse à la disposition des personnes intéressées.

The author retains ownership of the copyright in his/her thesis. Neither the thesis nor substantial extracts from it may be printed or otherwise reproduced without his/her permission.

L'auteur conserve la propriété du droit d'auteur qui protège sa thèse. Ni la thèse ni des extraits substantiels de celle-ci ne doivent être imprimés ou autrement reproduits sans son autorisation.

ISBN 0-612-10636-5

Canada

UNIVERSITY OF ALBERTA
RELEASE FORM

NAME OF AUTHOR: **BING SHEN**
TITLE OF THESIS: **CMOS ACTUATORS**
DEGREE: **DOCTOR OF PHILOSOPHY**
YEAR THIS DEGREE GRANTED: **1996**

PERMISSION IS HEREBY GRANTED TO THE UNIVERSITY OF ALBERTA LIBRARY TO REPRODUCE SINGLE COPIES OF THIS THESIS AND TO LEND OR SELL SUCH COPIES FOR PRIVATE, SCHOLARLY OR SCIENTIFIC RESEARCH PURPOSES ONLY.

THE AUTHOR RESERVES ALL OTHER PUBLICATION RIGHTS, IN ASSOCIATION WITH THE COPYRIGHT IN THE THESIS, AND EXCEPT AS HEREIN BEFORE PROVIDED NEITHER THE THESIS NOR ANY SUBSTANTIAL PORTION THEREOF MAY BE PRINTED OR OTHERWISE REPRODUCED IN ANY MATERIAL FORM WHATEVER WITHOUT THE AUTHOR'S PRIOR WRITTEN PERMISSION.

(SIGNED)



BING SHEN

BEIYUAN DAYUAN


ANWAI, BEIJING

P.R. CHINA

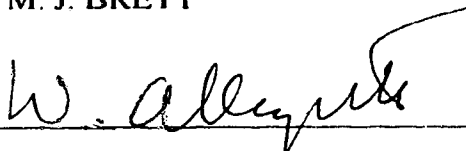
DATE: *Jan. 19, 1996*

UNIVERSITY OF ALBERTA
FACULTY OF GRADUATE STUDIES AND RESEARCH

THE UNDERSIGNED CERTIFY THAT THEY HAVE READ, AND RECOMMEND TO THE FACULTY OF GRADUATE STUDIES AND RESEARCH FOR ACCEPTANCE, A THESIS ENTITLED **CMOS ACTUATORS** SUBMITTED BY **BING SHEN** IN PARTIAL FULFILLMENT OF THE REQUIREMENTS FOR THE DEGREE OF **DOCTOR OF PHILOSOPHY**.


DR. A.M. ROBINSON (SUPERVISOR)


DR. M. J. BRETT


DR. W. ALLEGRETTO


DR. F. VERMEULEN


DR. K. STROMSMOE


PP DR. K. PISTER

DATE: 17 Jan 1996

Abstract

The static and dynamic characteristics of the thermally sensitive structures micro-machined by the standard CMOS processes were investigated. Thermal sensitivities of different structures were measured at ambient pressures of 1 atm and 10^{-4} Torr. Heat loss mechanisms were analyzed and methods to increase the thermal sensitivity discussed. For the dynamic response, the time-varying resistance of a microbridge device was measured under excitation by electrical current and power steps. The time-varying response for the device at 1 atm and in a vacuum were observed under a number of step amplitudes and the time constants of the device extracted. An analytic model was developed and its predictions were consistent with the observations from the experiments.

A magnetically actuated cantilever-type device was designed and tested. The device was fabricated using a standard CMOS process, and the design employed the novel concept of a cantilever-in-cantilever (CIC) structure to produce a large angular deflection. Actuation was initiated by Lorentz forces due to the interaction between currents flowing in the structure and an external magnetic field. The deflection of the device was measured and compared with the predictions of an analytic calculation. A static deflection of more than 2.5° has been achieved. The measurements of response time and frequency response were also performed. The triple CIC (structure containing three active cantilevers) has a measured response time of $25 \mu\text{s}$ and a resonant frequency of 17 kHz. At resonance its deflection can reach more than 25° .

Acknowledgements

I would like to express my sincere gratitude to my supervisor, Dr. A.M. Robinson, for his patience, encouragement and guidance throughout this research work. Special appreciation should be extended to Dr. W. Allegretto, Dr. M. Brett, Dr. K.A. Stromsmoe and Dr. T. Hruday for their enlightening discussions in various areas. Dr. R.P.W. Lawson has provided invaluable help and support during my entire graduate program, to which I am grateful.

I wish to acknowledge the financial support generously provided by the Alberta Microelectronic Centre (AMC). Special thanks to G. Mckinnon, T. Tran, G. Fitzpatrick, Y. Ning, Y. Loke, M. Paranjape, and C. Shafai for their instruction and assistance with the facilities at AMC, as well as for their helpful suggestions and advice. The Canadian Microelectronics Corporation (CMC) has played a key role to provide CMOS chips through out this project.

Visiting scholars from China, Professor Zongsheng Lai, Professor Ming Hu, and Bing Yu, have provided tremendous help which should be greatly appreciated. Constant technical assistance from R. Haley and J.R. Dawe has been an immense contribution to the success of my efforts.

I am also grateful to N. Jantz, Yanmin Li, Dr. X. Sun and Nelson Poon for their continuous support, and to R. Bobkowski, Yunlei Li, Ming Hu and Yuan Ma for providing SEM services.

I would also like to thank my volleyball team members, including Bing Xu, Sam Yan, Weijia Chen, Janet Luo, Limai Zou, Xiaoli Cheng, and Kelly Ma, for sharing those enjoyable memories.

Finally, my heartfelt gratitude goes to my wife and family for their willing support and help, especially during difficult times. This thesis is dedicated to them.

Contents

1	Introduction	1
1.1	Measurement Systems	1
1.2	Microtransducers and Micromachining	2
1.3	Thesis Overview	4
2	CMOS Bulk Micromachining	6
2.1	Bulk Silicon Micromachining	6
2.1.1	Wet Anisotropic Etching	6
2.1.2	Mask Patterning and Etching Undercut	7
2.1.3	Anisotropic Etchants	9
2.2	CMOS Technology	11
2.2.1	MOS transistors	11
2.2.2	CMOS Inverter	13
2.3	CMOS Micromachining	23
3	Thermally Sensitive Structures	27

3.1	Polysilicon	28
3.2	Functional Sensor Devices	30
3.2.1	Gas Pressure Sensor	31
3.2.2	Thermal Radiation Sensor	34
3.3	Thermal Sensitivity	39
3.4	Performance Improvement	41
4	Dynamic Characteristics Investigation	46
4.1	Experimental Setup and Procedure	46
4.2	Analytic Modeling for CC Operation	51
4.3	Results and Analysis	59
5	Movable Structures in CMOS Technology	65
5.1	Review of CMOS Fabricated Movable Structures	66
5.1.1	Sub-nanogram Mass Sensor	66
5.1.2	Electro-thermal Actuator	67
5.1.3	Thermally Excited Resonators	69
5.1.4	Thermally Activated Micromirrors	71
5.2	Magnetically Actuated Devices	78
5.2.1	Magnetic Actuation	78
5.2.2	Deflection Estimation	79
5.2.3	Deflection Enhancement – CIC Structure	85

5.2.4	Experiments and Analysis	92
5.2.5	Potential Applications	105
6	Conclusions and Outlook	107
6.1	Summary of Contributions	107
6.1.1	Thermally Sensitive Structures	108
6.1.2	Magnetically Actuated Device	109
6.2	Future Work	111

List of Tables

3.1	Characteristics of polysilicon from NT and Mitel CMOS processes	30
4.1	Measured time constants for response of CC excitation ($R_0 = 1.806k\Omega$)	61
4.2	Measured time constants for response of CP excitation ($R_0 = 1.806k\Omega$)	64
5.1	Mechanical properties of CMOS thin film materials	83
5.2	Frequency response of a triple-CIC structure ($I_{rms} = 8.0 mA$).	105

List of Figures

1.1	Basic components of a measurement system.	2
2.1	Crystallographic planes for a unit cube of silicon crystal.	7
2.2	Square opening in alignment with the wafer primary flat (vertical dimension has been exaggerated in the cross-sectional diagram). . .	8
2.3	Several opening designs and cavity boundary after isotropic etching.	10
2.4	Physical structures of MOS transistors.	12
2.5	Physical structures of CMOS inverter.	14
2.6	P-well process	15
2.7	N-guard process	15
2.8	Device well definition	16
2.9	P-guard process	17
2.10	Device well formation	17
2.11	Polysilicon masking and etching	18
2.12	N+ implantation process	19
2.13	P+ implantation process	19

2.14	Contact cut process	20
2.15	Metal-1 masking and etching	20
2.16	Via process	21
2.17	Metal-2 masking and etching	22
2.18	Passivation process, final inverter structure	22
2.19	CMOS suspended mass structure.	25
3.1	(a) Plan view of the suspended bridge. The polysilicon resistor is supported by a total of 20 oxide arms over the cavity etched in the silicon substrate. (b) Elevated view of the bridge.	32
3.2	Microbridge used as a gas pressure gauge (Pirani gauge).	33
3.3	Plan view of suspended platform.	35
3.4	Experimental setup for radiation sensor.	36
3.5	Microplatform as a radiation sensor.	37
3.6	Thermal sensitivity measurements under two ambient pressures.	40
3.7	Suspension arm serves as a thermal link.	42
3.8	Plan view of a platform with enhanced thermal sensitivity.	44
4.1	Experimental setup for measuring dynamic response.	47
4.2	Voltage measured across the microresistor under CC operation. Resistance is proportional to V . Current step occurs at $t=0$	49
4.3	Square of voltage measured under CP operation. Resistance is proportional to V^2 . Power step occurs at $t=0$	50

4.4	Differential section of the bridge structure.	52
4.5	Semilogarithmic response of the resistor under CC operation, obtained from data of Figure 4.2.	60
4.6	Variation of τ^{-1} with square of current step amplitude.	62
4.7	Semilogarithmic response of the resistor under CP operation, obtained from data of Figure 4.3.	63
5.1	Electro-thermal actuator structure.	68
5.2	Microbeam (cantilever) structure as a thermal excited resonator.	70
5.3	Plan view of thermally actuated CMOS micromirror.	73
5.4	Experimental setup for deflection angle measurement.	74
5.5	Mirror deflection versus the input current.	75
5.6	Mirror deflection variation with the average temperature of the driving beams.	76
5.7	A simple magnetic activated mirror device structure.	80
5.8	Cantilever deflection under concentrated force F (a) and concentrated moment M (b).	81
5.9	Cross section of the support arm: (a) original; (b) transformed.	83
5.10	SEM picture of a triple CIC device.	85
5.11	Triple CIC plan view and metal layers arrangement (in regions where metal1 and metal2 leads are side-by-side, they actually overlap each other in the real device).	86
5.12	Deflection estimation for triple CIC structure.	87

5.13	Temperature increase of support arms versus the input current.	93
5.14	Mirror tilt variation with the input current.	94
5.15	Photodetector arrangement for mirror response time measurement.	96
5.16	Photodetector output (upper trace) as mirror is excited by an AC square wave current at 102 Hz (lower trace).	97
5.17	Close-up look of Figure 5.16.	98
5.18	Triple CIC structure frequency response.	101
5.19	Double CIC structure frequency response.	102
5.20	Temperature increase of the support arms versus driven frequency.	104

Chapter 1

Introduction

1.1 Measurement Systems

There has been a need of gathering and processing information from the surroundings since the beginning of the human history. Instinctive information gathering is accomplished by sensing or measuring physical and chemical quantities in the environment using an assortment of measurement systems of the human body, such as sight, hearing, touch, smell and taste. These measurements are then processed by a neural system (the brain) and used to make decisions. However, due to its very nature, the information obtained by the human's biological measurement systems is subjective and qualitative. Thus instruments and tools which provide quantitative measurement systems have been designed and used. Today, a wide range of measurement systems that have a variety of uses could be found almost anywhere from the home to factory floor.

Figure 2.2.1 shows the basic components of a typical measurement system. The input signal to a measurement system is often called the *measurand* which is the physical or chemical quantity to be measured (e.g. pressure, radiation, tempera-

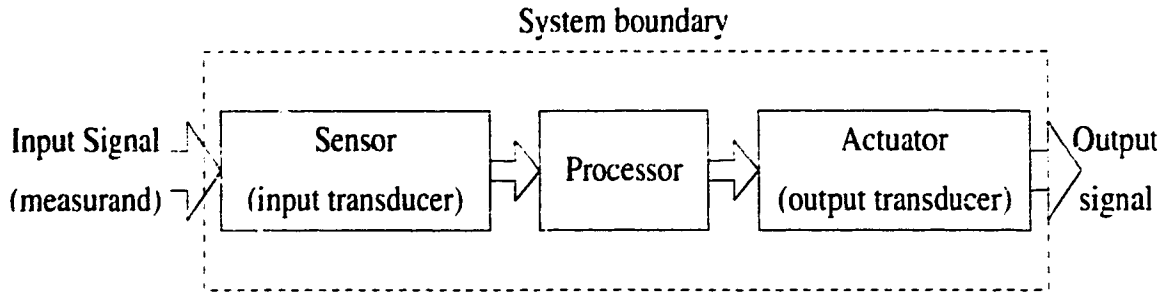


Figure 1.1: Basic components of a measurement system.

ture). The measurand is detected or sensed by an *input transducer* or *sensor*. A sensor is normally defined as a device that converts a non-electrical quantity into an electrical signal. Coming from the sensor, the electrical signal is conditioned and modified by the *processor* unit without changing the form of the energy that carries the signal.

Finally, the signal from the processor might be used to display information to a human operator. Alternatively, the signal might be recorded on some type of medium, or initiate some action for a process control system. Any such device that converts an electrical signal into a quantity of another form will be referred to as an *actuator* or *output transducer*. For example, the presentation of information over a loud speaker requires the conversion of an electrical signal into an acoustic signal and is thus an actuating process.

1.2 Microtransducers and Micromachining

The transducer plays an important role in our industrial and personal lives. A large transducer may have excellent operating characteristics but, nevertheless, its marketability and applicability could be severely limited simply by its size. For

example, it is difficult to perform image collecting using a photo-multiplier. A reduction in the size of a transducer often leads to an increase in its applicability through:

- lower weight (greater portability);
- less effect on measurand (higher measurement accuracy);
- faster response;
- lower manufacturing cost;
- higher packing density leading to wider range of applications.

A microtransducer is differentiated from its large counterparts not only by its small size but by the techniques used in its manufacturing. It is often formed by fabrication technologies that have been used to build integrated circuits (IC). The process of fabricating such devices with very small dimensions (in the micrometer range) is often referred to as *micromachining* [1].

In terms of the various forms of its final products, micromachining technology can be classified as either *bulk micromachining* or *surface micromachining* [2]. Bulk micromachining, largely depending on the remarkable mechanical properties of single-crystal silicon [3], is usually performed by selectively etching crystalline silicon, and the micromechanical structures developed with this technology are made of either crystalline silicon or deposited or grown films on silicon. Surface micromachining, on the other hand, is a technique for fabricating three-dimensional micromechanical structures from multiple stacked and patterned thin films [4, 5, 6], on the surface of a silicon crystal.

Although the micromachining technology emerged from fabrication schemes of integrated circuits, standard IC processes have not been directly used for building

micromechanical structures until recent investigations pursued by Parameswaran *et al.* [7, 8, 9, 10]. In their approach, a standard CMOS (Complementary Metal Oxide Silicon) IC process is used as a primary micromachining process. Compared to conventional non-standard microfabrication methods, CMOS micromachining has the following advantages:

- A standard process is highly regulated and the process parameters are well-defined. Thus a high degree of reliability and repeatability could be offered to the structures built using the process.
- Through fabrication services, these commercialized processes could be easily accessed by research groups without complex fabrication facilities. In Canada, the CMOS process has been a readily available technology offered to universities by Northern Telecom Electronics Limited and Mitel Corporation, through the aegis of the Canadian Microelectronics Corporation (CMC).
- Supporting electronics has been a vital part of any transducer system. Using the standard IC process to fabricate transducers enables merging of IC circuits and micromechanical structures on the same chip, a requirement for building a “smart” or “intelligent” sensor [11].

1.3 Thesis Overview

CMOS micromachining has become a simple and yet powerful approach especially applicable for bulk micromachining. In spite of successful fabrication of several microsensors using CMOS technology[12, 13, 14, 15, 16]. CMOS micromachining is still at a preliminary development stage. Performance improvement and structure optimization of those devices would be the next and very critical step towards the commercialization of the technology. In addition, very little [15, 17]

has been done on any actuator (output transducer) applications which will require controlled displacement (movement) to accomplish the desired function, such as resonator, active (deflected) mirror, microspeaker and microscanner. This research is aimed at performance optimization of several thermally sensitive structures and an investigation on movable structures fabricated using CMOS technology.

“CMOS bulk micromachining” is the main fabrication scheme for all the devices discussed in this thesis. A variety of structures has been fabricated using the CMOS processes offered by Northern Telecom and Mitel. The project demonstrated the procedure for the microstructure development, including layout design, post processing, characteristics testing, numerical simulation and performance optimization. Applications of those devices have been explored in both the microsensor and microactuator areas.

After a brief introduction to a few transducer terminologies, Chapter 2 describes the fundamentals for CMOS micromachining starting from an introduction to the CMOS process as an IC process to the realization of micromechanical structures using the process. Several thermally sensitive structures built by the CMOS process are introduced in Chapter 3. Chapter 4 demonstrates time response testing on a micromachined structure and relates the experimental results to the material properties and gas pressure of the environment. Chapters 5 concentrates on the investigation of CMOS micromachined movable structures and their applications, while conclusions are drawn in Chapter 6.

Chapter 2

CMOS Bulk Micromachining

2.1 Bulk Silicon Micromachining

Bulk silicon micromachining is the technique of fabricating well-defined three-dimensional micromechanical structures out of silicon, polysilicon and silicon oxides and nitrides. Wet anisotropic etching has become the core process of this technology.

2.1.1 Wet Anisotropic Etching

Wet anisotropic etching is a process of preferential directional etching of material using liquid etchants. The principle of anisotropic etching is based on crystallographic-orientation-dependent etching rates. To explain the phenomenon, a look at the silicon crystal is necessary.

Figure 2.1 displays a unit cube of silicon crystal in which the shadowed areas represent the three important crystallographic planes. Miller indices, corresponding to the smallest integer values which represent the reciprocal distance from the origin

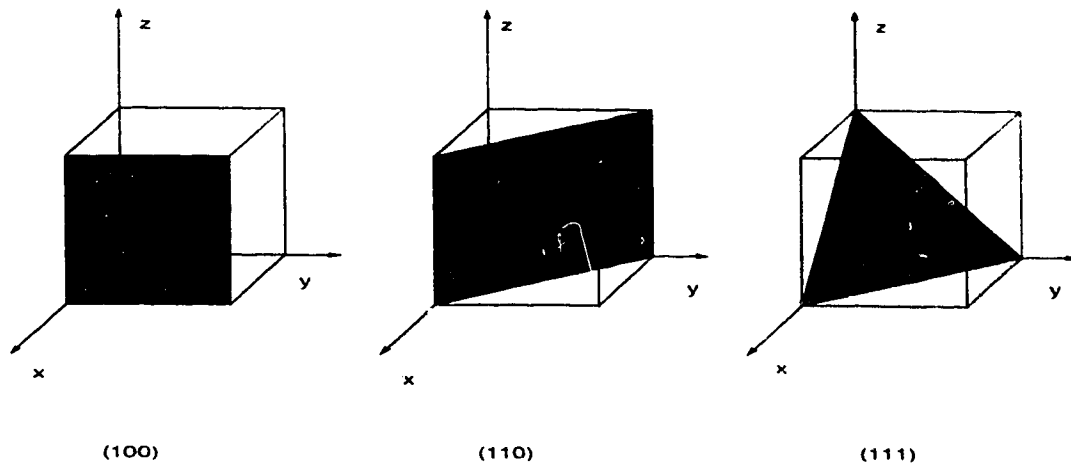


Figure 2.1: Crystallographic planes for a unit cube of silicon crystal.

to intersection of the plane through the three axes, are often used to describe those planes. The three planes shown in Figure 2.1 are named, from left to right, (100), (110) and (111) respectively. The atoms inside the silicon crystal are distributed in such way that the (111) plane exhibits the highest density of atoms per unit area and it determines the orientation of slowest etching.

Silicon wafers are available in three common orientations, namely $\langle 100 \rangle$, $\langle 110 \rangle$ and $\langle 111 \rangle$. The brackets “ \langle ” and “ \rangle ” are used to flag that the indices are for wafer orientations. It should be noted that the bracketing convention can vary between different literatures. Nevertheless, the most frequently used convention is that (abc) represents a particular crystal plane whereas $\langle abc \rangle$ denotes the group of vectors equivalent by crystal symmetry.

2.1.2 Mask Patterning and Etching Undercut

Before etching, silicon wafers have to be covered by a layer of mask (often made of silicon oxide or nitride) and the mask has to be patterned to make certain

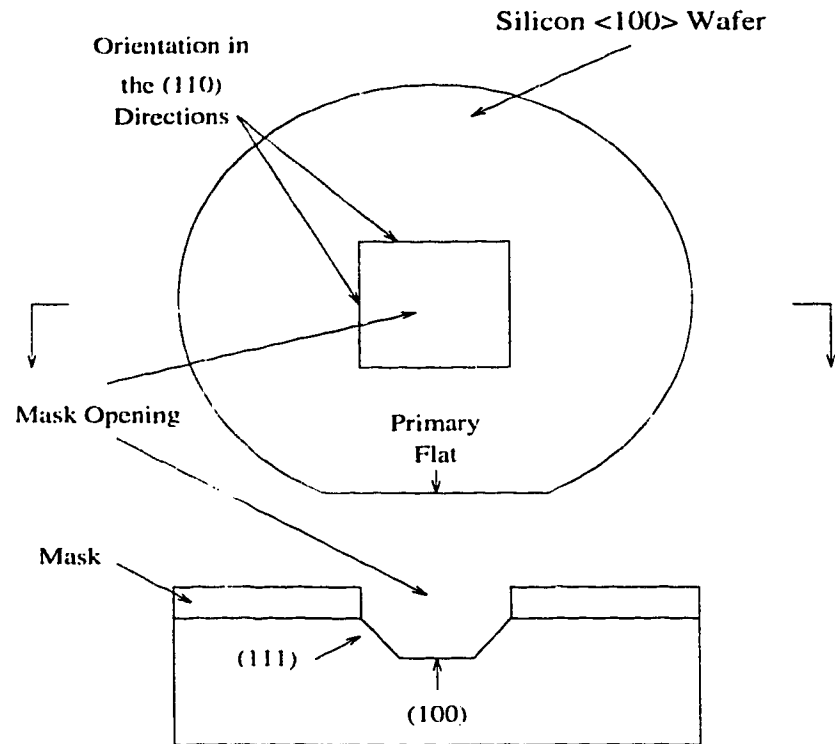


Figure 2.2: Square opening in alignment with the wafer primary flat (vertical dimension has been exaggerated in the cross-sectional diagram).

areas (openings) of the silicon substrate exposed to the etchant. The geometry of three-dimensional structures etched through the openings in a mask depends on the shape and the orientation of the opening itself. Discussions about the relationship between the mask opening and etched geometry will be concentrated on $\langle 100 \rangle$ -oriented wafers since $\langle 100 \rangle$ wafers are exclusively used for CMOS circuit fabrication.

Figure 2.2 illustrates the anisotropic etching profile as a square mask opening is in alignment with (110) orientations. The primary flat on the wafer indicates the (110) orientation of the crystalline silicon. In the situation displayed, the edges of

the etched pit almost coincide with the mask opening edges. It should be noted that the etchant will attack the (111) plane and make the pit size slightly larger than the mask opening. However, if the opening edge is not aligned to the (110) orientation, or the primary flat, *undercutting* of the mask, that is, substrate etching under the mask, will occur until the (111) plane is encountered. Also, any mask opening containing a convex corner will cause undercutting of the region beneath the mask. Undercutting plays a key role in the fabrication of any suspended microstructure. All the structures discussed in this thesis are built using undercutting. Figure 2.3 shows numerous mask opening shapes, orientations and the etched cavity boundaries after a prolonged time of anisotropic etching. The undercutting effect caused by attacking the (111) plane is also presented. It can be easily understood that the non-open regions overlapped by the cavity areas will form the suspended structures. For example, Figure 2.3 (a) is a cantilever structure, (b) is a suspended microbridge (c) forms some arbitrary shaped structures suspended over a square cavity, and (d) shows a platform supported by four arms. It should be noted that there are some design pitfalls which are often easily overlooked by a beginner. The opening location shown in Figure 2.3 (e) will not form a suspended platform and the bridge will not be released from the design of Figure 2.3 (f). Detail discussions on the layout design rules for microstructure fabrication in standard CMOS technology can be found in reference [18].

2.1.3 Anisotropic Etchants

Several anisotropic chemical etchants are used for single crystal silicon, such as EDP (ethylenediamine- pyrocatechol-water) [19, 20], TMAH (tetramethylammonium hydroxide) [21], and KOH (potassium hydroxide-water) [19]. They are composed of a primary component (ethylenediamine, tetramethylammonium, potassium hydroxide), a complexing agent (pyrocatechol), and a diluent (water).

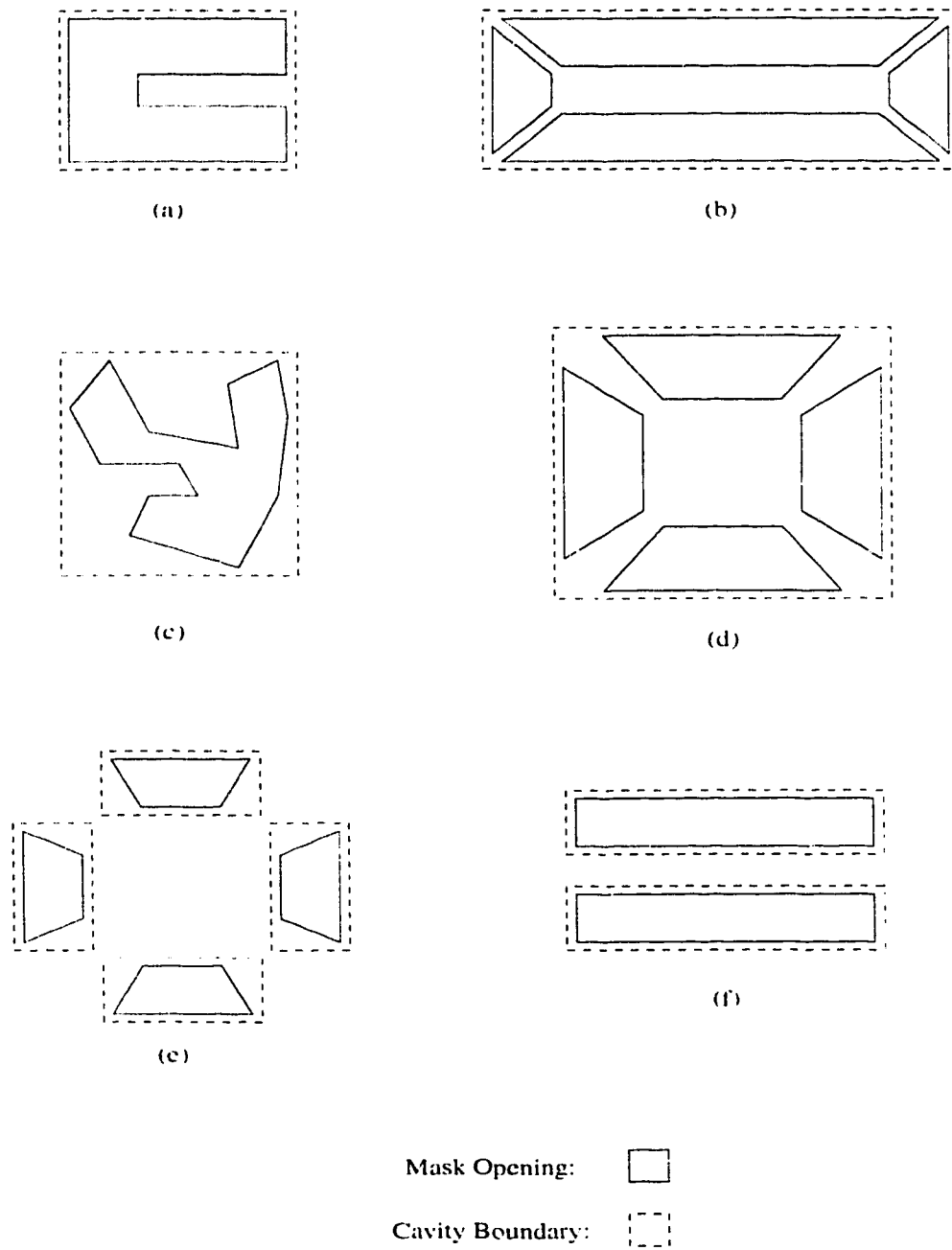


Figure 2.3: Several opening designs and cavity boundary after isotropic etching.

Anisotropic etchants can be highly material selective, which indicates that they may be masked by different materials (silicon dioxide, silicon nitride, chromium, gold and so on). For example, EDP does not attack gold, chromium, silver, or tantalum; and the etch rate of silicon dioxide and silicon nitride is extremely low compared to silicon [3]. However, EDP may attack aluminum. Tetramethylammonium hydroxide (TMAH) also shows higher selectivity to silicon oxide and silicon nitride allowing either to be used as a mask material. A disadvantage of a potassium hydroxide solution is that it etches silicon oxide much faster than the anisotropic silicon etching. It is not feasible to use silicon dioxide alone as a masking material when using KOH [3]. Another interesting silicon etchant used in CMOS micromachining is xenon difluoride (XeF_2). It is a gas phase, room temperature, highly selective isotropic etchant. Detailed discussions in this regard can be found in references [98, 99]. The etchant used in this project is EDP at a temperature of 110°C. The typical etch time is approximately one hour.

2.2 CMOS Technology

Over the past ten years, CMOS integrated circuits have become a mainstream technology for VLSI system design. This section will give a brief review of this technology, starting from an introduction of a MOS transistor to the formation process of a simple CMOS inverter.

2.2.1 MOS transistors

MOS is a name describing the actual structure of a special transistor. It is created by superimposing several layers of conducting (Metal), isolating (Oxide), and transistor forming materials (Silicon or Semiconductor). There are two types of

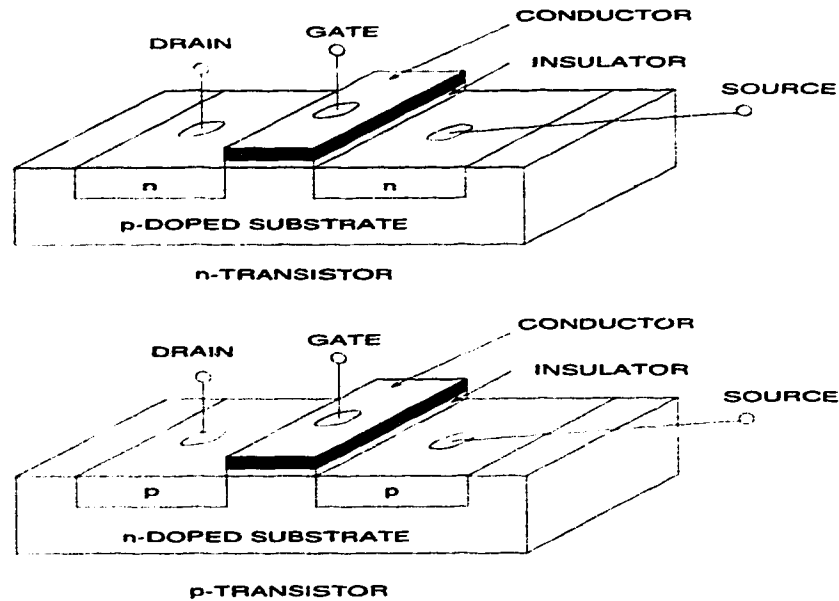


Figure 2.4: Physical structures of MOS transistors.

MOS transistors, namely the n-type (nMOS) transistor and the p-type (pMOS) transistor. These are fabricated in silicon by using either negatively doped silicon that is rich in electrons or positively doped silicon that is rich in holes. Their typical structures are shown in Figure 2.4.

Both transistors have at least three terminals, namely *drain*, *gate* and *source*. As illustrated by Figure 2.4, oppositely doped silicon between the drain and source stops any current flow between them. However, if an appropriate voltage is applied to the gate, a portion of silicon substrate under the gate conductor will be changed into the same type of doping as that forming drain and source, providing a conduction path (channel), and the transistor is turned “*on*”. An opposite polarity voltage applied to the gate, on the other hand, prevents conduction between the source and drain from happening and turns “*off*” the transistor.

pMOS and nMOS transistors perform oppositely in terms of the gate control volt-

age and transistor on/off state. For the purpose of convenience, the symbol “1” will be assumed to be the high voltage that is normally called *power* or V_{DD} . The “0” will be a low voltage, often called *ground* or V_{SS} . An nMOS transistor is turned on if there is a “1” on the gate. A “0” on the gate will turn off the transistor. For a pMOS transistor, however, a “0” on the gate ensures electrical connection between its source and drain. The transistor is turned off when there is a “1” on the gate.

2.2.2 CMOS Inverter

The term Complementary MOS, or CMOS, denotes the technology of fabricating both nMOS and pMOS transistors on the same silicon substrate. CMOS processing is optimized to accomplish superb performance for integrated circuits. This section will provide a brief overview of CMOS technology, with a simplified treatment of the process steps to form an inverter.

Figure 2.5 shows how to build a CMOS inverter using a nMOS transistor and pMOS transistor. Using the properties of MOS transistors discussed in the previous section, it is not difficult to find out how the inverter functions by examining the electrical connections in Figure 2.5.

One of the popular CMOS technologies is named the *P-well process*. A common approach to P-well CMOS fabrication has been to start with a moderately doped n-type silicon substrate (wafer), create the p-type well for the nMOS devices, and build the pMOS devices in the native n-substrate. Figure 2.6 to figure 2.18 illustrate the major steps involved in a P-well CMOS process offered by Northern Telecom. The mask that is used in each process step is shown in addition to a sample section of wafer containing an inverter. The real processing steps are somewhat complex and variations of the CMOS process exist. The following processing

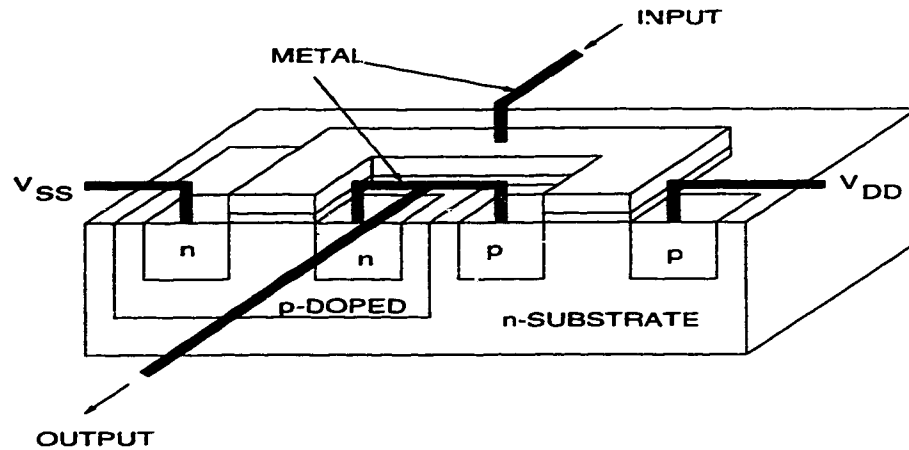


Figure 2.5: Physical structures of CMOS inverter.

step descriptions serve merely as an illustration.

- Oxidation forms a layer of silicon dioxide (SiO_2) which acts as a masking layer for the silicon underneath. The first photolithographic process removes the SiO_2 in a specific region, defined by a *P-well* mask, to expose the n-type silicon. An ion-implantation is performed to form a P-doped silicon section with depth of about 5-10 μm . The structure is also called P-well as shown in Figure 2.6.
- After removing the oxide, a photoresist (PR) layer is deposited on the wafer surface. Another photolithographic process uses an *N-guard* mask to pattern the PR layer, which permits an N-implant in certain areas, as shown in Figure 2.7.
- A thin SiO_2 layer (thinox), which will function as the gate insulator, is grown over the exposed silicon surface.
- The PR is removed and a layer of silicon nitride Si_3N_4 is deposited on the thinox and patterned using the *device well* mask. This photolithographic

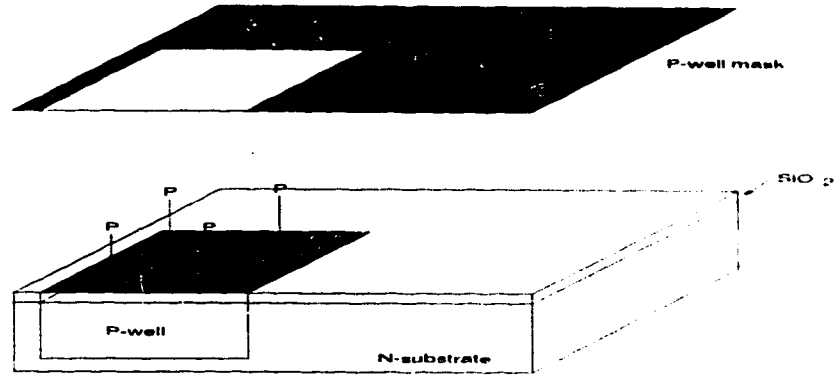


Figure 2.6: P-well process

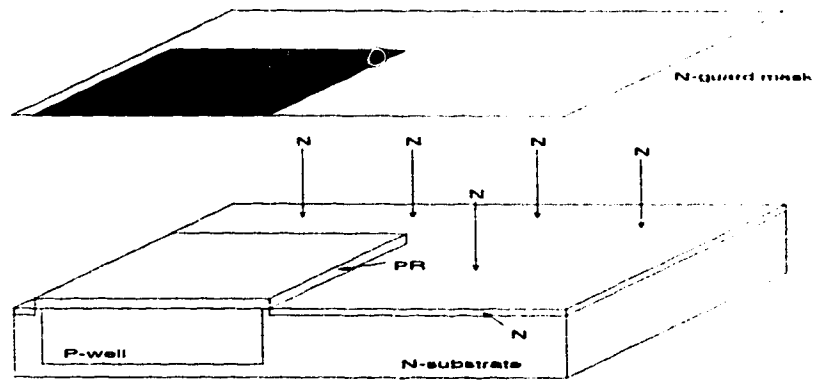


Figure 2.7: N-guard process

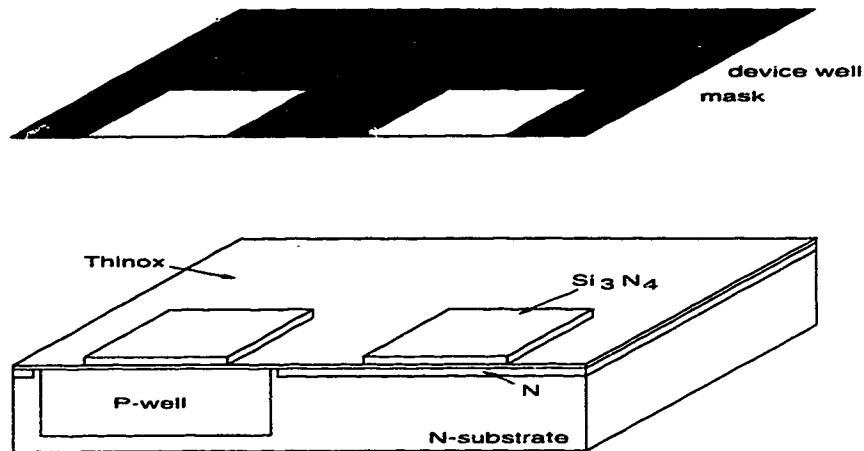


Figure 2.8: Device well definition

step, as sketched in Figure 2.8, leaves the dielectric sandwich only in regions which will become drains, sources, channel regions and diffusion interconnects. The sandwich is used to mask these regions from the next processing step, a P-implant into the P-wells. It also defines the regions of subsequent field oxide growth.

- Another PR layer is deposited and patterned using the *P-guard* mask as shown in Figure 2.9. The P-guard mask indicates the area where P-implant should occur. Following this step, the PR is removed again and thick oxide (field oxide) is grown on the regions where the nitride does not exist. The removal of nitride after that produces a structure as shown in Figure 2.10.
- With a thin oxide gate insulator layer over all active regions, the polysilicon gate layer is deposited over the entire surface and doped N^+ . The “+” here denotes the high doses that exceed $10^{15}/cm^2$. The next photolithographic process, shown in Figure 2.11, uses the *polysilicon* mask to define the gate regions and interconnections.
- A N^+ exclusion mask is used to *prevent* the N^+ doping from getting into

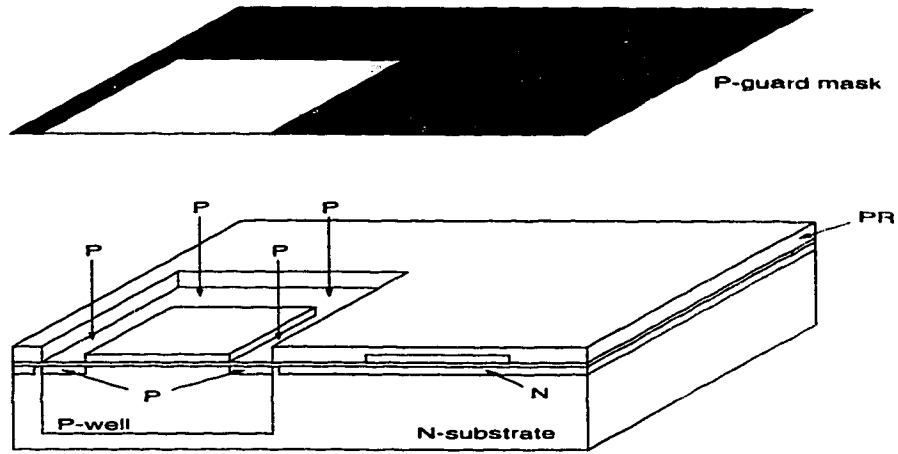


Figure 2.9: P-guard process

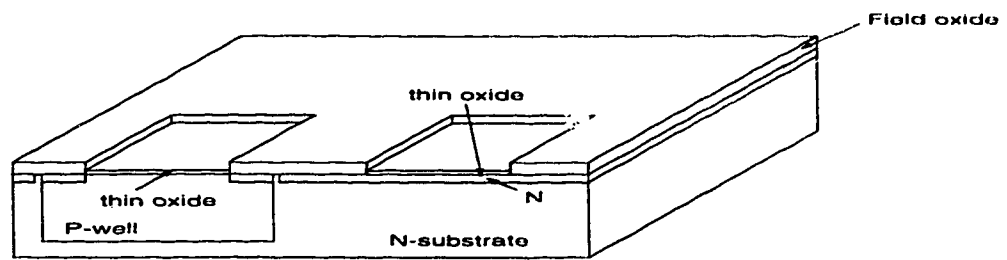


Figure 2.10: Device well formation

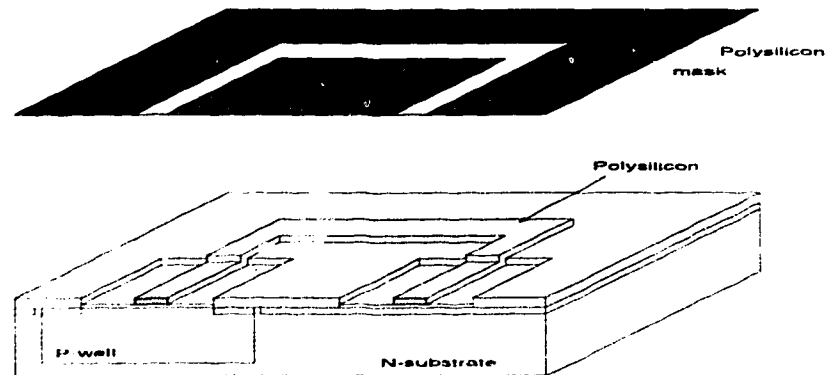


Figure 2.11: Polysilicon masking and etching

P-device regions. Figure 2.12 shows three N^+ regions formed by this photolithographic operation: the source and drain regions of the N-device within the P-well, and a contact region in the N-substrate.

- The source and drain regions of the P-device and substrate contact region in the P-well are defined by P^+ mask. The result is illustrated in Figure 2.13.
- A moderately thick layer of SiO_2 is deposited over the entire surface and the *contact* mask is used in a photolithographic operation to etch out the contact region for the next metallization process (Figure 2.14).
- A layer of aluminum is deposited over the entire surface and the *metal1* mask is used in a photolithographic process to create the conducting lines. The masking and etching is shown in Figure 2.15.
- Another layer of SiO_2 is deposited over the entire surface and the *via* mask is used to etch out the via regions to connect metal1 to metal2, as shown in Figure 2.16.
- The second layer of aluminum is evaporated over the wafer and the *metal2*

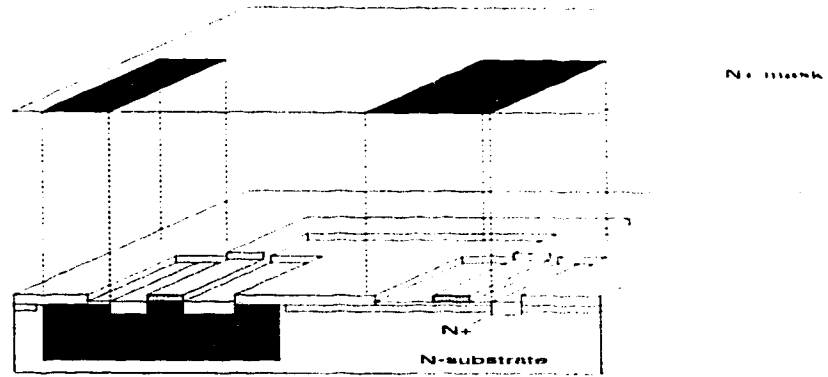


Figure 2.12: N+ implantation process

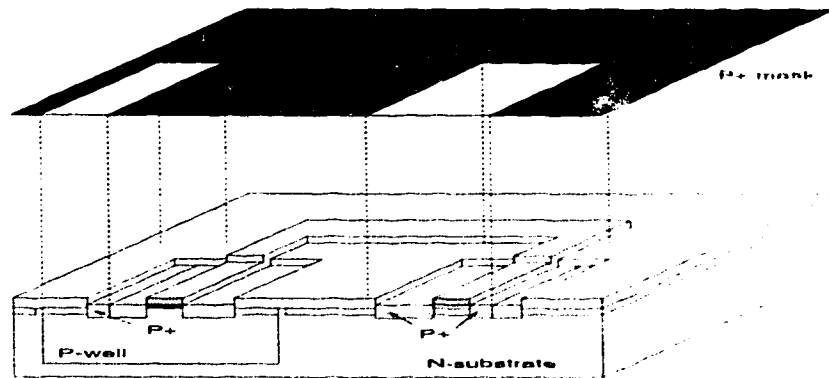


Figure 2.13: P+ implantation process

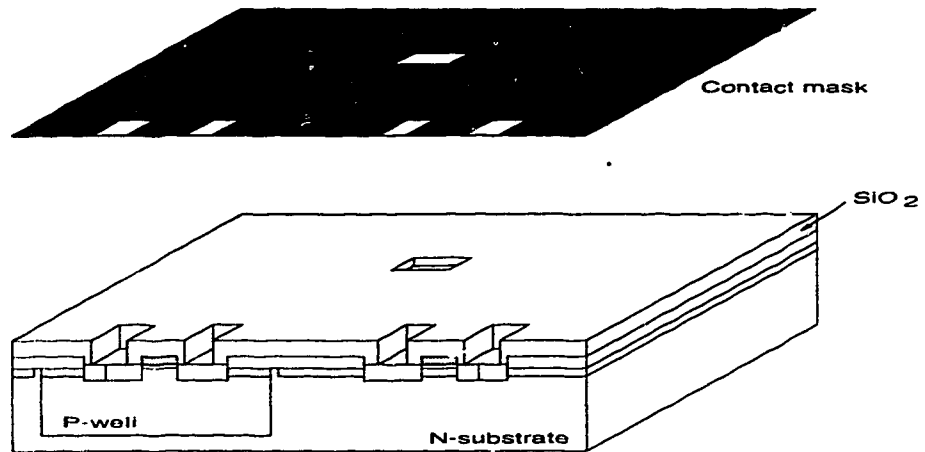


Figure 2.14: Contact cut process

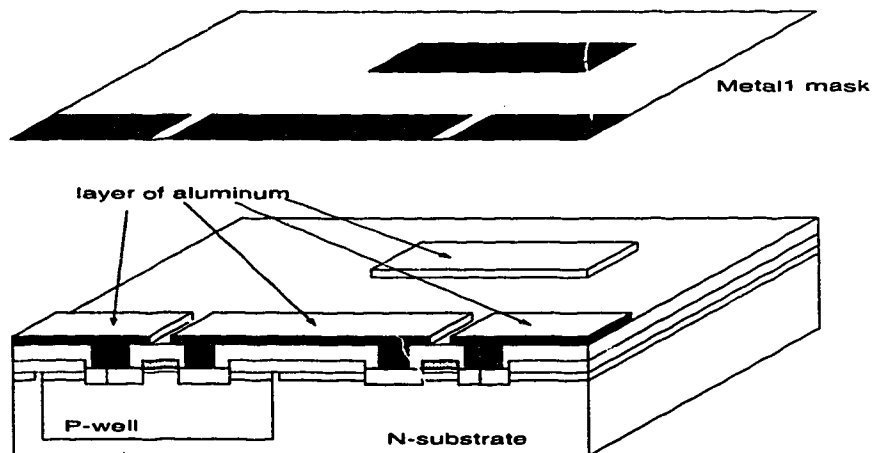


Figure 2.15: Metal-1 masking and etching

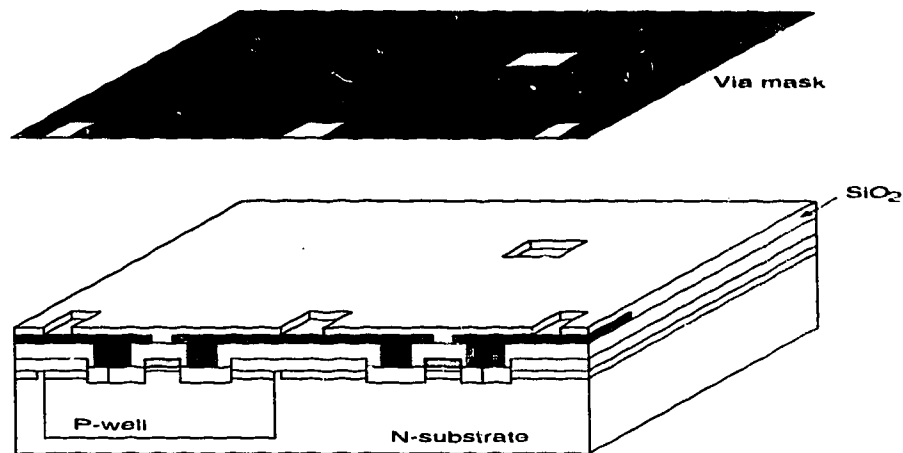


Figure 2.16: Via process

mask is used to define the metallization lines and pads (Figure 2.17) that make the circuit accessible to the outside world.

- Finally a dielectric layer is deposited over the entire surface and the *passivation* mask is used to etch out regions over the metal bonding pads and probe pads. The complete structure for a CMOS inverter, fabricated using P-well CMOS process, is shown in Figure 2.18.

The masks used in the process are sometimes referred as layers. Since the process itself has been standardized, the task of IC layout design is to specify the lateral size, shapes and locations of these layers. Some of the process steps above, such as N-guard and P-guard formations, are not directly related to construction of the inverter shown in Figure 2.5. They are included to enhance the performance of integrated circuits. Detailed discussion regarding their functions can be found in reference [28].

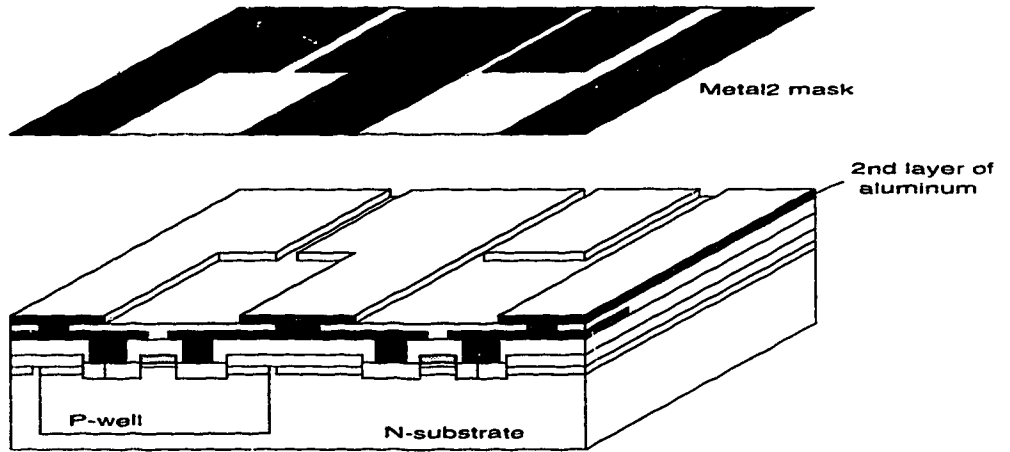


Figure 2.17: Metal-2 masking and etching

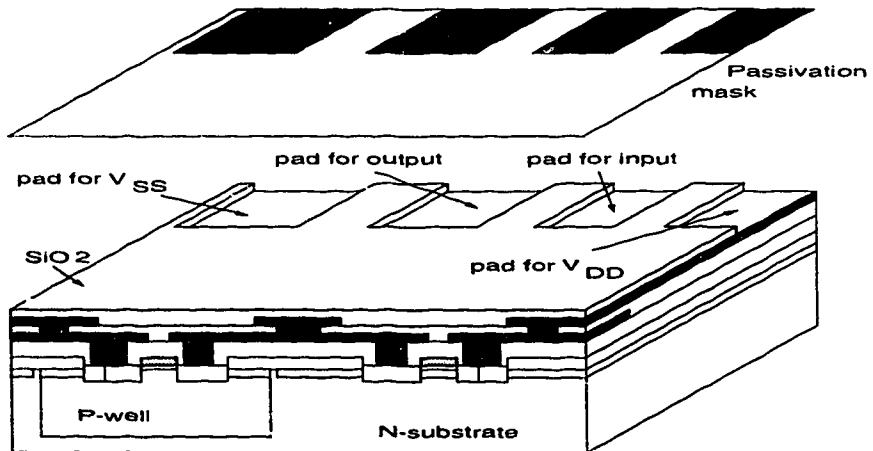


Figure 2.18: Passivation process, final inverter structure

2.3 CMOS Micromachining

The brief introduction on the CMOS process in the previous section immediately reveals that the key elements relevant to bulk micromachining, such as $\langle 100 \rangle$ wafer orientation, dielectric layers, polysilicon and other thin films, are already present. The only step left is to create micromechanical structures by anisotropic etching of the silicon substrate, a process not included in standard CMOS, but one which can be done as a *postprocessing* add-on step without changing the standard process.

As discussed in Section 2.1.2 and reference [18], a successful anisotropic etching depends largely on the shapes and location of openings on the substrate. Conventionally, there are no regions of substrate exposed for an IC wafer fabricated using the CMOS process. However, because the patterns of thin films stacked on the top of the substrate are controlled by layout design, there is a way to create an opening on the substrate by making all the films absent at that region. Examination of the CMOS process in the previous section shows that an opening can be formed by stacking, in the layout design, device well, contact cut, via, and passivation layers together, resulting in no layers being deposited at these locations in the fabricated wafers.

Once the open regions are successfully defined and fabricated, the shapes and structures of the mechanical devices are just a matter of design and imagination. Generally, polysilicon and metal can be used as the active parts of the micromechanical device; parts such as: sensing element, electrical conductor, heating resistor, and optics mirror. They are usually protected and supported by dielectric layers forming so-called “sandwiched” structures. Manipulation of layout design also permits some degree of thickness control over some multilayer structures by subtracting certain layers from the device.

There has been a variety of mechanical structures fabricated using standard CMOS processes, such as cantilever, bridge and suspended platform. Those devices can measure gas flow [12] and pressure [36, 37] or be used as actuators [15]. Their operations are based on the thermal isolation achieved by the postprocessing etching. The next chapter will be devoted mainly to this type of structure. Some efforts have been made on fabricating movable CMOS mechanical structures with applications like resonators or nano-gram mass sensors. Detailed discussions in this regard can be found in Chapter 5 of this thesis. Using the same approach, many other complex structures have also been fabricated. An example of a suspended mass is shown in Figure 2.19 [2]. This structure was fabricated in a twin-well CMOS process. The support arms that keep the central mass suspended are spiral-like, making the structure very flexible and sensitive to any acceleration.

Another interesting application for CMOS micromachining is to fabricate a high quality inductor for the development of an RF amplifier [2]. Inductors are the key components of an RF amplifier because they are used as a tuned load to obtain a desired gain and to filter band signals and noise [38]. The conventional spiral-structured integrated inductor is not suitable for the purpose because high parasitic capacitance to the substrate precludes its use at high frequency, and the series spreading resistance in the substrate severely limits its quality factor (Q). Both problems can be solved by etching a cavity below the inductor. It has been reported [2] that the inductor's self-resonance frequency was increased from 800 MHz to 3 GHz, by forming a cavity beneath the inductor. As a result, a fully integrated RF amplifier was implemented to achieve a peak gain of 14 dB at 770 MHz. For comparison, the amplifier using an inductor with no cavity can only yield a peak gain of 5 dB at 400 kHz.

To summarize, the combination of the IC CMOS process and micromachining or microfabrication offers a novel and economical approach toward future integrated

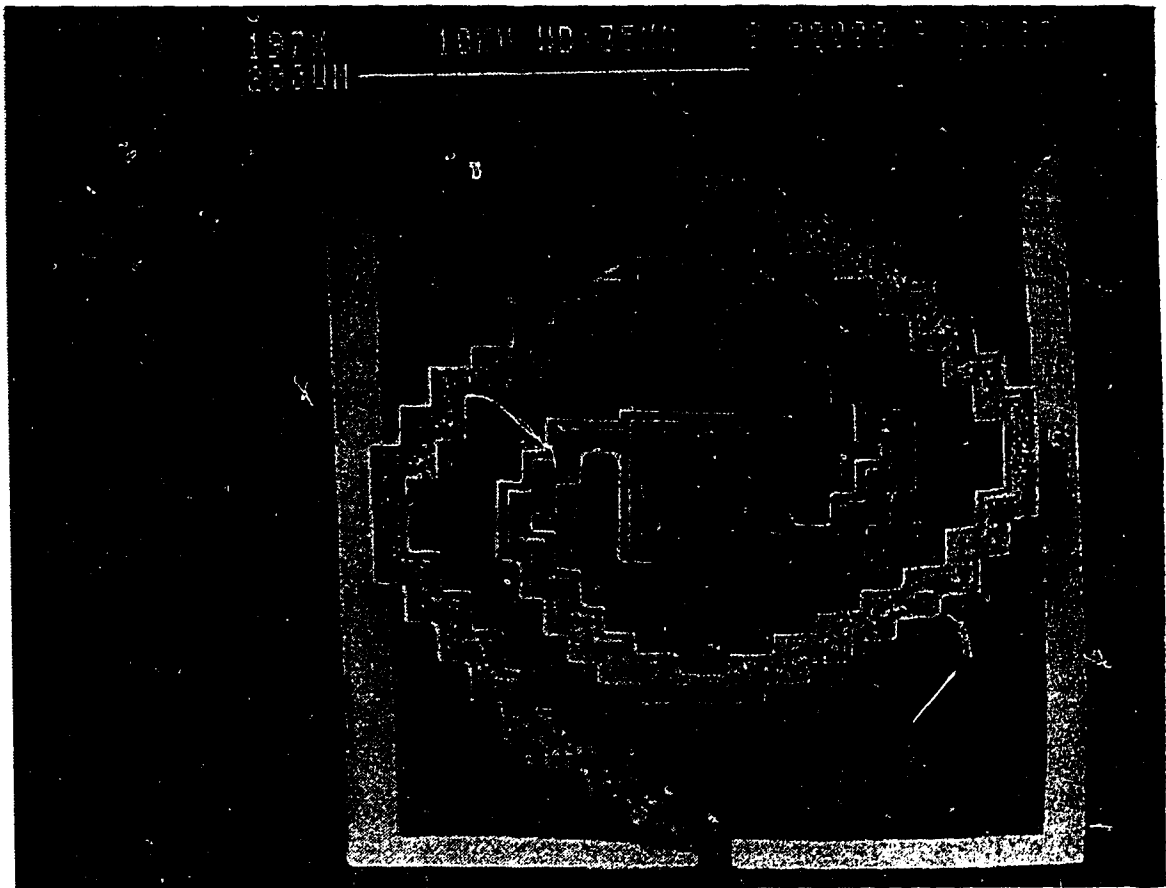


Figure 2.19: CMOS suspended mass structure.

systems with the merger of optical, mechanical and electrical components. The full potential of this special scheme remains unknown and needs further systematic investigation.

Chapter 3

Thermally Sensitive Structures

Electronic temperature sensing is a mature technology. Well known thermal characteristics of bipolar diodes [22] and transistors [23] have often been used to build IC temperature sensors. CMOS temperature sensors have also been achieved by either building a lateral bipolar transistor [24, 25, 26] or utilizing the thermal properties of a MOS transistor and resistor [27]. All the sensors mentioned above are used for temperature measurement. CMOS micromachining, however, offers an opportunity to fabricate thermally isolated micromechanical structures with the temperature sensing element embedded. The technology extends the applications of an ordinary temperature sensing to the following areas:

- The thermally sensitive structures can be used for indirectly sensing measurands other than temperature, such as gas pressure, radiation, and gas flow. The thermally sensitive structures will convert those measurands into temperature variation which in turn will be detected by the temperature sensing element.
- The thermally sensitive structures can be used as actuators as well. For example, micro-hot-plate and micro-radiation emitters can be constructed

to convert an electric signal into thermal energy [39] or radiation emission [45].

3.1 Polysilicon

Originally, the gate electrode of a MOS transistor was made of metal, just as the name “MOS” implies. In modern CMOS technology, however, most of gate electrodes are made of *polycrystalline* silicon, also called polysilicon or simply poly. The most significant aspect of using polysilicon as the gate electrode is its ability to be used as a further mask to allow precise definition of source and drain electrodes. Using the p-well process described in Section 2.2.2 as an example, undoped polysilicon is deposited on the gate insulator. Polysilicon and source/drain regions are then doped at the same time. The achieved minimum gate-to-source and gate-to-drain overlap will improve circuit performance [28]. In CMOS ICs, polysilicon is also used as interconnect, resistor element, and one or both plates of a capacitor.

Polysilicon plays a key role on CMOS micromachined structures and is often chosen to make active elements because:

- It is available in almost any CMOS and BiCMOS processes;
- It is usually sandwiched inside dielectric layers and is thus protected from postprocessing etching;
- Its electrical resistance varies with temperature [29, 30, 31] and is a natural temperature sensing element for sensor applications;
- It has reasonable resistivity and can be used as an electrical heater resistor.

The electrical resistance of a polysilicon layer (or any other thin film material) is often expressed by a parameter called *sheet resistance*, which can be defined as the resistance of one square block of film layer. The mathematical equation for sheet resistance R_s is:

$$R_s = \rho/t \quad (3.1)$$

in which ρ denotes the material resistivity and t the film thickness. Units of R_s are usually quoted in Ω/\square . Thus the resistance of a rectangular layer can be obtained by simply multiplying the sheet resistance R_s , by the ratio of the length to width of the resistor.

The most important parameter of polysilicon used as a temperature sensing element is its *temperature coefficient of resistance (TCR)*. The defining equation for the TCR is:

$$R(T) = R_0[1 + \alpha(T - T_0)] \quad (3.2)$$

where $R(T)$ is resistance at temperature T , R_0 is resistance at reference temperature T_0 (room temperature resistance is often used here), and α is the TCR.

Equation (3.2) permits a determination of temperature T provided R_0 , T_0 and α are known and R can be experimentally measured. This forms the fundamental use of such a material as a temperature sensing element.

The characteristics of lightly doped polysilicon resistors has been investigated carefully [29, 30]. However, most of polysilicon used in the CMOS process is highly doped and the typical doping density is approximately $10^{20}/cm^3$. Its electrical and thermal properties are very process-dependent because they are very sensitive to both the doping concentration and the thermal process history [31]. Thus it be-

Table 3.1: Characteristics of polysilicon from NT and Mitel CMOS processes

	R_s (Ω/\square)	α ($10^{-3}/^{\circ}C$)	T_{cr} ($^{\circ}C$)
NT Poly1	14 ± 2	1.15	~ 350
NT Poly2	38 ± 4	-2.0	< 100
Mitel Poly1	20 ± 2	1.10	~ 350
Mitel Poly2	100 ± 10	0.18	~ 450

comes necessary to investigate characteristics of polysilicon for individual CMOS processes.

For the Northern Telecom 1.2 μm and Mitel 1.5 μm CMOS processes, the resistance and the TCR of the polysilicon layers and the stability of both under actual operating conditions have been systematically studied [32, 33]. Both processes have two layers of polysilicon, namely poly1 and poly2. The poly1 layer serves as the gate electrode and the interconnects while poly2 layer is used as the top plate of an IC capacitor. Table 3.1 shows the testing results for these two processes. In the table, T_{cr} is the *critical temperature*, above which the resistance was not reversible with respect to temperature. Provided the temperature was kept below this value, good stability and repeatability for resistor thermal properties were observed [32]. The negative TCR value of NT poly2 resistor may be due to the light doping concentration for this particular layer.

3.2 Functional Sensor Devices

As the first generation of CMOS micromachined structures, a variety of thermally sensitive structures have been developed for sensor and actuator applica-

tions [12, 15, 17, 34, 35]. This section will illustrate how the thermally sensitive structures, in combination with temperature sensitive polysilicon resistors, could be used as sensors by describing the operating principles of two commonly used thermal sensors.

3.2.1 Gas Pressure Sensor

The CMOS micromachined pressure sensor is operated on the principle of the thermal conductivity gauge [36, 37], historically called the Pirani gauge. The temperature of a current-heated wire depends on the loss of energy due to the thermal conductivity of the surrounding gas. The thermal conductivity gauge detects the temperature variation by measuring the resistance change of the wire [40]. Thus the hot wire in a Pirani gauge is usually made of high TCR metal, such as platinum, tungsten or nickel. Polysilicon, however, has been used as the hot-wire material in the standard CMOS micromachined Pirani gauge, because it is readily available and it has a TCR as discussed in the previous section.

The device discussed here is a suspended bridge structure fabricated by the CMOS process offered by Northern Telecom. An isotropic etching was performed to form a cavity under the suspended structure. Its final geometry is shown in Figure 3.1. The white and central shadowed areas of Figure 3.1 (a) represent the oxide bridge and polysilicon resistor, respectively. The dark triangular and trapezoidal regions indicate the areas of the exposed silicon substrate where the anisotropic etching occurs, forming the trench beneath the oxide bridge, as indicated in Figure 3.1 (b). The active element (hot wire), made of poly1 of the process, is sandwiched between the field and chemical vapour deposited (CVD) oxide layers.

The experimental setup consisted of a diffusion pump system and a bell jar where the sensor was placed. A constant current of 0.6 mA was passed through the gauge

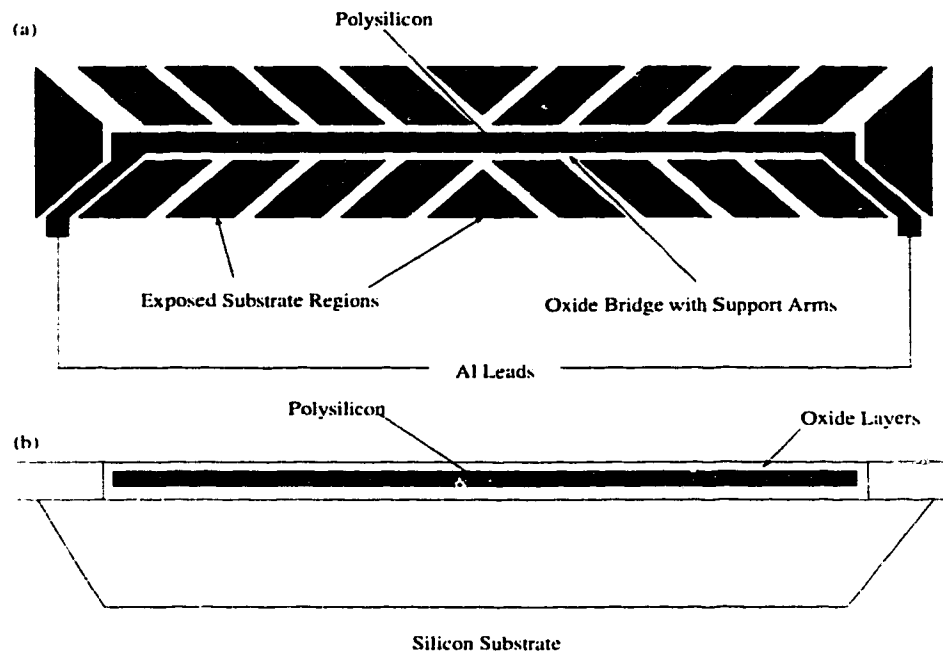


Figure 3.1: (a) Plan view of the suspended bridge. The polysilicon resistor is supported by a total of 20 oxide arms over the cavity etched in the silicon substrate. (b) Elevated view of the bridge.

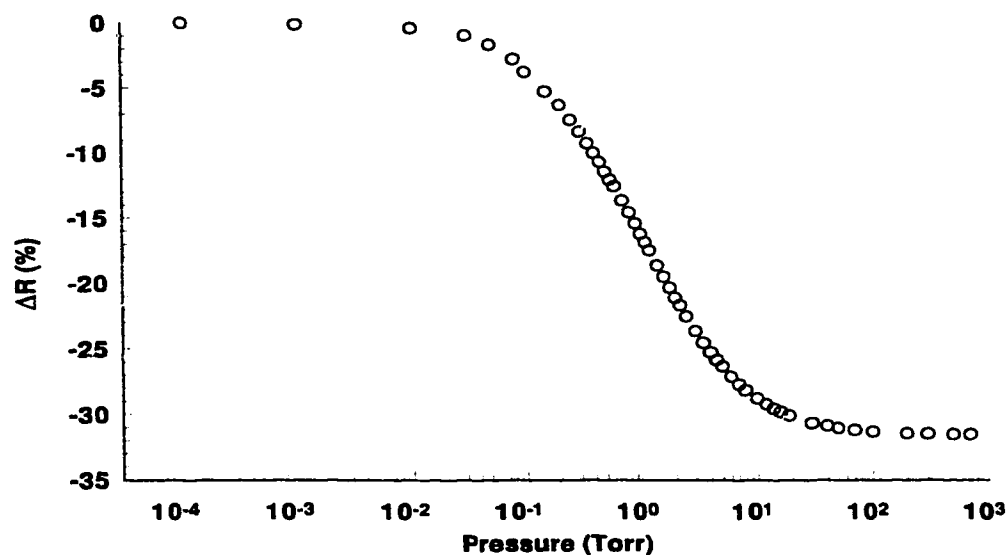


Figure 3.2: Microbridge used as a gas pressure gauge (Pirani gauge).

hot wire, and the voltages across the resistor were monitored by a data acquisition unit. Pressure in the bell jar was measured using a capacitance manometer at low pressures ($10^{-3} - 1$ Torr) and two diaphragm gauges at intermediate ($1 - 20$ Torr) and high ($100 - 700$ Torr) pressures. The procedure followed was to pump down the system below 10^{-3} Torr, isolate the pump, and then slowly bleed the gas into the bell jar. The controlled inflow rate was low enough to ensure that gas flow over the sensor element was negligible to avoid forced convective cooling. Voltages across the sensors were measured as the pressure increased to 1 atm.

Figure 3.2 shows the variation of sensor resistance at different pressures. The sensor resistance variation is represented by the percentage change of resistance, normalized at 10^{-4} Torr. The curve demonstrates the typical shape for a thermal conductivity pressure gauge. Above 100 Torr, where the thermal conductivity of

the gas is independent of pressure, the element temperature and therefore the resistance is almost constant. Below 0.1 Torr, the resistance is again independent of pressure because heat loss by conduction through the gas becomes very small. In the region between 0.1 and 100 Torr, the gas conduction heat loss tends to dominate and the resistance is a strong function of the gas pressure.

3.2.2 Thermal Radiation Sensor

Radiation sensors can be classified as non-contacting sensors because they detect remotely the emission of electro-magnetic radiation covering the spectral range from UV to infrared (IR). Based on their operating principles, radiation sensors can be conveniently divided into two classes: photon detector, such as photo-multiplier, photo-diode and photo-resistor, and pyroelectric detector, sometimes referred to as a thermal radiation detector, such as a thermal pyranometer. A photon detector absorbs the quantum energy of the incident radiation and the consequence of the energy exchange can be generation of a photocurrent, or variation of the resistance. The operation of a photon detector is characterized by excellent responsivity and a strong spectral dependence. It is usually sensitive to short-wave-length radiation due to the high energy a photon carries. The typical response time of a photon detector is several microseconds or less. A thermal radiation detector, however, measures the incident radiation by monitoring the temperature variation of its sensing element subjected to an incident radiation. Its sensitivity depends largely on the mechanical structure and radiation absorptivity of its sensing element. Contrary to the photon detector, a thermal radiation sensor is almost spectrally independent and its response range can easily be extended to the infrared. Its response speed is much slower than that of the photon detector.

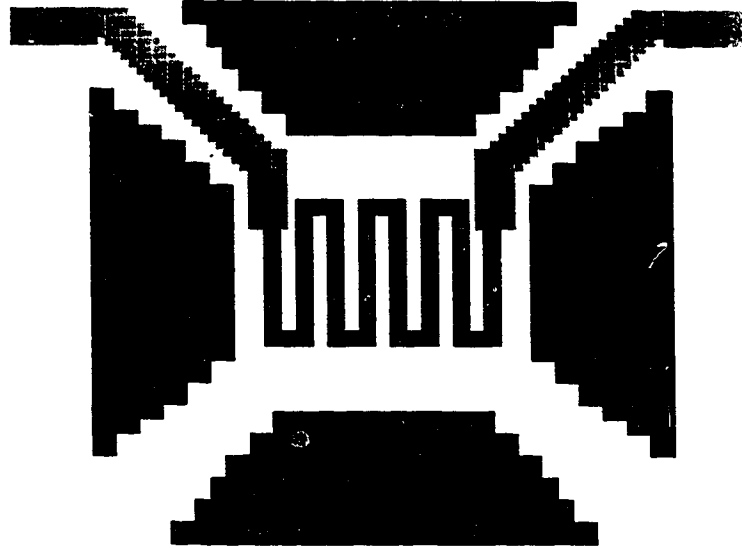


Figure 3.3: Plan view of suspended platform.

The photon detector has been an excellent performance sensor in almost all the spectrum region of radiation except the far IR. But almost all the IR photon detectors are characterized by high cost, high maintenance requirement, and high power consumption [41]. Fabricating low-cost IR detectors has been the main motivation behind the investigation on micro-thermal radiation sensors, which has advantages over its macro-predecessor, advantages such as higher sensitivity and faster response.

The temperature variation of the sensing element inside a thermal radiation sensor can be measured by any of a number of temperature-dependent mechanisms, such as thermoelectric voltage [42], resistance change [41], or p-n junction voltage of a diode [43]. The device discussed in this section is a miniature bolometer fabricated using a standard CMOS process.

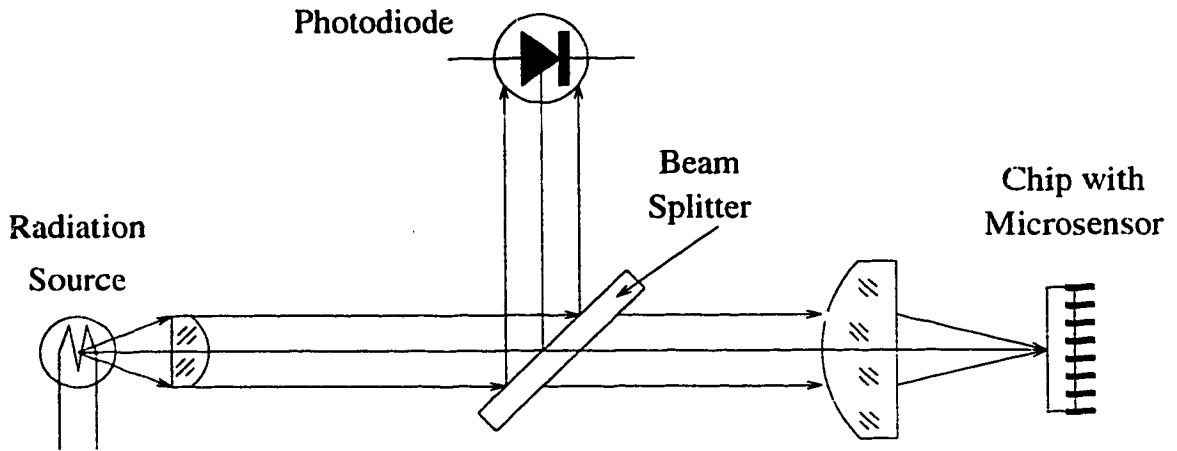


Figure 3.4: Experimental setup for radiation sensor.

The plan view of the device is shown in Figure 3.3. It is a suspended square oxide platform with four support arms on the corners. The cavity beneath the platform is anisotropically etched through the four black regions where the silicon substrate is exposed. The temperature sensing element is the serpentine-shaped polysilicon resistor, sandwiched between the oxide layers.

Figure 3.4 shows the experimental setup. A tungsten filament lamp was used as the radiation source. To obtain different radiation intensities, the lamp was powered by a Variac autotransformer. An EG&G photodiode was used to monitor the radiation intensity. The 50% beam splitter permits simultaneous radiation measurements by both the photodiode and the micro-radiation sensor. An optical lens was placed in front of the microsensor so that the radiation would only reach the sensor structure under test. Both the bolometer resistance and photodiode output were recorded with a digital multi-meter (DMM). The average temperature elevation of the microplatform was calculated using Equation (3.2).

Figure 3.5 plots the temperature variation of the platform against the output signals from the photodiode. The variation of the microplatform temperature

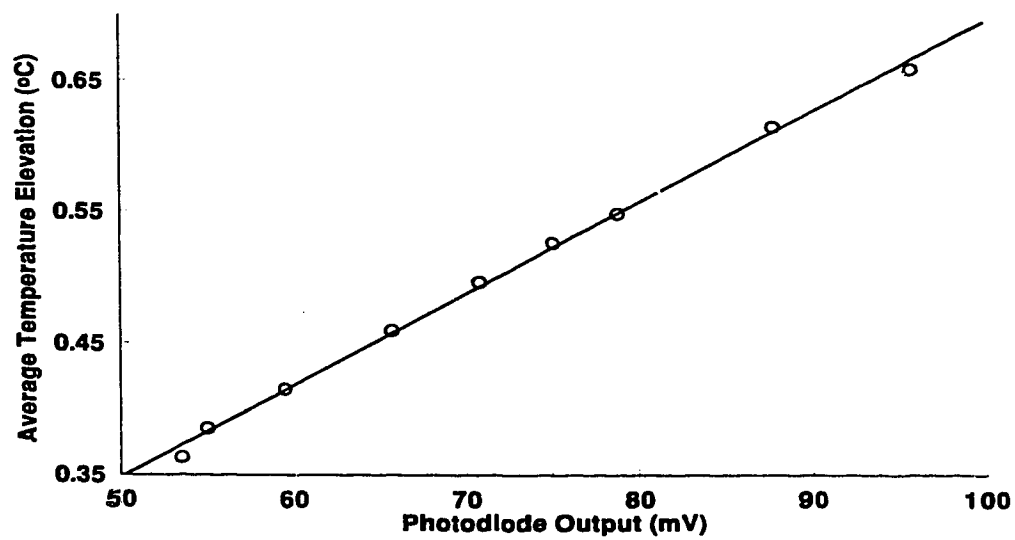


Figure 3.5: Microplatform as a radiation sensor.

and hence the sensor resistance increases linearly with incident radiation intensity. This observation implies that the microsensor response to incident radiation can be well described by a first order system using the first law of thermodynamics. The equation that governs the process can be formulated as:

$$P_i = K(\bar{T} - T_0) \quad (3.3)$$

where P_i is the absorbed incident radiation power, \bar{T} is the average temperature of the microstructure, T_0 is the temperature of the environment, and K is the total thermal conductance between the microplatform and the environment. Among these parameters, only K depends on the geometric shape of the microstructure. After examining the radiation sensor and pressure sensor structures carefully, it is easy to understand that anisotropic etching has formed cavities isolating thermal conduction between the microstructure, either microbridge or microplatform or cantilever, and the silicon substrate, making those structures thermally sensitive to the measurands. The concept can also be explained by looking at Equation (3.3): the thermal conductivity K has been reduced so significantly by the cavity under the platform that the temperature elevation of the platform ($\bar{T} - T_0$) becomes measurable as it is subjected to a radiation energy. Thus $1/K$ is used to indicate the thermal sensitivity of any thermally sensitive structure.

A similar platform structure was also used as a thermal radiation emitter which converted the electrical energy into radiation [44, 45]. In a thermal radiation emitter, electrical energy was converted to heat by the microresistor heater sandwiched inside the platform. Radiation was emitted due to the significant temperature increase on the platform. The process can also be described by Equation (3.3), at least for low \bar{T} , where P_i denotes the input electrical power rather than the incident radiation. Obviously, the smaller the value of K , the more efficient the

system would be.

3.3 Thermal Sensitivity

For thermally sensitive microstructures fabricated using standard IC processes, thermal sensitivity is an important parameter because it determines the general sensitivity of any thermal sensor and determines the general conversion efficiency of the thermal device, such as a thermal radiation emitter.

There is a simple and effective way to measure the thermal sensitivity of a microstructure. By definition, thermal sensitivity is the average temperature rise of the microstructure under unit power dissipation. According to Equation (3.3), thermal sensitivity can be formulated as:

$$1/K = (T - T_0)/P_i \quad (3.4)$$

$(T - T_0)$ can be easily estimated by measuring the resistance of the temperature sensitive polysilicon resistor inside the structure. If the structure is powered by electrical energy, such as a constant current, the dissipated power P_i can be calculated using current through and voltage across the resistor.

To demonstrate the procedure to extract the thermal sensitivity, a set of constant currents ranging from 1.8 mA to 3.2 mA were fed through the polysilicon resistor of the bridge-like structure discussed in Section 3.2.1 and illustrated in Figure 3.1, and the respective voltages measured using the DMM. Those I-V values were converted into the dissipated power and respective structure temperature increase as plotted in Figure 3.6. To investigate the effect of the ambient medium (air), a similar set of measurements was performed in vacuum (pressure less than 10^{-4} Torr), using currents of 0.60-0.95 mA, and the calculated results are also included

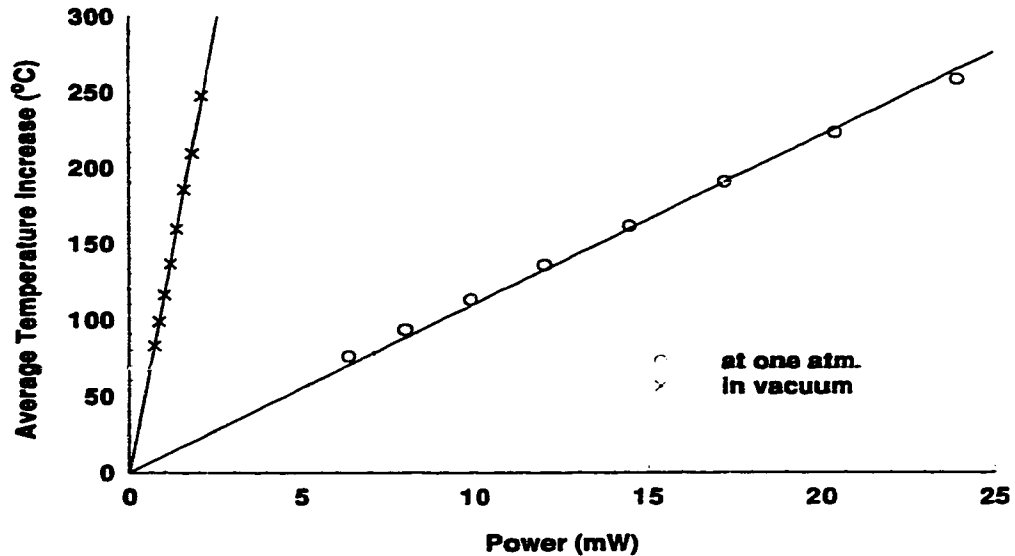


Figure 3.6: Thermal sensitivity measurements under two ambient pressures.

in the figure.

Under both pressures, the temperature rise is a linear function of the dissipated power. Because the origin must also be one point of the $(T - T_0)$ versus P_i plot, straight line fitting, restrained to pass through the origin, is performed on the data points by the method of least-squares. The slope of the fitted line is the thermal sensitivity of the structure. The points from the vacuum measurement lie closely on the straight line, implying that thermal sensitivity is almost a constant over the tested temperature range. For the measurement at one atmosphere, the experimental points do not fit the straight line as well, presumably because the thermal conductivity of the air depends slightly on the temperature [46]. The temperature rise at high dissipated power (~ 25 mW) is below the fitting line due to the higher thermal conductivity of the air at that temperature. Nevertheless, thermal

sensitivity is an excellent thermal characteristic indicator for these thermally sensitive structures. For this particular structure, the measured thermal sensitivity is 1.1×10^4 °C/W at one atmosphere and 11.6×10^4 °C/W in vacuum. The significant thermal sensitivity difference for the two environment pressures indicates that heat loss through the ambient air is very significant. Under one atmosphere pressure, about 90% of the total heat loss was conducted through the gas. This estimation is based on the assumption that the heat losses through the suspension arms are the same for both pressures, i.e. one atmosphere and vacuum, if the average temperature rises of the device are the same. This assumption is valid for this particular device as pointed out by the numerical simulation [17]

Because thermal sensitivity is the thermal resistance between the microstructure and its surroundings, its value depends largely on the geometry of the specific structures. For the platform structure used as a radiation sensor in the previous section, the measured thermal sensitivity is 2.3×10^4 °C/W at one atmosphere and 10.1×10^4 °C/W in vacuum. These results show that better radiation sensor sensitivity could be achieved by operation in a vacuum or in a gas of low thermal conductivity, such as SF_6 .

Thermal isolation is the most important parameter in designing a sensor of ultimate sensitivity or an actuator with high energy conversion efficiency. The next section will discuss on how to increase the thermal isolation with proper layout design.

3.4 Performance Improvement

The performance of a thermally sensitive structure, used either as a sensor or actuator, depends largely on its thermal sensitivity and hence its geometric structure. Because of the limitation provided by standard CMOS compatible materials,

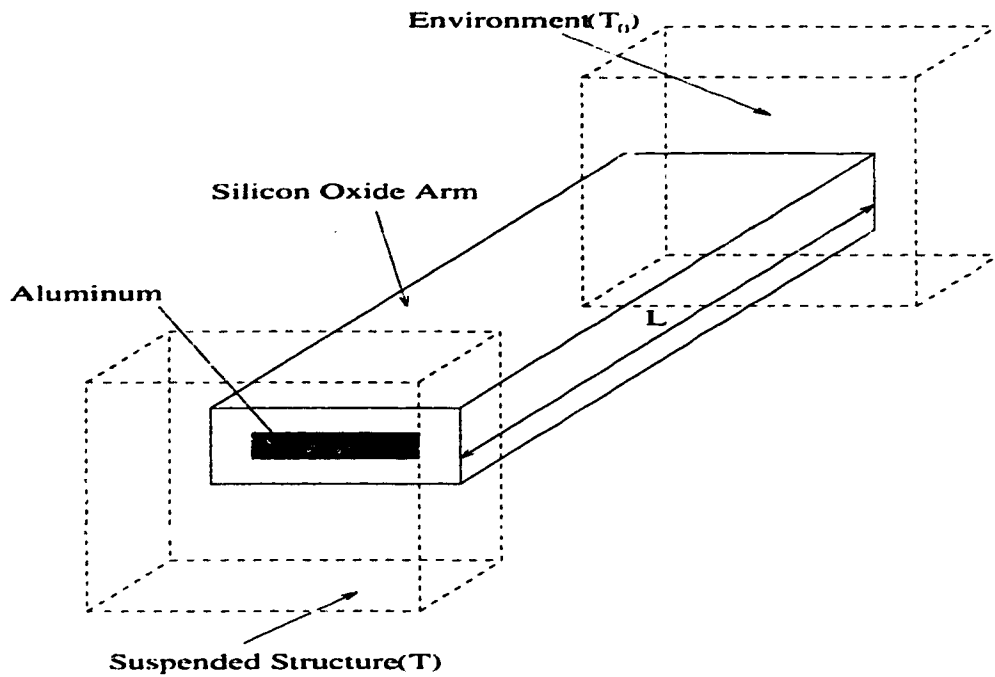


Figure 3.7: Suspension arm serves as a thermal link.

appropriate layout design for the microstructure turns out to be crucial for a satisfactory device performance in practical applications. As discussed before, thermal sensitivity is the thermal resistance between the suspended structure and the environment, which is determined by the thermal conductance (K). The heat loss mechanisms from a microstructure usually include radiation, conduction through the structure support arms to the silicon substrate and conduction and convection through the surrounding gas. Natural convection has been shown to be negligible [54]. The gas thermal conductance is a function of both temperature and absolute pressure and is difficult to model by a linear system. Heat loss by radiation is often negligible if the structure temperature is below 300 °C. Thus the discussions of this section will concentrate on the thermal resistance of the support arms.

Assume that the support arm shown in Figure 3.7 is the only thermal link between the suspended structure and the environment. To make the model more realistic,

the support arm is composed of silicon dioxide with aluminum wire sandwiched inside. The equation for the heat flow through the arm in the steady state can be formulated as

$$H = (k_{Al}A_{Al} + k_{ox}A_{ox})(T - T_0)/L \quad (3.5)$$

where H is the quantity of heat flowing through the arm per unit time, k_{Al} and k_{ox} denote the *thermal conductivity* of aluminum and silicon dioxide respectively. A_{Al} and A_{ox} are their cross-sectional areas, $(T - T_0)$ represents the temperature difference between the structure and the environment, and L is the total length of the arm.

At steady state, H should be equal to the input power dissipated in the structure. Using Equation (3.4), the structure thermal sensitivity is

$$1/K = L/(k_{Al}A_{Al} + k_{ox}A_{ox}) \quad (3.6)$$

One obvious way to improve the thermal sensitivity is to increase the support arm length L . However, space requirements for some sensor applications often limit attainable arm length. Meander or spiral shaped structures have been introduced to overcome this problem [48]. Reducing the the cross-sectional areas is another way to enhance the thermal sensitivity. Since the vertical dimension (thickness) of a support arm is a fixed quantity for a specific process, the width of support arm should be minimized as much as the design rules allow.

The aluminum wire in Figure 3.7 plays an important role in the heat conduction due to its high thermal conductivity ($k_{Al} = 237W/m^{\circ}C$). The heat leakage can be significantly reduced by replacing the aluminum with polysilicon, a material with much lower thermal conductivity ($k_{poly} = 34W/m^{\circ}C$). However, the thermal

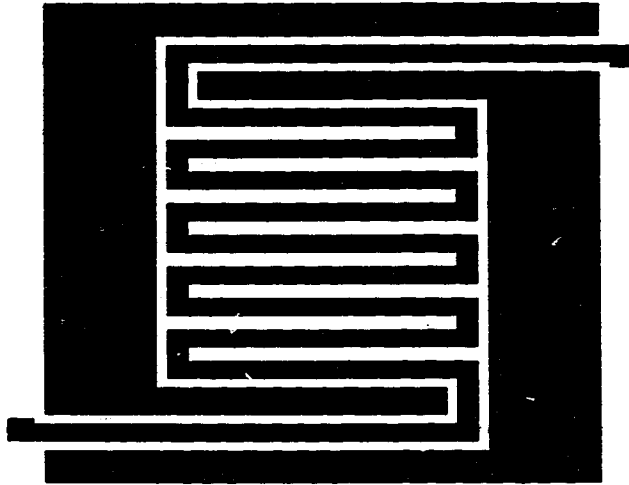


Figure 3.8: Plan view of a platform with enhanced thermal sensitivity.

sensitivity is by no means the only factor to be considered in the actual layout design. A successful design should result in a robust and stable structure with high thermal sensitivity.

Figure 3.8 shows the layout design for a microplatform with enhanced thermal sensitivity. The suspended structure is supported by two thinner and longer arms compared with the four-armed structure in Section 3.2.2. The aluminum inside the arm is replaced by the polysilicon. Thermal sensitivity measurements indicate that the improvement is substantial: $8.6 \times 10^4 \text{ }^\circ\text{C/W}$ over $2.3 \times 10^4 \text{ }^\circ\text{C/W}$ at one atmosphere and $93.4 \times 10^4 \text{ }^\circ\text{C/W}$ over $10.1 \times 10^4 \text{ }^\circ\text{C/W}$ in vacuum.

This chapter has shown that the thermal sensitivity of a device can be easily calculated by measuring its I-V characteristics. It was found that, for some devices, up to 90% of heat loss was by conduction through the gas. Thermal sensitivity

can be enhanced significantly by modifying the physical structure or eliminating the ambient gas or by doing both.

Chapter 4

Dynamic Characteristics Investigation

It is very common that a sensor or actuator operates under time-varying conditions. The optimum performance of these devices depends on the understanding of their dynamic characteristics. In addition, time-varying testing can reveal the thermal properties, such as thermal capacitance, which can't be obtained using the steady state measurement. The resistance of a micromachined polysilicon resistor has been measured under excitation by both a constant current and constant power step. The time-varying response of the polysilicon resistor at two different pressures was observed under various step amplitudes. Analysis will be performed to link the response to the physical processes generating the phenomenon.

4.1 Experimental Setup and Procedure

Fabricated using Northern Telecom 1.2 μm CMOS process, the device under test is identical to the pressure sensor discussed in the previous chapter, as illustrated

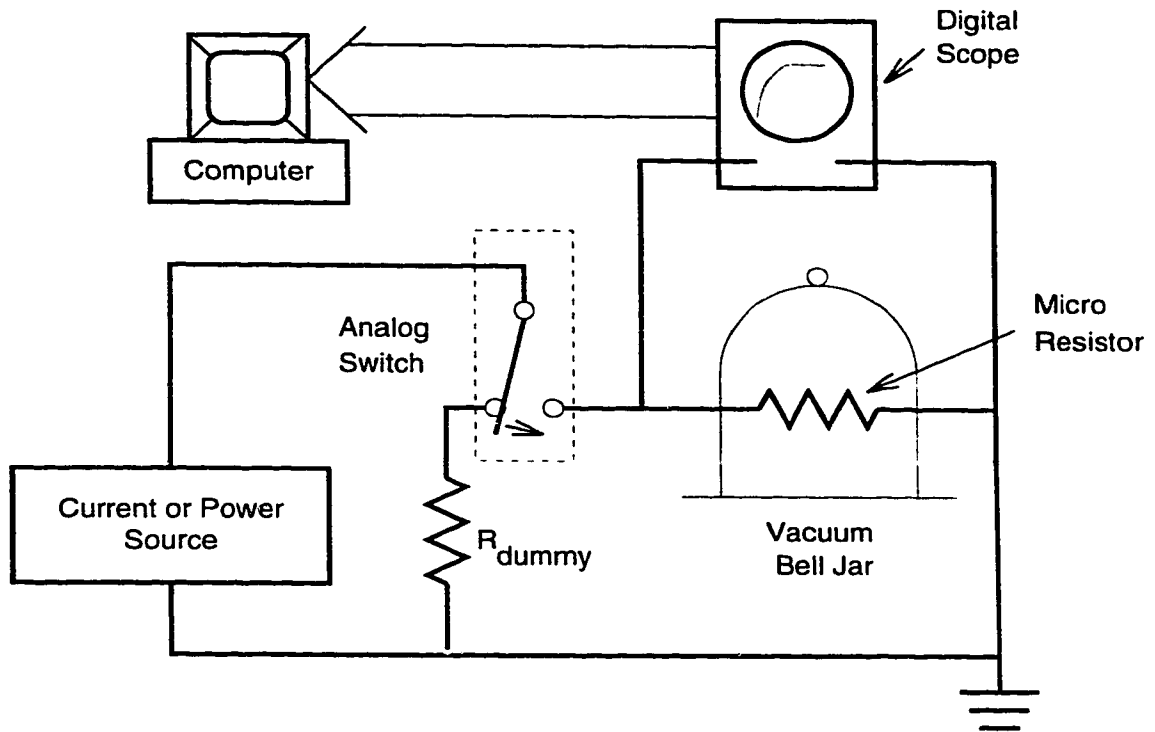


Figure 4.1: Experimental setup for measuring dynamic response.

in Figure 3.1, containing a polysilicon resistor, made of the poly1 layer of the process, sandwiched inside a bridge-like silicon dioxide suspended structure. The experimental setup for measuring the time-varying response is sketched in Figure 4.1.

The device was placed in a bell jar/diffusion pump system and at pressures of either 1 atmosphere, or 10^{-4} Torr. This latter pressure will be referred to as "vacuum". The microresistor was subjected to a step-function input of constant current (CC) or constant power (CP). The CC measurements were initiated by switching a continuously operating constant current source from a dummy load resistor to the polysilicon microresistor under test, using a solid-state switch. The

resistance of the dummy load was matched in value as closely as possible to the room-temperature polysilicon resistance, and the switching occurred in less than $0.5 \mu s$. This switching procedure minimized transient effects on the operation of the CC source.

The CP source was originally developed for testing polysilicon resistors at a preset constant power, independent of the load resistance [49]. The same load-switching technique was employed as in the CC mode in initiating the power step-function input. Transient effects after switching tended to persist no longer than $0.5 ms$.

Upon application of the current or power step-function input, the microresistor temperature and hence the resistance increased from room temperature to its final steady-state value. This value and the time to attain it depend on the step amplitude, the excitation mode, heat capacitance and the relevant heat-loss mechanisms. It should be pointed out that the measured response is the device thermal response. The electrical time constant is much smaller and any delay caused by electrical response is therefore negligible.

The device response was observed by measuring the voltage generated across the microresistor using a digital sampling/storage oscilloscope at a step-function repetition rate of 1 Hz. Signal averaging was necessary for the low current or CP excitation mode measurements; a maximum of 256 sweeps was available. The data was then downloaded into a 386 PC for analysis. The input step amplitudes, for both pressures under either CC or CP operation mode, were selected so that the average temperature increase of the device is below its critical value ($\sim 300^\circ C$) [32, 33]; values greater than this limit produced permanent changes both in the room-temperature resistance and the TCR.

A typical CC response is plotted in Figure 4.2 at one atmosphere. The current step $I = 2.6 mA$. The device resistance, proportional to the measured voltage, rises

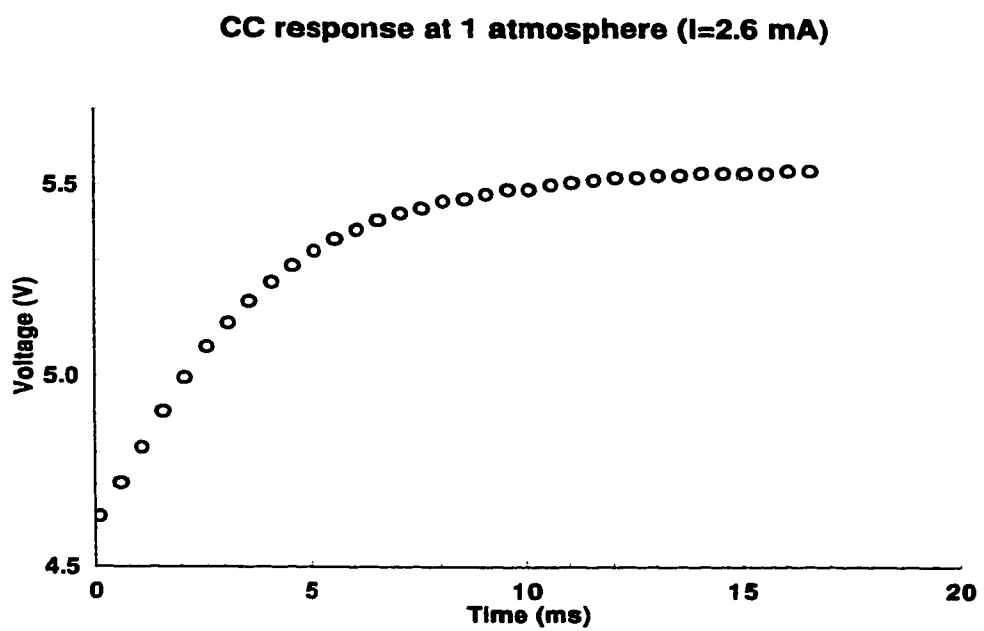


Figure 4.2: Voltage measured across the microresistor under CC operation. Resistance is proportional to V . Current step occurs at $t=0$.

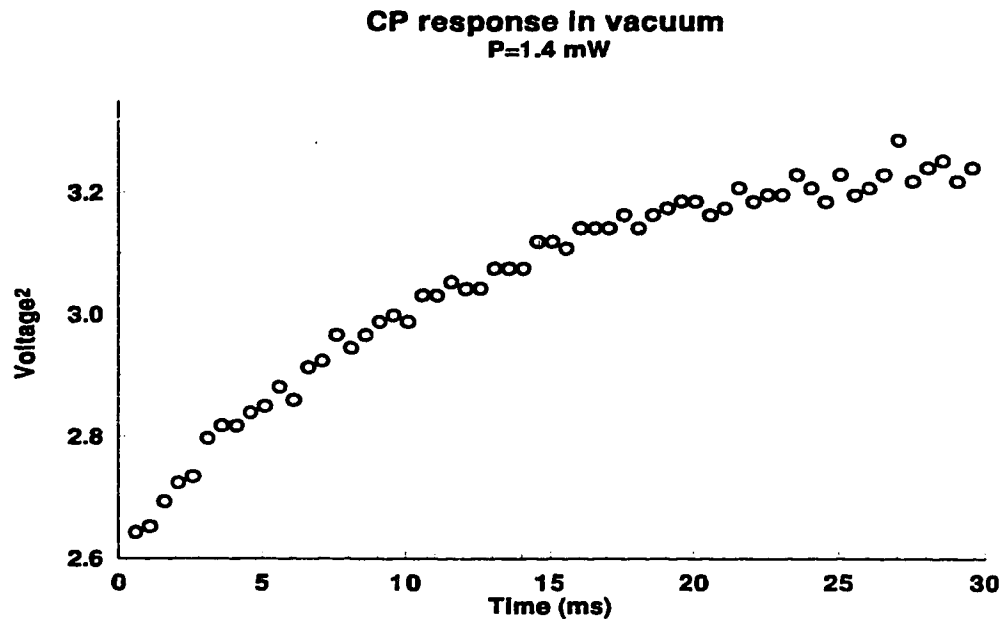


Figure 4.3: Square of voltage measured under CP operation. Resistance is proportional to V^2 . Power step occurs at $t=0$.

from its value at room temperature, $R_0 = 1.806k\Omega$, to its steady-state value, $R_{ss} = 2.141k\Omega$ in a time of approximately 15 ms. This resistance increase corresponds to an increase in the average temperature, $\Delta\bar{T}$, of approximately $180^\circ C$. The value of $\Delta\bar{T}$ quoted here is obtained from the known values for R_0 , R_{ss} and the TCR of the polysilicon resistor. Even with signal averaging, the steady-state signal-to-noise ratio, represented by the change in voltages of Figure 4.2 to the scatter of points varied from approximately 10:1 to 100:1, depending on input current step I and pressure conditions.

Figure 4.3 shows the response of the same resistor under CP operation in vacuum. The power step amplitude $P = 1.4mW$. The device resistance, now proportional

to V^2 , rises from R_0 to a steady-state value of $R_{ss} = 2.330k\Omega$, corresponding to a temperature elevation of $\Delta\bar{T} = 290^\circ\text{C}$, in a time of approximately 30 ms. The signal-to-noise ratios for this mode of excitation were worse than the CC mode, being as poor as 3:1 at low power levels. The value of $\Delta\bar{T}$ in this example is close to the maximum value of 300°C .

4.2 Analytic Modeling for CC Operation

Analytic modeling of a device structure is important to understand qualitatively the device operation and properly interpret its response under given conditions. It is also essential for design optimization of further devices.

Because the structure under study has complex geometry (20 oxide arms support the suspended microbridge), some degree of simplification is necessary to make the analytic modeling possible. The various assumptions made in the solution are discussed in what follows.

- Temperature gradients on the bridge beam cross section area are ignored as the total length of the bridge ($L = 1000\mu\text{m}$) is much longer than the width ($w = 20\mu\text{m}$) and thickness ($t = 2\mu\text{m}$).
- Natural convection is not considered because it has been observed that the device response is independent of device orientation.
- The 20 oxide support arms will be lumped into two pieces of equivalent thermal conductors continuously distributed along both sides of the beam.

Following the above assumptions, a differential section of the beam of width w , thickness t_{ox} , length Δx , and cavity depth s , is shown in Figure 4.4. The heat balance for the section is given by

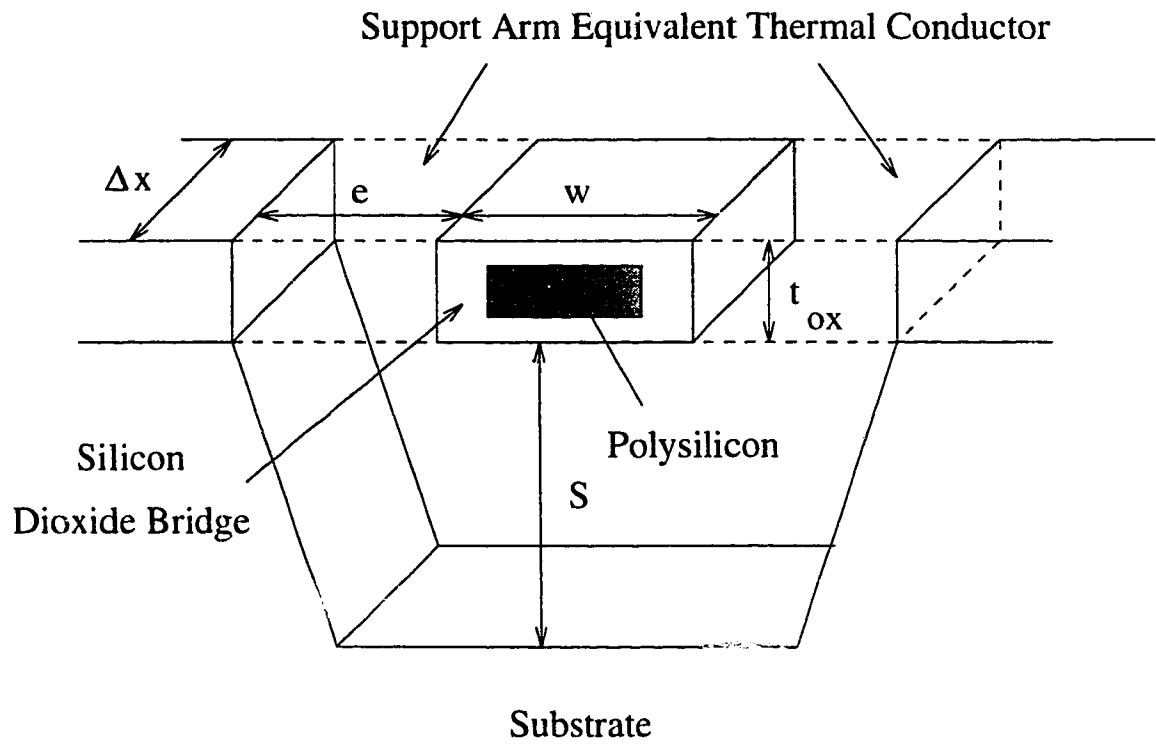


Figure 4.4: Differential section of the bridge structure.

$$Q_{total} = P - Q_{cond} - Q_{rad} \quad (4.1)$$

where Q_{total} is the net rate of change of the internal energy of the element, P is the power generated inside, Q_{cond} is heat loss mechanism acting on the element due to conduction, and Q_{rad} is the heat loss due to radiation.

In Equation (4.1), Q_{total} is

$$Q_{total} = (c_{poly}\rho_{poly}A_{poly} + c_{ox}\rho_{ox}A_{ox})\Delta x \frac{\partial T}{\partial t} \quad (4.2)$$

where c_{poly} and c_{ox} denote specific heat of polysilicon and silicon dioxide respectively, ρ_{poly} and ρ_{ox} represent their densities, A_{poly} and A_{ox} are their cross-sectional areas, T is element temperature, and t represents time.

The power generated by the input current I can be formulated as

$$P = I^2 R_0 \Delta x [1 + \alpha(T - T_0)] / L \quad (4.3)$$

where R_0 is the room temperature resistance of polysilicon, α is the TCR of polysilicon, T_0 denotes the room temperature, and L is the total length of the bridge beam (polysilicon resistor).

The conduction term in Equation (4.1) consists of three components, namely conduction through the beam itself, conduction through the gas, and conduction through the support arms.

The equation for the heat conduction through the beam is

$$Q_{cond1} = (k_{poly}A_{poly} + k_{ox}A_{ox}) \left(\frac{\partial T}{\partial x} \Big|_{x + \Delta x} - \frac{\partial T}{\partial x} \Big|_x \right) \quad (4.4)$$

where k_{poly} and k_{ox} are the thermal conductivities of polysilicon and oxide respectively.

The second component of the conduction is the heat loss through the surrounding gas. The actual physical process is very complex. The first order approximation that only considers the heat flow to the base of the cavity is formulated in what follows.

$$Q_{cond2} = \eta_g k_g(p) w \Delta x (T - T_0) / s \quad (4.5)$$

where $k_g(p)$ is the thermal conductivity of the gas, the factor η_g denotes the coefficient accounting for the first order approximation, and s is the cavity depth (see Figure 4.4). The gas conductivity is both a function of temperature [50] and absolute pressure p [51]. For simplicity, its temperature dependence is neglected.

The heat loss through the support arms is assumed to be averaged out along the whole beam

$$Q_{cond3} = \eta_{ox} k_{ox} t_{ox} \Delta x (T - T_0) / \epsilon \quad (4.6)$$

where the factor η_{ox} denotes the coefficient accounting for the process of the support arm averaging effect, t_{ox} is the beam thickness, and ϵ is the distance between beam and cavity edge (see Figure 4.4).

The last term in Equation (4.1) represents the radiative heat loss which can be expressed by

$$Q_{rad} = \epsilon \sigma (2w + 2t_{ox}) \Delta x (T^4 - T_0^4)$$

where σ is the Stefan-Boltzmann constant and ϵ is the emissivity of silicon dioxide surface. The value of ϵ is assumed to be a constant although it is in fact

spectrum-dependent [52]. If the bridge temperature is not much higher than the room temperature ($T - T_0 \leq 300^\circ\text{C}$). The above equation can be adequately approximated by the first term of a Taylor series centered at T_0

$$Q_{rad} = 4\epsilon\sigma(2w + 2l_{ox})\Delta x T_0^3(T - T_0) \quad (4.7)$$

Combining Equation (4.1) – (4.7) and taking the limit as $\Delta x \rightarrow 0$ results in the linear second-order partial differential equation

$$a \frac{\partial T}{\partial t} = b - (-c_1 + c_2 + c_3 + c_4)(T - T_0) + d \frac{\partial^2 T}{\partial x^2} = b - c(T - T_0) + d \frac{\partial^2 T}{\partial x^2} \quad (4.8)$$

in which

$$a = c_{poly}\rho_{poly}A_{poly} + c_{ox}\rho_{ox}A_{ox}$$

$$b = I^2 R_0 / L$$

$$c_1 = \alpha I^2 R_0 / L$$

$$c_2 = \eta_y k_y(p)w/s$$

$$c_3 = \eta_{ox} k_{ox} l_{ox} / c$$

$$c_4 = 4\epsilon\sigma(2w + 2l_{ox})T_0^3$$

$$c = -c_1 + c_2 + c_3 + c_4$$

$$d = k_{poly}A_{poly} + k_{ox}A_{ox}$$

Further rearranging Equation (4.8) yields

$$\frac{\partial u}{\partial t} = \beta \frac{\partial^2 u}{\partial x^2} - \xi u \quad (4.9)$$

with

$$u = T - (T_0 + b/c); \quad \beta = \epsilon^2/a; \quad \xi = c/a.$$

In order to find the temperature profile of the microbridge, Equation (4.9) must be solved subject to certain initial and boundary conditions. At the moment of the current step, the whole structure is assumed to have the same temperature as the environment, i.e.

$$u(x, t = 0) = -b/c \quad (T = T_0) \quad (4.10)$$

It is also assumed that the temperature at the microbridge anchors ($x = 0, L$) is always kept identical to that of the substrate, due the much higher thermal conductivity of the aluminum lead. Therefore the boundary condition is

$$u(x = 0, L) = -b/c \quad (4.11)$$

Equation (4.9) can be solved by the method of separation of variables [53] and the solution is

$$u(x, t) = u_{ss}(x) + u_{tr}(x, t) \quad (4.12)$$

where the steady-state solution is

$$u_{ss}(x) = \left(-\frac{b}{c}\right) \frac{\cosh \sqrt{\frac{\xi}{\beta}}(x - L/2)}{\cosh \sqrt{\frac{\xi}{\beta}}L/2} \quad (4.13)$$

and the transient solution is

$$u_{tr}(x, t) = \sum_{n=1}^{\infty} B_n \sin\left(\frac{n\pi x}{L}\right) \exp\left[-\beta\left(\frac{n^2\pi^2}{L^2} + \frac{\xi}{\beta}\right)t\right] \quad (4.14)$$

with

$$B_n = \frac{2}{L} \left(-\frac{b}{c} \right) \int_0^L \left[1 - \frac{\cosh \sqrt{\frac{\xi}{\beta}}(x - L/2)}{\cosh \sqrt{\frac{\xi}{\beta}}L/2} \right] \sin\left(\frac{n\pi x}{L}\right) dx \quad (4.15)$$

The average temperature of the bridge is

$$\bar{u} = \frac{1}{L} \int_0^L u dx = \bar{u}_{ss} + \bar{u}_{tr} \quad (4.16)$$

where

$$\bar{u}_{tr} = \frac{1}{L} \int_0^L u_{tr} dx = \sum_{n=1}^{\infty} \frac{(1 - (-1)^n) B_n}{n\pi} \exp \left[-\beta \left(\frac{n^2 \pi^2}{L^2} + \frac{\xi}{\beta} \right) t \right] \quad (4.17)$$

Neglecting the high-order terms in Equation (4.17), the transient (dynamic) response of the polysilicon resistor subjected to a CC step excitation is an exponential time variation

$$\bar{u}_{tr} \approx \frac{2B_1}{\pi} \exp \left[-\beta \left(\frac{\pi^2}{L^2} + \frac{\xi}{\beta} \right) t \right] \quad (4.18)$$

with a time constant

$$\tau = \left[\beta \left(\frac{\pi^2}{L^2} + \frac{\xi}{\beta} \right) \right]^{-1} \quad (4.19)$$

Similar results were obtained by Mastrangelo [46] for their microbridge devices, except they did not have the complication of the averaging coefficients.

The definition of β shows that it is a structure-related parameter whose value depends only on material and geometry of the structure. Once the device has been fabricated, the value of β is fixed. The value of ξ , however, depends not only on the structure but on the operating conditions such as the current step amplitude I

and the surrounding gas pressure p . To illustrate how those operating conditions affect the response time, Equation (4.19) is manipulated into

$$\tau^{-1} = K_0 + K_1 k_g(p) - K_2 I^2 \quad (4.20)$$

where

$$\begin{aligned} K_0 = & \frac{k_{poly} A_{poly} + k_{ox} A_{ox}}{c_{poly} \rho_{poly} A_{poly} + c_{ox} \rho_{ox} A_{ox}} \left(\frac{\pi}{L} \right)^2 \\ & + \frac{\eta_{ox} k_{ox} l_{ox}}{c(c_{poly} \rho_{poly} A_{poly} + c_{ox} \rho_{ox} A_{ox})} \\ & + \frac{4c\sigma(2w + 2l_{ox})T_0^3}{c_{poly} \rho_{poly} A_{poly} + c_{ox} \rho_{ox} A_{ox}} \end{aligned}$$

$$K_1 = \frac{\eta_g w}{s(c_{poly} \rho_{poly} A_{poly} + c_{ox} \rho_{ox} A_{ox})}$$

$$K_2 = \frac{\alpha R_0}{L(c_{poly} \rho_{poly} A_{poly} + c_{ox} \rho_{ox} A_{ox})}$$

K_0 , K_1 and K_2 are the structure-related positive constants, which can be calculated from the geometric and material properties of the device. It can be predicted from Equation (4.20) that the time constant for the CC response of the device, at a given gas pressure, should be a strong function of the current step amplitude. τ^{-1} for a number of current step amplitudes should produce a straight-line plot as a function of I^2 . In addition, response time is also determined by the surrounding gas pressure. Higher pressure (larger $k_g(p)$) should make τ smaller and device response faster.

Analytic modeling for CP mode operation is difficult because the input current is also time-varying. A simpler analytic model, dealing with CP excitation by

ignoring all spatial details of the device, has been discussed in detail elsewhere [54, 55, 56]. In brief, the model concluded that for CP step excitation, the device response is a single exponential time variation with the time constant *independent* of the input step amplitude. As to the relationship between response time and ambient gas pressure, the model predicts a similar trend as the CC step excitation.

4.3 Results and Analysis

For the case of the CC step excitation, the time variation of the voltage across the polysilicon resistor is shown in Figure 4.5 on a semilogarithmic plot. The data used in the plot is identical to the data in Figure 4.2. Thus the operating conditions are $I = 2.6mA$ at a pressure of 1 atmosphere. The plot is closely linear in form, indicating an first order exponential variation of resistance, and hence \bar{n}_r , with time t , as predicted by Equation (4.18). From the slope of the straight line the time constant of $\tau = 3.39ms$ was calculated for the heating process excited by the current step of this particular amplitude.

The straight line plot of Figure 4.5 could be considered to be a “typical” plot. Some of the plots for other conditions were straighter and with less data point spread, while others were not. In particular, the first $0.5ms$ of some, but not all, of the semilogarithmic plots, such as that of Figure 4.5, showed a slight curvature below the straight line. This is mainly caused by the transient effects in the excitation circuit and current source. At the other end of the time scale, noise and the resolution limits of the data acquisition unit result in a large step-shaped spread in the plotted points.

Considering the curvature and data point spread of all the semilogarithmic plots as well as the accuracy of testing equipment, an uncertainty of $\pm 7\%$ is estimated

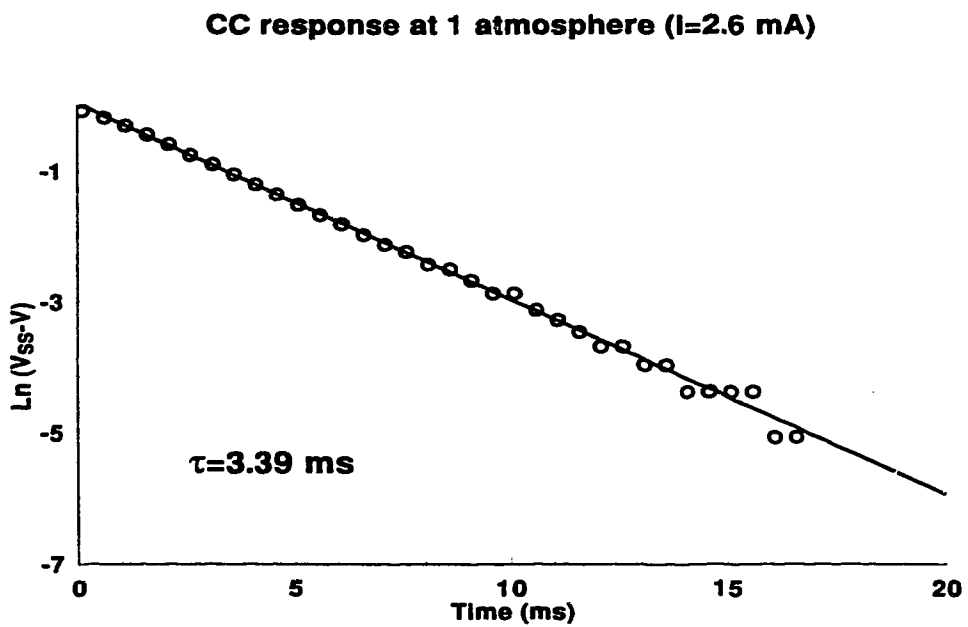


Figure 4.5: Semilogarithmic response of the resistor under CC operation, obtained from data of Figure 4.2.

Table 4.1: Measured time constants for response of CC excitation ($R_0 = 1.806k\Omega$)

At one atm			In vacuum		
Current (mA)	τ (ms)	ΔR (%)	Current (mA)	τ (ms)	ΔR (%)
1.60	2.49	4.92	0.60	12.35	9.53
1.80	2.58	8.75	0.65	12.56	11.33
2.00	2.79	10.74	0.70	13.00	13.36
2.20	2.96	13.01	0.75	13.70	15.70
2.40	3.15	15.60	0.80	14.60	18.33
2.60	3.39	18.59	0.85	15.83	21.31
2.80	3.59	21.91	0.90	16.18	24.09
3.00	3.88	25.63	0.95	16.91	28.45
3.20	4.19	29.70			

on the measurement of the time constants. The measured time constants of the CC excitation for this particular resistor are listed in Table 4.1.

The values of Table 4.1 are consistent with the predictions of Equation (4.20): the device responded to a CC excitation much faster at one atmosphere than in vacuum; and its time constant is a strong function of the current step amplitude. The variation of τ with current amplitude is shown in Figure 4.6 as a plot of τ^{-1} versus I^2 . The figure indicates that the points fall approximately on a straight line, for both pressures, as expected from Equation (4.20). According to Equation (4.20), $\tau^{-1} - I^2$ plots under two pressures should be parallel to each other since K_2 is a constant independent of pressure. The two least-square fitting straight lines for the two pressures shown in the diagram, however, are not parallel. It is probably because the actual thermal conductivity of the ambient gas $k_g(p)$ depends on the temperature and thus the input power and therefore on the current amplitude I . The experimental points in the τ^{-1} vs I^2 plot support the explanation. Those

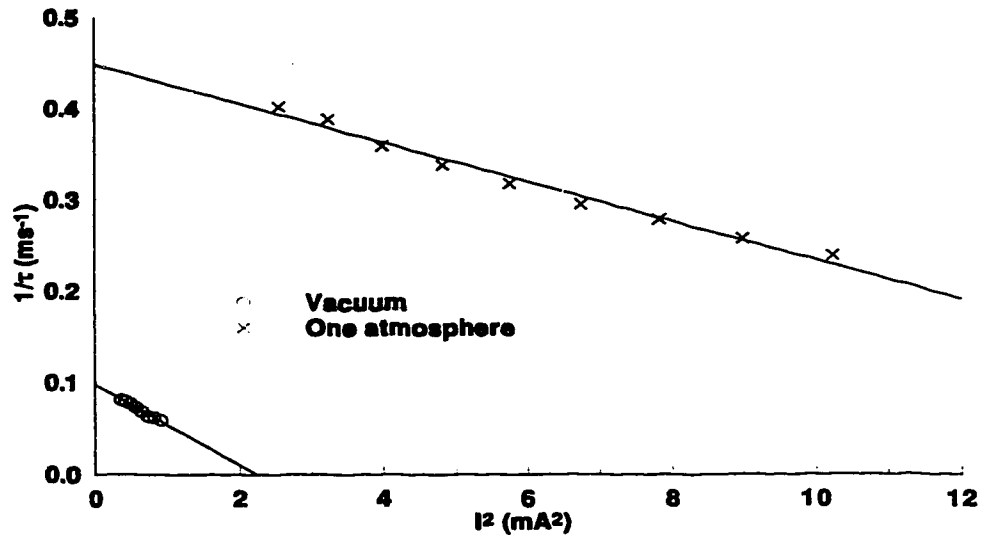


Figure 4.6: Variation of τ^{-1} with square of current step amplitude.

τ^{-1} s at the currents higher than about 5 mA is larger than the predictions of the first order model due to the increasing values of $k_g(p)$ in Equation (4.20), making the best fitting line for the data measured at one atmosphere unparallel with the vacuum line. The uncertainty for the time constant measurements discussed above may also contribute to the phenomenon.

With operation in the CP mode, the response was also exponential in time, as indicated in Figure 4.7, which is the semilogarithmic plot of the data from Figure 4.3. Least-square fitting of the experimental points obtains the response time (τ) for the specific CP excitation ($P = 1.4mW$) of about 11.89ms. Generally the accuracy of measuring the time constants for the CP response is less than for the CC response due to the lower signal-to-noise ratio. An uncertainty as high

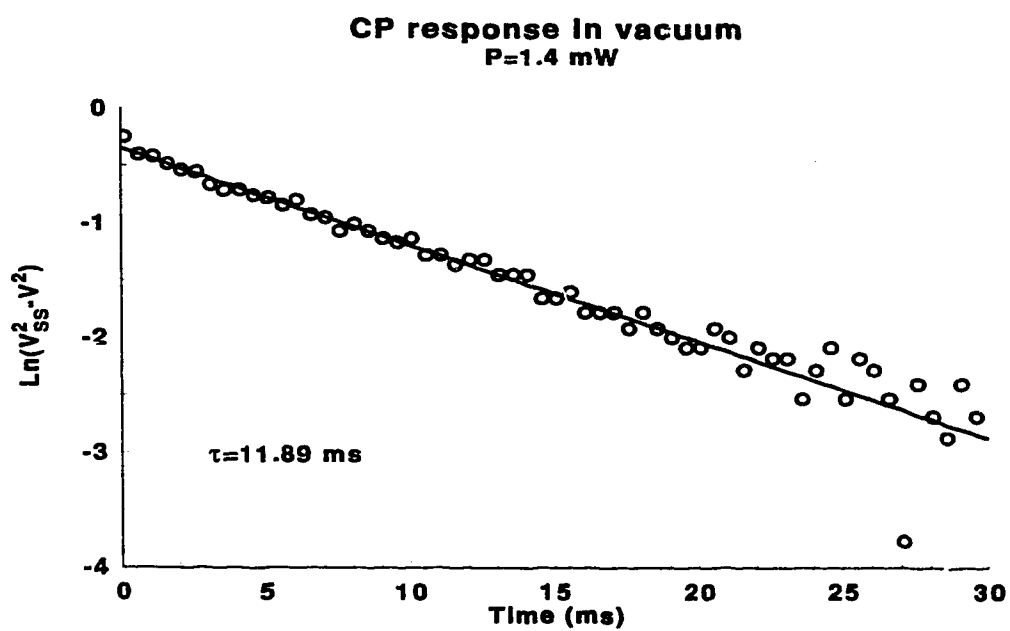


Figure 4.7: Semilogarithmic response of the resistor under CP operation, obtained from data of Figure 4.3.

Table 4.2: Measured time constants for response of CP excitation ($R_0 = 1.806k\Omega$)

At one atm			In vacuum		
Power (mW)	τ (ms)	ΔR (%)	Power (mW)	τ (ms)	ΔR (%)
5	0.99	8.14	0.6	11.36	13.00
10	1.08	14.18	0.8	11.78	17.92
15	0.99	20.42	1.0	11.02	20.36
20	1.04	26.61	1.1	11.47	23.18
25	1.05	31.48	1.2	11.90	26.29
			1.3	11.51	27.65
			1.4	11.89	29.06

as $\pm 12\%$ has been estimated for the measurements. Table 4.2 lists the measured time constants as well as the input power amplitude. Unlike the 'C' response, the risetime of the device under CP excitation is independent of amplitude of the power step. The average time constant $\tau = 1.03 \pm 0.03$ ms at one atmosphere and $\tau = 11.56 \pm 0.4$ ms in a vacuum. The uncertainty cited represents the standard deviation of experimental values. The observation is consistent with the predictions of the model discussed in references [54, 55, 56].

Under either type of excitation, the risetime in vacuum is significantly longer than at one atmosphere. The faster thermal response at one atmosphere is expected due to the additional heat loss available by conduction through the gas. With the discussions in Chapter 3, it can be concluded that thermal sensitivity and thermal response time are interconnected for a device. Improving one of these properties usually sacrifices the other. Appropriate compromise has to be considered, using the application requirements as a guideline, for any real transducer design.

Chapter 5

Movable Structures in CMOS Technology

Until the present time, the majority of CMOS micromachining research has concentrated on the development of static devices, fixed three-dimensional mechanical structures that would function properly without any spatial displacement. All the devices discussed in the previous chapters belong to this category. The growing interest in dynamic (movable) devices questioned the capability of the standard IC process micromachining technology in this area. However, efforts of fabricating dynamic structures using standard processes have been discouraged by the difficulty of finding a suitable force to activate the mechanical movement. The great potential of building dynamic structures using standard IC process has been ignored.

The purpose of this chapter is to demonstrate how a standard CMOS technology can be used to fabricate movable structures by describing the concept development, structure design, fabrication and testing procedure of deflectable mirror devices.

To begin with, an overview on existing movable structures fabricated using CMOS

technology is given, with a detail description of CMOS active mirror being reported. since this chapter is devoted mainly towards the development of deflectable mirror devices.

5.1 Review of CMOS Fabricated Movable Structures

5.1.1 Sub-nanogram Mass Sensor

A $180\mu\text{m} \times 60\mu\text{m}$ silicon dioxide cantilever was built using the standard CMOS $1.2\mu\text{m}$ process offered by Northern Telecom [57, 58]. The device was used to measure the mass of discrete objects sitting on the cantilever arm by monitoring resonant frequency variation of the structure.

The cantilever structures were formed out of CMOS CVD silicon oxide layers embedding polysilicon piezoresistors. The chip containing the cantilever was placed on the top of a miniature vibrating table. Different frequencies were used to vibrate the structure and the resonant frequency was recognized by monitoring resistance variation of the integrated polysilicon piezoresistors with the help of an on-chip amplifier. Calibration of the device was performed using polystyrene calibration spheres as standard weights, because their diameter and density and hence mass are well defined. Placing those micro-objects was achieved using a micro-manipulator. Sensitivity of 0.1 nanogram has been achieved. Mass measurements can also be performed in a liquid medium, offering an economical means to produce bio-mass measurement and monitoring systems.

For this device, the force moving the structure comes from the acceleration imposed by the vibration of the substrate. The mechanism is well suited for this partic-

ular application but can not be extended to applications requiring a stationary substrate.

5.1.2 Electro-thermal Actuator

Several electro-thermal actuators have been designed and fabricated using a standard CMOS process [8, 15, 59]. Their operating principle is based on that of a bimetal strip, made of two layers of different materials with different coefficients of thermal expansion attached together. This strip, when subjected to a temperature increase, curls towards the material with the lower thermal expansion coefficient and produces a mechanical deflection.

In the CMOS electro-thermal actuator discussed in reference [59], aluminum and polysilicon layers have been chosen to be the thermal conducting layers of the “bimetal” strip. To protect them from being attacked by the postprocessing etchant, the polysilicon and metal beams have been wrapped by the CVD silicon oxide layers. Obviously, for a bimetal strip cantilever, the displacement of the unclamped end depends on the magnitude of mechanical deflection and thus on the difference between the two thermal expansion coefficients, strip temperature, and total length of the structure. The longer the cantilever, the more the displacement.

The structure of CMOS actuator is sketched in Figure 5.1 [59]. In order to achieve maximum displacement at the movable end (the central plate with contact-cut squares), the composite beam, polysilicon and aluminum layers sandwiched inside the silicon oxide layers, is coil-shaped to increase the cantilever length without wasting wafer space. The metal and polysilicon are not in contact, except at the central plate, forming a stacked coiled resistive electrical path. Polysilicon also acts as the heating element for the actuator due to its higher resistivity. Post-processing is performed to etch out the silicon under the structure. The mismatched stress

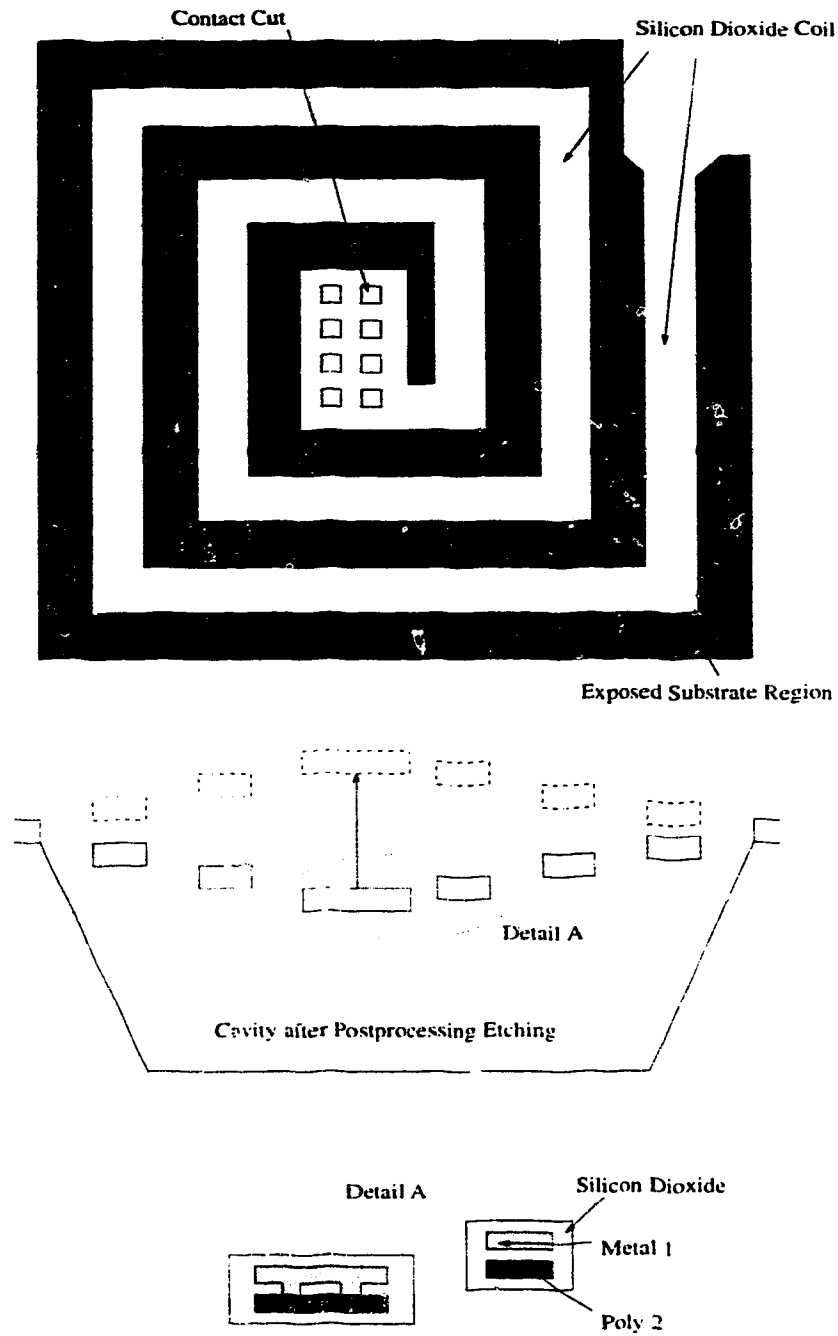


Figure 5.1: Electro-thermal actuator structure.

developed between the polysilicon and metal layers bends the coil into the cavity. When a current is passed through the resistive structure, its temperature rises and the different thermal expansion coefficients of the two materials make the coil move upward, while the central plate has the maximum spatial displacement as shown in Figure 5.1.

5.1.3 Thermally Excited Resonators

Thermally excited Resonators for proximity and pressure sensing have been developed using CMOS IC technology with subsequent micromachining [60, 17]. Microbeam (microcantilever) and microbridge resonators have been made in this way, using the $1.2\mu m$ double metal CMOS process provided by Austria Micro Systems (AMS). As an example, the structure of the microbeam resonator is shown in Figure 5.2, where the two lateral polysilicon resistors are designed for AC heating; the central polysilicon resistor is used for piezoresistive detection. Metal structures serve as optical mirrors and electrical connections.

The polysilicon heating resistors (R) are driven by an AC voltage $V_{ac} \cos(\omega t)$ superimposed on a DC voltage V_{dc} in order to obtain an output signal at the applied frequency. Therefore the generated thermal power P [61, 62] is given by

$$P = \frac{1}{R}(V_{dc}^2 + V_{ac}^2/2 + 2V_{dc}V_{ac} \cos \omega t + V_{ac}^2 \cos 2\omega t) = P_{stat} + P_{d1} \cos \omega t + P_{d2} \cos 2\omega t \quad (5.1)$$

The thermal power P consists of one static component P_{stat} and two dynamic components P_{d1} and P_{d2} with frequency ω and 2ω . Only vibrations with the same frequency ω as the applied AC voltage V_{ac} are investigated. The dynamic heating produces an oscillating bending moment because of different thermal expansion

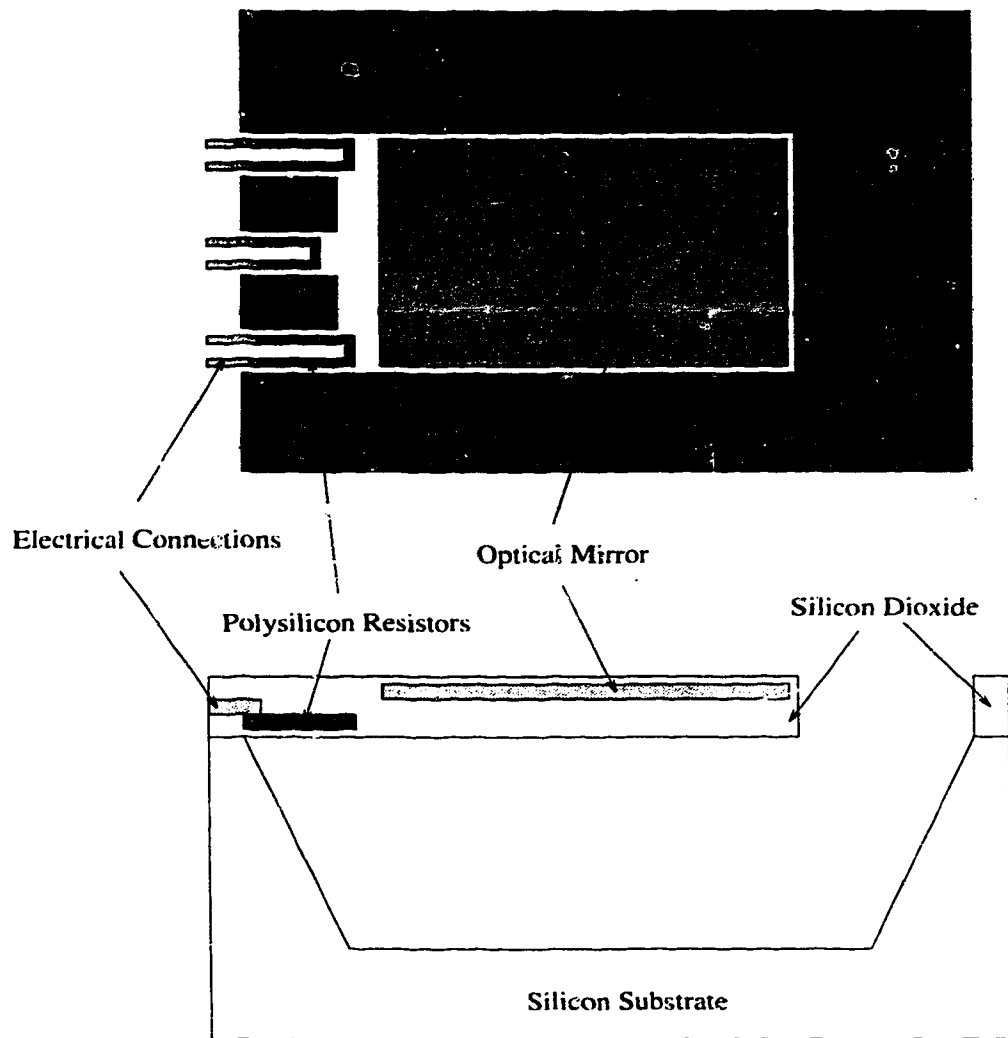


Figure 5.2: Microbeam (cantilever) structure as a thermal excited resonator.

coefficients of the materials involved in the sandwich structure and because of vertical gradients of the dynamic temperature profile (thermal wave) [63, 64].

The resonance frequencies and vibration amplitudes are measured optically by using a laser heterodyne interferometer in combination with a network/spectrum analyzer. The laser beam can be focused on the microstructures with a minimum spot diameter of about $20\ \mu\text{m}$. The laser heterodyne interferometer allows the measurement of vibrating frequency up to 1 MHz with a resolution (depending on frequency) better than 0.01 nm [17].

The experimental results show that thermal excitation of the resonators is feasible for frequencies up to at least 1 MHz [17]. For the cantilever beam resonator, a maximum vibration amplitude of $1.7\ \mu\text{m}$, at the fundamental resonant frequency of $30.43\ \text{kHz}$, was measured, for $P_{\text{stat}} = 11.0\ \text{mW}$ and $P_{\text{d1}} = 9.2\ \text{mW}$. For the bridge-shaped resonator, vibration amplitude of $290\ \text{nm}$ was observed at the fundamental resonance of $79.2\ \text{kHz}$ under excitation power of $P_{\text{stat}} = 7.7\ \text{mW}$ and $P_{\text{d1}} = 10.9\ \text{mW}$.

5.1.4 Thermally Activated Micromirrors

Deflectable micromirrors were originally intended for light modulators, which are used to alter the amplitude or the phase of light. In the late 1960s and early 1970s, high density arrays of micromachined light phase shifters were proposed [65, 66, 67]. In the late 70s, a laser beam deflector [68] and a silicon scanning mirror [69] were built by Petersen. In spite of those efforts, micro-deflectable mirror devices were not commercialized until 1992 when Texas Instruments announced the development of an air-ticket printer, which has a built-in micromechanical light modulator [70]. In 1993, Texas Instruments also successfully developed a high definition display projection system based on a 2-dimensional array of de-

deflectable micro-mirrors. Those products were based on the ongoing research and development of the company for over two decades [71, 72, 73]. The efforts of recent research and development involve the realization of optical choppers [75, 76], micro-interferometers [77, 78, 79], diffraction light modulators [80], scanning mirrors [81, 82, 83], optical shutters [84] and optical switches [85]. At present, the growing interest in the deflectable micro-mirror devices stems from the need to develop fast switching systems for fiberoptic networks built for telecommunication systems. Several micromachined spatial light modulators have been proposed for this purpose [86, 87, 88].

The deflectable mirror devices mentioned above are all fabricated using customized surface micromachining processes. Recently, there have been successful attempts to build deflectable mirrors using standard CMOS bulk micromachining technology [89, 90, 91]. The deflection has been activated by the thermal bimetal effect based on the same operating principle as the actuator discussed in Section 5.1.2. In what follows, the thermally activated mirror developed at the University of Alberta [89] will be used as an example to illustrate operating principle, layout design and performance of the device.

The layout design (plan view) of a typical thermally activated mirror is shown in Figure 5.3. The device consists of two parallel cantilever beams supporting the mirror plate between their tips. Each of the cantilevers is a stacked structure of field oxide layer and CVD layers of oxide and nitride, enclosing a polysilicon heating resistor. The mirror plate is made of all-standard silicon dioxide, aluminum and silicon nitride layers. The metal layer acts as an optical reflector (mirror). The driving support arms are $130\ \mu\text{m}$ long and $12\ \mu\text{m}$ wide. The size of the mirror plate is $160\ \mu\text{m} \times 116\ \mu\text{m}$. The device was fabricated using the Mitel $1.5\ \mu\text{m}$ CMOS process and the gate polysilicon layer (poly1) was used as the heating resistor.

Intrinsic mechanical stress due to the temperature cycles during fabrication results

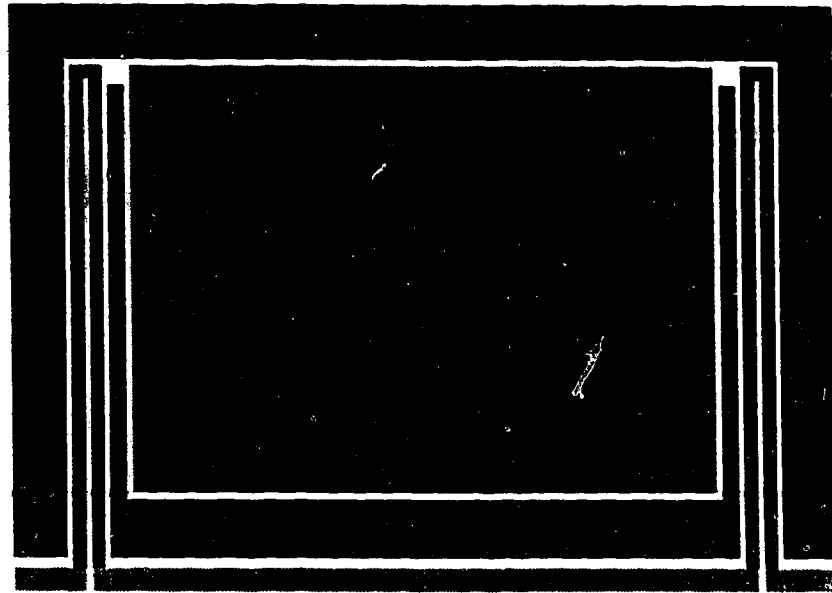


Figure 5.3: Plan view of thermally actuated CMOS micromirror.

in pre-bending of the suspension arms after the structure is released. When heated by an electric current through the polysilicon, the different coefficients of thermal expansion of the beam layers lead to a bending of the cantilevers and thus the tilting of the attached mirror plate. The minimum contact regions between the suspensions and mirror plate not only reduce the bending load on the driving beams, but also keep the mirror reflecting surface flat when the beams are thermally actuated.

The mirror deflection angles are determined by light reflection measurements, as illustrated in Figure 5.4, where a beam from a helium-neon laser was focused on the mirror. The positions on the screen of the light spots of the laser beam reflected by the mirror in the rest and in deflected positions indicate the mirror deflection. The mirror deflection angle is half of the angle α indicated in Figure 5.4. A constant current source was used to drive the mirror and the heater resistance was monitored

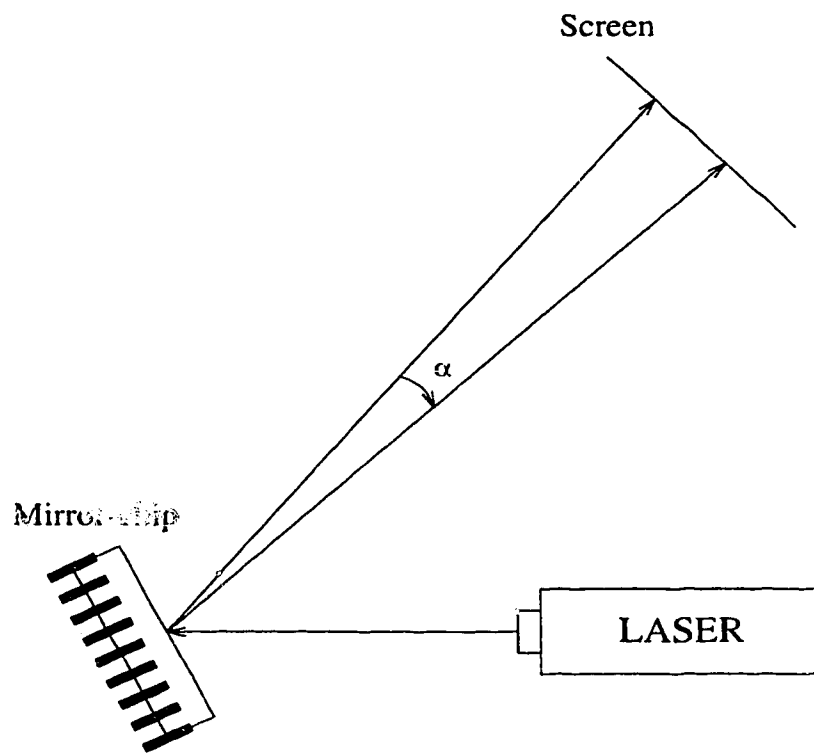


Figure 5.4: Experimental setup for deflection angle measurement.

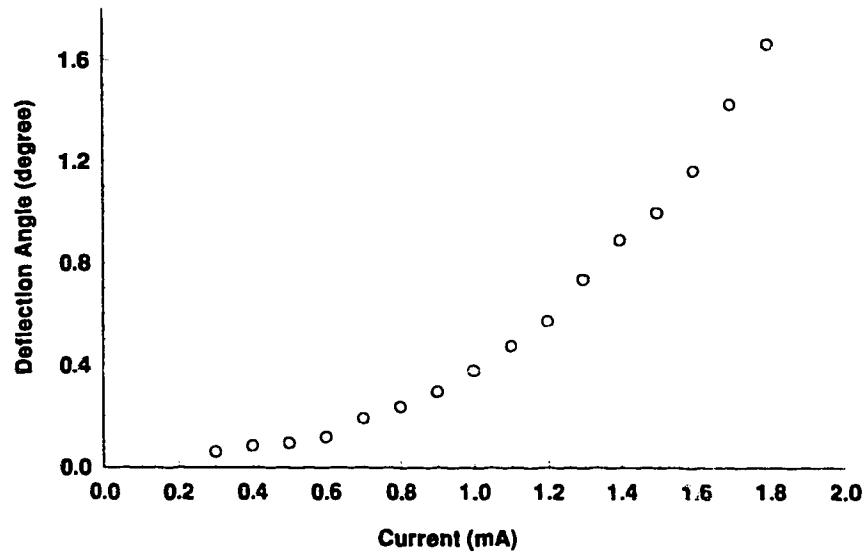


Figure 5.5: Mirror deflection versus the input current.

by a DMM measuring the voltage across the resistor.

Figure 5.5 displays the experimental relationship between the deflection angle and input current while Figure 5.6 shows how the deflection varies with the average temperature of the driving beams. The beam temperature was determined by Equation (3.2) and the TCR value from Table 3.1. From those diagrams, it can be seen that the deflection has a linear relationship with the temperature of the support cantilevers. This observation is justified by the numerical simulation in reference [91]. However, the deflection is more sensitive to the current increase because the heating power $P = I^2R$. The substantial deflection variation with current (higher than 1.2 mA) is caused by both the I^2 term and R 's dependence on the current.

The response time of the mirror deflection was also estimated using the same setup

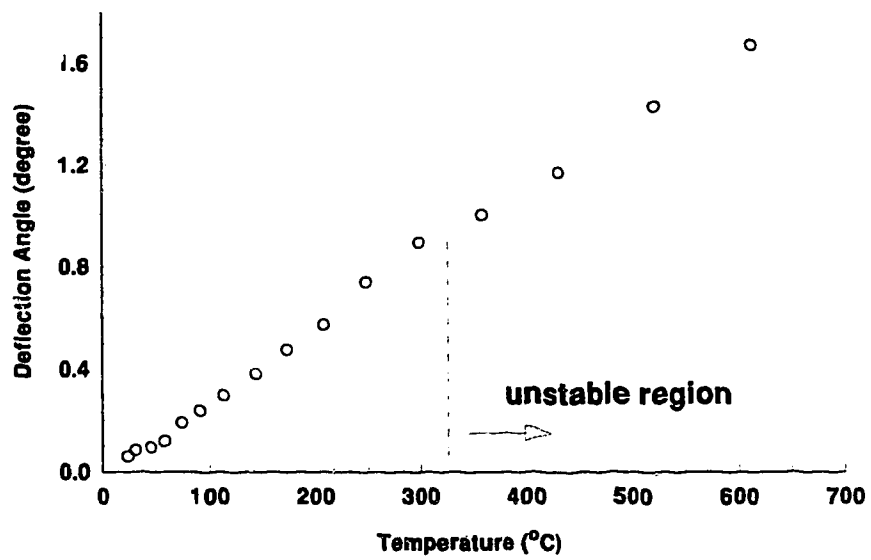


Figure 5.6: Mirror deflection variation with the average temperature of the driving beams.

shown in Figure 5.4. The movement of the reflection laser spot was captured by a Kodak high speed video camera. The time for the reflection to move from the rest location to the deflected location is approximately 3 ms. This value is consistent with the thermal response time measurements discussed in Chapter 4.

Even though the maximum deflection achieved from the experiment is 1.7° , the driving beams need to be heated to over 600°C to reach this magnitude of deflection. At this temperature, the electrical and mechanical properties of the materials composing the support beam become highly unstable: the resistance of the heating polysilicon resistor varies with time, making it difficult to keep the dissipated heating power constant; and the driving beams are plastically deformed and irrecoverable plastic deflection occurs [8]. As a result, elastic deflection at high temperature is neither repeatable nor controllable. Based on Table 3.1, the operating temperature of polysilicon should be kept below 350°C . Figure 5.6 indicates the unstable region where the temperature is higher than 330°C . Therefore the usable maximum deflection for this particular device is about 1° .

Optimization on deflection angle has been reported by including two layers of aluminum on top of the driving beams, leaving out both the intermediate oxide and the top passivation layers [90]. The purpose of the design is to utilize the large thermal expansion coefficient of aluminum for the mirror actuation. Deflection as large as 6° were observed and again the reproducibility is questioned [90]. Another obvious problem with the design is how to protect the aluminum lines from being attacked by the postprocessing etching because both EDP and TMAH etch aluminum [92].

Using XeF_2 as the silicon etchant, electrostatically actuated flip-mirror devices have been built in standard CMOS process. Reference [100] gives a detailed introduction in this area.

5.2 Magnetically Actuated Devices

Most movable structures realized using the CMOS process are thermally activated as discussed in the previous section. Obvious drawbacks of thermal actuation include:

- Slow response times. Discussions in Chapter 4 indicate that the response time of the device under external thermal excitation is several milliseconds. Heat transfer mechanisms limits response speed of thermal actuation.
- Unidirectional motion. The bending direction of the thermally actuated devices depends on the thermal expansion coefficients of the materials. Once the structure is fabricated, there is no way to change the direction of motion of actuation.
- Small deflection angle. The deflection angle of the thermally activated mirror is small, especially for the stable operation range, to have many practical applications.

The purpose of magnetically activated device (MAD) development is to seek an alternate and better approach to construct a mechanically movable device using the simple and economical CMOS process. The magnitude, speed and controllability of the achieved movement are expected to be improved significantly over the thermally activated devices.

5.2.1 Magnetic Actuation

The magnetic force has been utilized in the operation of electric motors for more than a century. In general, when a current-carrying conductor lies in a magnetic

field, magnetic forces are exerted on the moving charges within the conductor. These forces are transmitted to the material of the conductor, and the conductor as a whole experiences a force distributed along its length. If a straight wire of length l is in a magnetic field B , the magnetic force, also called the Lorentz force, can be formulated as

$$\vec{F} = I_l \vec{l} \times \vec{B} \quad (5.2)$$

where I_l is the electrical current flowing through the wire. The direction of the force can be easily reversed by making the current flow in the opposite direction. This feature makes magnetic actuation flexible and controllable. Magnetic force appears simultaneously with the presence of the electrical current. Thus the response time of a magnetically actuated device is only determined by the mechanical properties and geometries of the structure. However, the question remains: how much deflection can a typical magnetic force bring to a structure, and if the deflection is too small, how to improve it?

5.2.2 Deflection actuation

A simple and essential cantilever structure for a magnetically actuated mirror is shown in Figure 5.7, where the electrical wire and magnetic field direction are also illustrated. The structure is similar to the thermally actuated mirror discussed in Section 5.4.1 for the purpose of reducing the bending load while keeping the mirror plate flat. A dielectric platform containing a rectangular metal layer as a optical mirror was supported by two parallel support arms. The metal lead is distributed as in Figure 5.7 in such a way that a current flowing through it interacts with the external magnetic field applied parallel to the support arms and results in a vertical displacement and rotation at the free end of the cantilever due to the generated

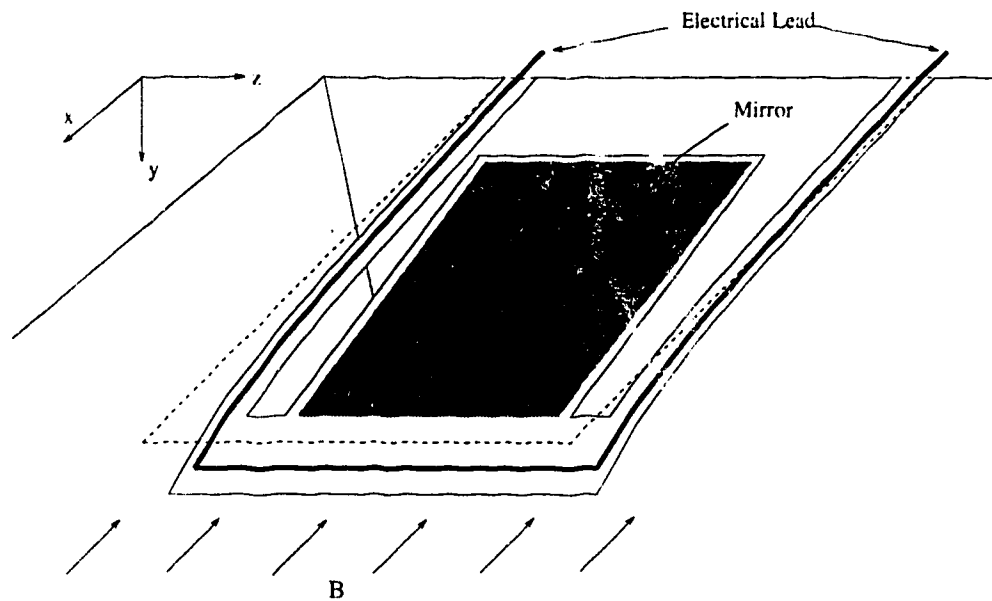


Figure 5.7: A simple magnetic activated mirror device structure.

Lorentz force. The small contact regions between the suspensions and the mirror plate produce the same rotation of the mirror as that of the free end of the support arms, if the effect of gravity is ignored.

The displacement and deflected angle of the free end of the cantilever can be estimated by replacing the distributed force along the end of the cantilever by two concentrated forces at the two outer corners of the cantilever. The problem is therefore simplified to determining the deflection of a simple cantilever under a concentrated force, as shown in Figure 5.8(a).

If the deflection is small, the equation describing the elastic curve of Figure 5.8 (a) is [93]

$$y = \frac{P}{6EI}(3Lx^2 - x^3) \quad (5.3)$$

where E is Young's modulus of the material forming the cantilever, I denotes

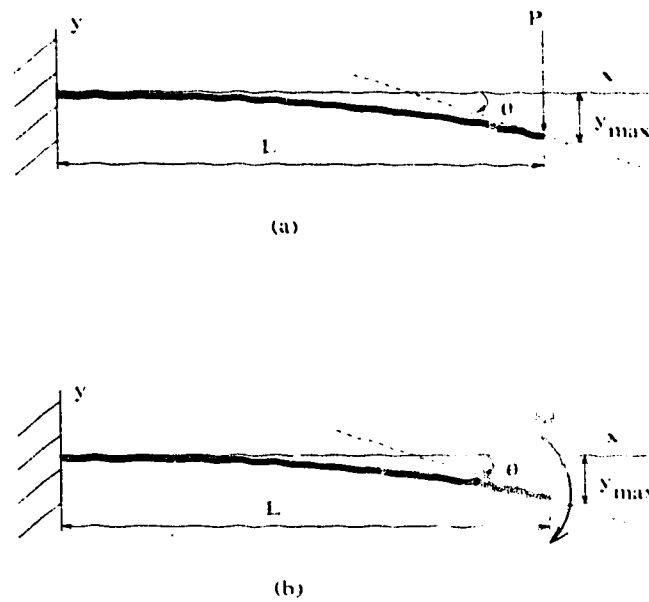


Figure 5.8: Cantilever deflection under concentrated force P (a) and concentrated moment M (b).

the moment of inertia of the cantilever cross-section area, L represents the total length of the cantilever, and the acting force is P . For the cantilever tip, $x = L$; the displacement is

$$y_{max} = \frac{PL^3}{3EI} \quad (5.4)$$

and the deflected angle is

$$\theta = \frac{PL^2}{2EI} \quad (5.5)$$

The deflection of a cantilever under a concentrated moment at the free end, as shown in Figure 5.8 (b), is not directly related to the analysis of the structure in Figure 5.7. However, it is part of the fundamentals for the deflection calculation of a cantilever-in-cantilever (CIC) structure, which will be discussed later. The

equation describing the elastic curve in Figure 5.8 (b) is

$$y = \frac{M}{2EI}x^2 \quad (5.6)$$

where M is the acting moment. Thus the cantilever tip displacement and deflected angle are [93]

$$y_{max} = \frac{ML^2}{2EI} \quad (5.7)$$

and

$$\theta = \frac{ML}{EI} \quad (5.8)$$

respectively. It should be noted that for a cantilever with a small deflection, the system is linear. That is, if the cantilever is under more than one load, the deflection at any part of the structure is equal to the algebraic sum of the deflection that each load has introduced independently.

Returning to the structure in Figure 5.7 and assuming the device was fabricated using the CMOS process, the mechanical properties of the suspension arms, such as Young's modulus and density, of the different CMOS-compatible materials are approximated with the corresponding bulk values as given in Table 5.1 and the thickness of the thin film layers forming the structure are from the process data.

The cross section of the support arm is illustrated in Figure 5.9 (a), where the vertical dimension is obtained from the CMOS $1.5 \mu\text{m}$ process data [94] provided by Mitel, and the arm width w is determined by the layout design. Due to the similar Young's modulus E between the silicon dioxide and the aluminum as indicated in Table 5.1, the oxide section of the beam, containing the aluminum lead, can

Table 5.1: Mechanical properties of CMOS thin film materials

Material	Young's Modulus (GPa)	Density (g/cm^3)
Polysilicon	168	2.3
Silicon Dioxide	74	2.2
Silicon Nitride	320	2.8
Aluminum	72	2.7

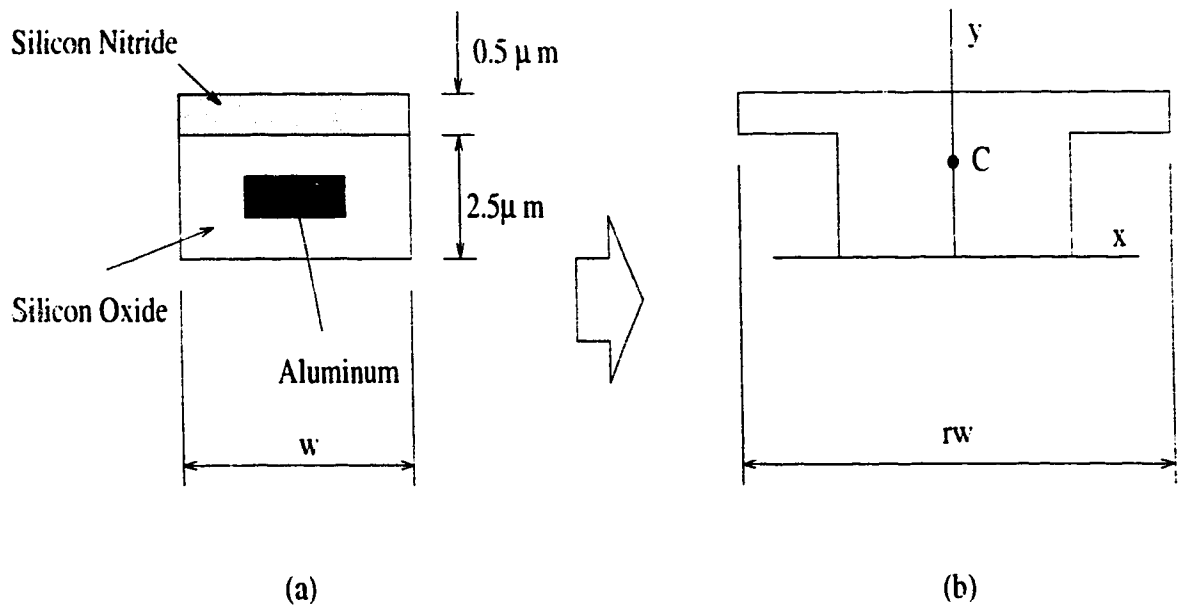


Figure 5.9: Cross section of the support arm: (a) original; (b) transformed.

be regarded as a homogeneous material. To calculate the moment of inertia of the arm [93], the nitride portion has to be transformed to have the same Young's modulus as the oxide portion by scaling its width by a factor of r , which is the ratio of the elastic modulus of nitride to the oxide (E_{ni}/E_{ox}). The transformed support arm cross section is shown in Figure 5.9 (b). The centroid C is located at

$$y_C = \frac{r \times 0.5 \times 2.75 + 2.5 \times 1.25}{r \times 0.5 + 2.5} \quad (5.9)$$

where $r = E_{ni}/E_{ox} = 4.324$. Inserting the value of r gives $y_C = 1.9456 \mu\text{m}$. The moment of inertia I of the area shown in Figure 5.9 (b) with respect to the centroid is

$$\begin{aligned} I(w) &= \frac{1}{12}(rw) \times (0.5)^3 + 0.5 \times (rw) \times (0.8044)^2 \\ &\quad + \frac{1}{12}w \times (2.5)^3 + 2.5 \times w \times (0.6956)^2 \\ &= 3.9557w \text{ } [\mu\text{m}^4] \end{aligned} \quad (5.10)$$

where w is the width of the support arm in μm .

Choosing typical values of the geometric and operating conditions for the structure shown in Figure 5.7 will yield the mirror deflection angle by using Equation (5.5). For example, if the current flowing through the structure is 10 mA, the external magnetic field intensity is 0.1 T, and the length of the electric wire perpendicular the magnetic field is $200 \mu\text{m}$, the generated Lorentz force $F = I_l B = 2 \times 10^{-7} \text{ N}$. Half of that force will act on each of the two arms, i.e. $P = F/2 = 1 \times 10^{-7} \text{ N}$. Assume that the arm width $w = 12 \mu\text{m}$ and length $L = 180 \mu\text{m}$, the deflection angle of the mirror will be

$$\theta = \frac{1 \times 10^{-7} \times 180^2}{2 \times 74 \times 10^{-3} \times 3.9557 \times 12} = 5.6937 \times 10^{-4} \text{ } [rad] = 0.03262^\circ$$

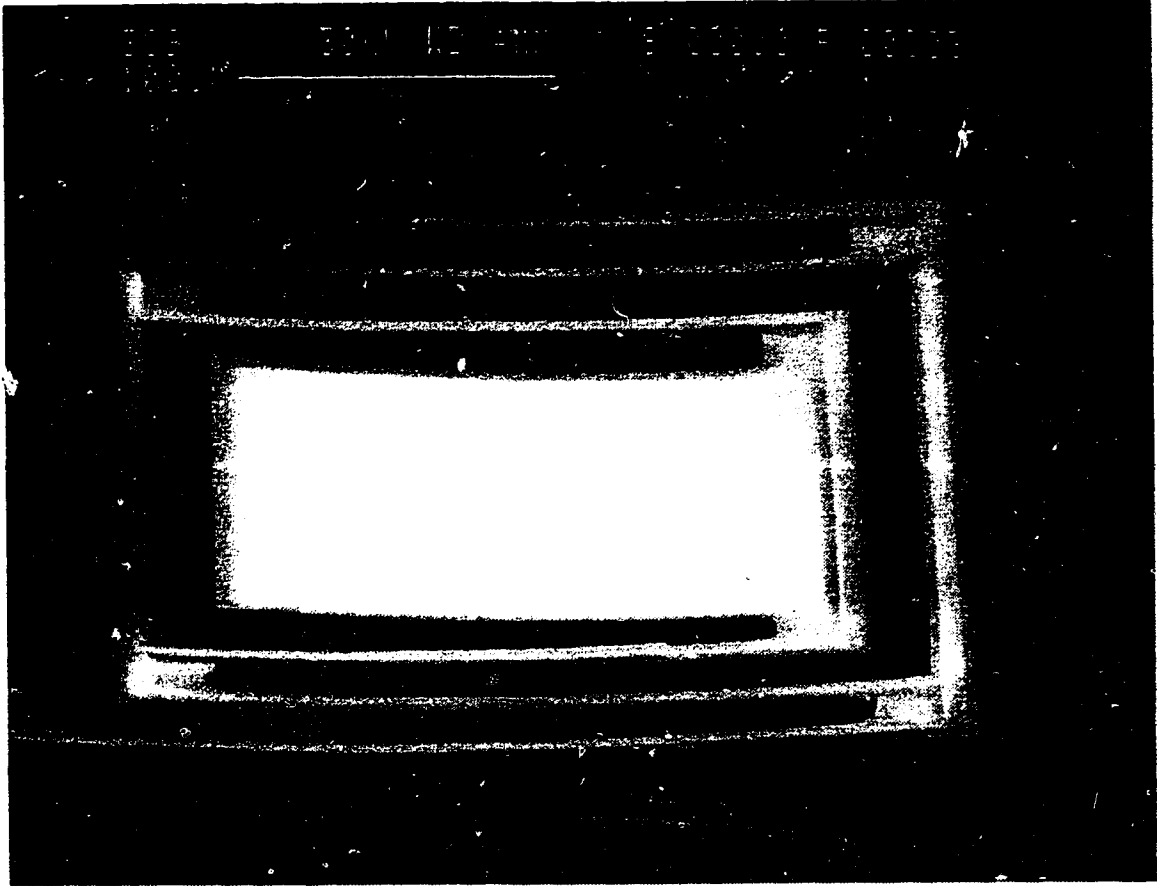


Figure 5.10: SEM picture of a triple CIC device.

and the displacement

$$y_{max} = 0.0553\mu m$$

5.2.3 Deflection Enhancement – CIC Structure

The estimations above point out that the magnitude of deflection for a simple cantilever structure is too small to have many potential applications. The cantilever-

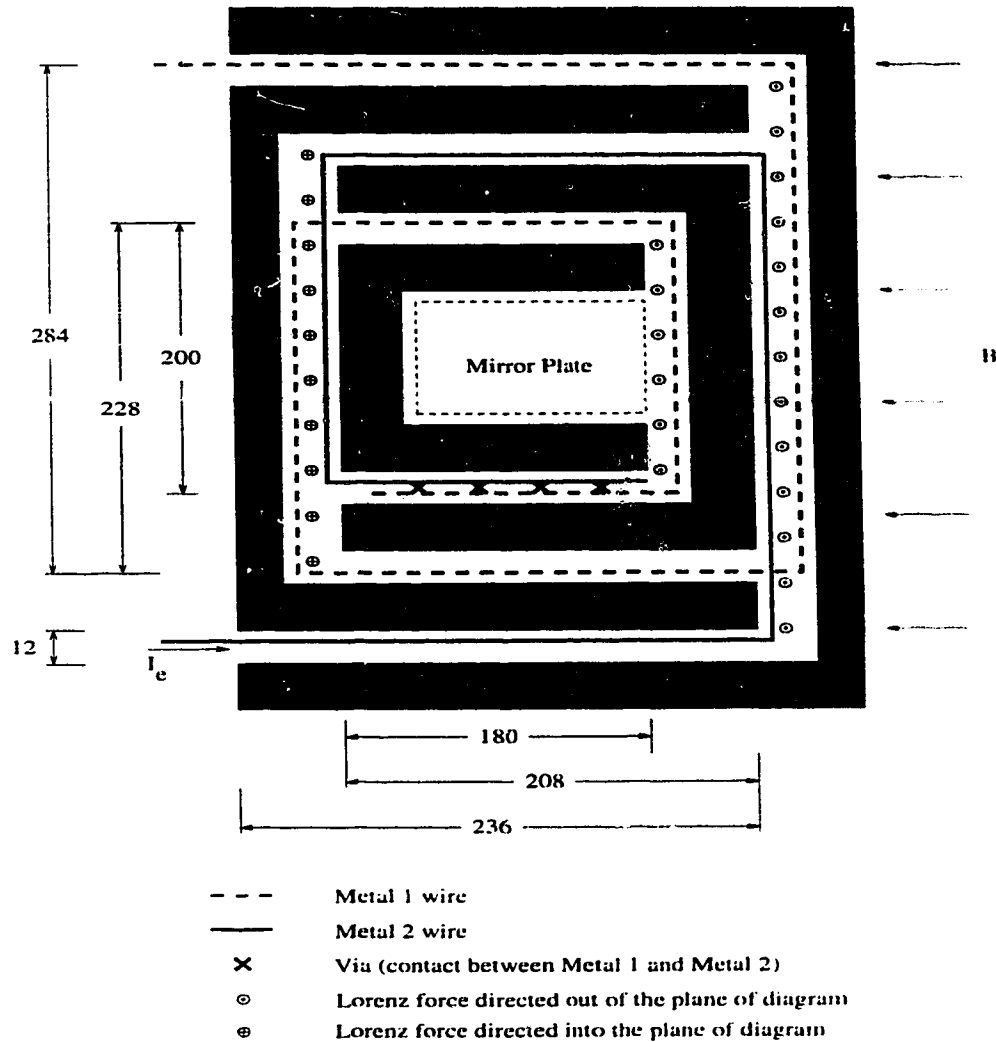


Figure 5.11: Triple CIC plan view and metal layers arrangement (in regions where metal1 and metal2 leads are side-by-side, they actually overlap each other in the real device).

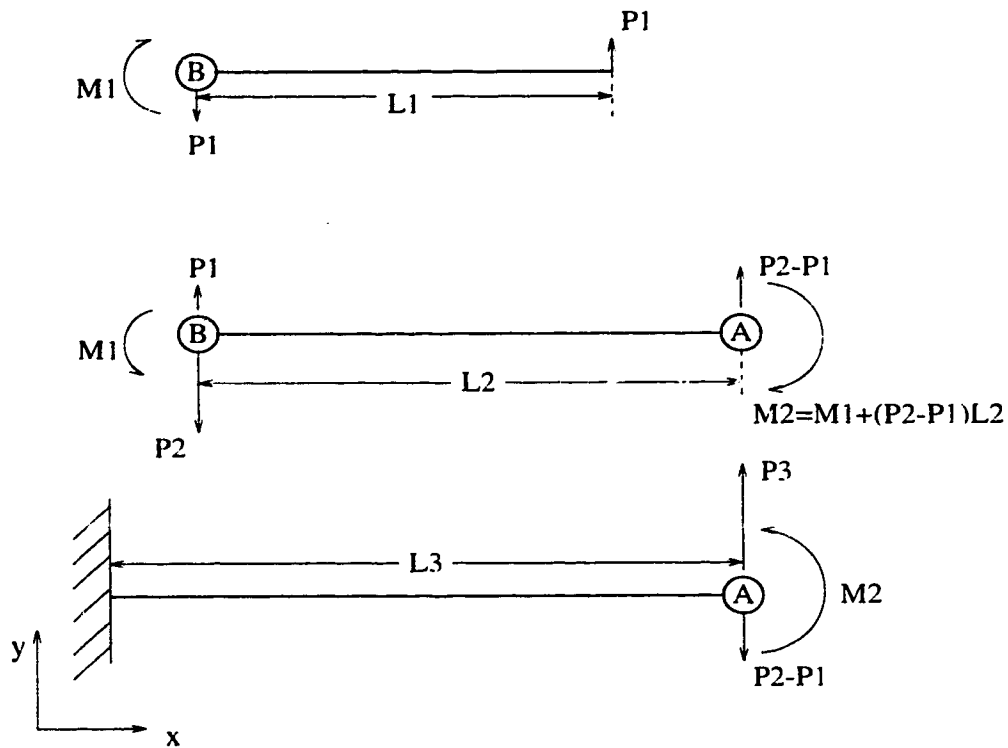


Figure 5.12: Deflection estimation for triple CIC structure.

in-cantilever (CIC) structures are developed to enhance the deflection. A SEM picture of the triple CIC device fabricated using the Northern Telecom $1.2 \mu\text{m}$ CMOS process is shown in Figure 5.10. The central cantilever is embedded in the surrounding cantilever, which in turn is embedded sequentially in two other surrounding cantilevers. The metal1 and metal2 layers of the CMOS process are used to form a coil conducting current around the peripheries of the cantilevers. The metal wires are arranged in such a pattern as shown in Figure 5.11 that the Lorentz forces generated on the two ends of the cantilever always have opposite directions. The following analysis will demonstrate that the magnetic forces will pass on and, most importantly, *amplify* the moment generated on the central cantilever through the cascaded cantilever structure.

The triple cantilever-in-cantilever structure is approximated by three simple cas-

caded cantilevers as shown in Figure 5.12, where the three cantilevers from the top to the bottom represent the inner, intermediate and outer cantilevers of Figure 5.11 respectively. The top cantilever is attached to with the middle one at point B , and the bottom and middle cantilevers are joined at point A . Figure 5.12 also illustrates the free-body force diagrams for those cantilevers. The Lorentz forces generated by the electrical current and the external magnetic field are approximated by the concentrated forces, namely P_1 , P_2 and P_3 for the three support structures on the ends of the cantilevers as shown in Figure 5.12. Assuming that the magnetic field intensity is evenly distributed along the surface of the device, the directions of forces P_1 and P_3 are always the same and opposite with that of P_2 . For the absolute values of these forces, $P_3 > P_2 > P_1$, due to the geometry of the device.

The displacement and the deflection angle of the top cantilever with respect to point B in Figure 5.12 can be calculated using Equation (5.4) and (5.5) directly

$$y_{max1} = \frac{P_1 L_1^3}{3EI}, \quad \theta_1 = \frac{P_1 L_1^2}{2EI} \quad (5.11)$$

where L_1 is the length of the top cantilever.

Considering the second cantilever, the deflection of point B with respect to A is composed of two parts. The deflection introduced by the moment $M_1 = P_1 L_1$ is formulated using Equation (5.7) and (5.8)

$$y'_{max2} = \frac{M_1 L_2^2}{2EI} = \frac{P_1 L_1 L_2^2}{2EI}, \quad \theta'_2 = \frac{M_1 L_2}{EI} = \frac{P_1 L_1 L_2}{EI} \quad (5.12)$$

and the deflection caused by the unbalanced force ($P_2 - P_1$) is

$$y''_{max2} = \frac{(P_2 - P_1) L_2^3}{3EI}, \quad \theta''_2 = \frac{(P_2 - P_1) L_2^2}{2EI} \quad (5.13)$$

in both equations. L_2 denotes the length of the second cantilever. Thus the total deflection of the second cantilever is

$$y_{max2} = y'_{max2} + y''_{max2} = \frac{P_1 L_1 L_2^2}{2EI} + \frac{(P_2 - P_1)L_2^3}{3EI}$$

$$\theta_2 = \theta'_2 + \theta''_2 = \frac{P_1 L_1 L_2}{EI} + \frac{(P_2 - P_1)L_2^2}{2EI} \quad (5.14)$$

Similarly, the deflection of the bottom cantilever is calculated using the net force and moment acting on point A . From the force diagram in Figure 5.12, the moment concentrated at A is $M_2 = P_1 L_1 + (P_2 - P_1)L_2$, and the net force is $P_3 - (P_2 - P_1)$. Thus the deflection of point A with respect to the clamped end is

$$y_{max3} = \frac{[P_1 L_1 + (P_2 - P_1)L_2] L_3^2}{2EI} + \frac{[P_3 - (P_2 - P_1)] L_3^3}{3EI}$$

$$\theta_3 = \frac{[P_1 L_1 + (P_2 - P_1)L_2] L_3}{EI} + \frac{[P_3 - (P_2 - P_1)] L_3^2}{2EI} \quad (5.15)$$

Notice the the directions of the displacements and rotations, the total deflection of the mirror plate with respect to the substrate is

$$y_{max} = y_{max1} - y_{max2} + y_{max3}$$

$$= \frac{P_1 L_1^3 - (P_2 - P_1)L_2^3 + [P_3 - (P_2 - P_1)] L_3^3}{3EI}$$

$$+ \frac{-P_1 L_1 L_2^2 + [P_1 L_1 + (P_2 - P_1)L_2] L_3^2}{2EI}$$

$$\theta = \theta_1 + \theta_2 + \theta_3$$

$$= \frac{P_1 L_1^2 + (P_2 - P_1)L_2^2 + [P_3 - (P_2 - P_1)] L_3^2}{2EI}$$

$$+ \frac{P_1 L_1 L_2 + [P_1 L_1 + (P_2 - P_1)L_2] L_3}{EI} \quad (5.16)$$

For a CIC structure containing n cantilevers, its deflection can be formulated as

$$y_{max} = \frac{\sum_{i=1}^n (-1)^{i+1} F_i L_i^3}{3EI} + \frac{\sum_{i=1}^{n-1} (-1)^i M_i L_{i+1}^2}{2EI}$$

$$\theta = \frac{\sum_{i=1}^n F_i L_i^2}{2EI} + \frac{\sum_{i=1}^{n-1} M_i L_{i+1}}{EI} \quad (5.17)$$

where

$$F_1 = P_1;$$

$$F_i = P_i - F_{i-1}, \text{ for } i > 1;$$

$$M_i = \sum_{j=1}^i F_j L_j$$

The conclusions drawn from Equation (5.17) are summarized as:

- The deflection of the central cantilever (mirror plate) of a CIC structure is the accumulation of the deflection of all the surrounding cantilevers. The vertical displacements of any two successive cantilevers are always in opposite directions making the accumulation not necessarily act in favour of increasing displacement magnitude. For the rotation angle, however, all the cantilevers contribute to the accumulation in the same direction. This property makes the CIC structure extremely effective in enhancing the deflection angle.
- The total deflection is proportional to the Lorentz force generated within each cantilever and therefore the magnetic field intensity B and the input current I_e .
- The moment generated at the central cantilever $M_1 = P_1 L_1$ is cascaded to the outer cantilever through the cantilevers in between. The moment is

enlarged at each stage. For example, the acting moment at the third stage, the bottom cantilever in Figure 5.12, is larger than M_1 by $(P_2 - P_1)L_2$. As a consequence, the maximum moment occurs at the fixed ends of the outer cantilever suspensions, and so do the highest stresses and strains. Thus they are the best locations to place the piezoresistive sensors.

- Due to the effect of the deflection accumulation and the moment enlargement, the CIC structures dramatically improve the deflection magnitude over the simple cantilever structure under the same operating conditions. The more embedded cantilevers there are, the more the attainable angular deflection.

Using the geometric dimensions shown in Figure 5.11, it is possible to estimate the deflection of this particular device. If the electrical current flowing through the coil $I_c = 10 \text{ mA}$ and the external magnetic field $B = 0.1 \text{ T}$,

$$P_1 = 1 \times 10^{-7} \text{ N}, \quad P_2 = 2.28 \times 10^{-7} \text{ N}, \quad \text{and} \quad P_3 = 2.84 \times 10^{-7} \text{ N}$$

$$L_1 = 180 \text{ } \mu\text{m}, \quad L_2 = 208 \text{ } \mu\text{m}, \quad \text{and} \quad L_3 = 236 \text{ } \mu\text{m}$$

As the suspension width $w = 12 \text{ } \mu\text{m}$, the moment of inertia for the structure is

$$I = 3.9557 \times 12 = 47.4684 \text{ } [\mu\text{m}^4]$$

Inserting above values into Equation (5.16) obtains

$$y_{max} = 0.3835 \text{ } \mu\text{m}$$

$$\theta = 6.5501 \times 10^{-3} \text{ } [rad] = 0.3753^\circ$$

Notice that the central cantilever is identical to the structure discussed before as an example of a single cantilever structure, and thus the triple CIC design has enhanced the deflection by more than ten times.

5.2.4 Experiments and Analysis

The magnetically activated mirror devices were fabricated using the CMOS 1.2 μm double metal process offered by Northern Telecom. The free standing CIC cantilevers were released by postprocessing etching performed at the Alberta Microelectronic Centre.

Two types of CIC devices were made. Figure 5.10 shows the triple CIC device where three active cantilevers have been embedded. The double CIC device is similar to the triple except it has one less embedded cantilever. The experimental setup to perform the measurements on the CIC devices is similar to that shown in Figure 5.4 except the chip with the devices is placed in between the two poles of a permanent magnet. The magnetic field has a measured value of 0.12 T for all the measurements and it is in the direction indicated in Figure 5.11. A beam from a helium-neon laser is focused onto the center of the cantilever mirror and the reflected beam falls on an opaque screen or a photo-detector. The angle of the cantilever is determined by the position of the reflected laser beam and the geometry of the system and the time of mirror movement is measured by monitoring the movement of the laser beam. DC and square wave AC currents are applied to determine the static and dynamic response of the devices.

Mirror Deflection

To activate the mirror deflection, high current (usually higher than 10 mA) is necessary and thus Joule heating on the suspensions cannot be avoided. Figure 5.13 plots the average temperature increase of the support arms of a triple CIC cantilever against the input current. An input current of 20 mA will heat the support arms to approximately 150°C above the room temperature. Thus the mirror deflection is activated not only by the Lorentz force but by the thermal

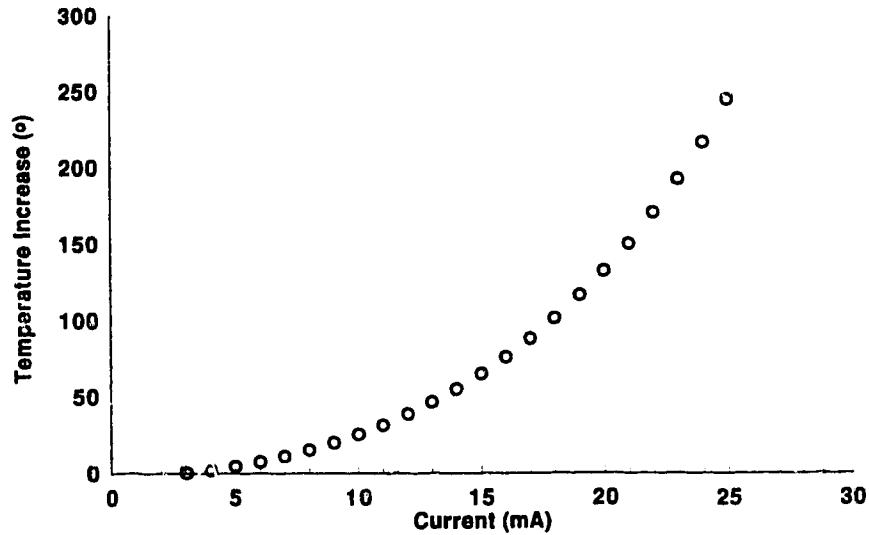


Figure 5.13: Temperature increase of support arms versus the input current.

multi-morph effect (see discussions in Section 5.1.4). To extract the magnetic effect, the measurement on the two reflected beam positions produced by the same current flowing in opposite directions is used to determine the cantilever deflection. The thermally activated deflection depends only on the dissipated electrical energy but not the current direction.

Figure 5.14 displays the tilt of the two types of devices as a function of DC current, where the tilt represents the total angular displacement by reversing the DC current. The deflection for both devices is linear with respect to the current as predicted by the analytic estimations in the previous sections. For the triple CIC structure, the measured deflection at $I_c = 10mA$ is about 0.5° , half the value of the tilt shown in the plot. The analytic model predicts a deflection of 0.3753° at $B = 0.1T$. Consider the stronger magnetic field in the experiment ($B = 0.12T$),

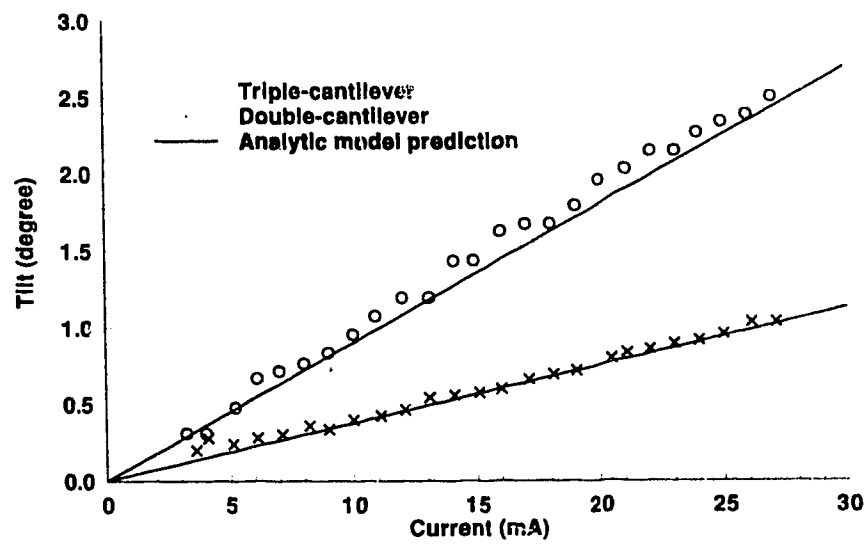


Figure 5.14: Mirror tilt variation with the input current.

the model estimates a deflection of $0.3753^\circ \times (0.12/0.1) = 0.45^\circ$. Measurement errors, thin film material property approximations and the model crudity contribute to the 10% inconsistency.

Response Time Measurement

The response time of a deflectable mirror is a crucial parameter for many practical applications, such as the applications in projective display systems, optical switches, and optical shutters. Accurate measurement of the velocity profile of the mirror during its deflection is very difficult. However, the simple experiment discussed in this section reveals fairly well the response time and the dynamic response of the device.

The experimental setup is similar to that used to measure the static deflection, except that the reflected laser beam falls on a photodiode rather than the opaque screen. The object of the experiment is to measure the switching speed of the reflected laser beam. The photodetector is positioned so that the edge of the reflected laser beam, as shown in Figure 5.15, will be moving inside the detector diaphragm region. As a consequence, the radiation flux passing through the diaphragm, and hence the detector output, will depend on the position of the light spot. For the situation drawn in Figure 5.15, the mirror in the up position allows maximum amount of radiation to fall on the detector while the mirror in down position minimizes the detector output signal. Although the relationship between the light spot displacement and the photodiode signal is nonlinear, the measurement is a good indication of the performance of the devices in the time domain as long as their variations are monotonic.

The mirror was driven by a square wave AC current of 6.7 mA. The output signal of the photodetector was sampled and collected using a digital oscilloscope. The

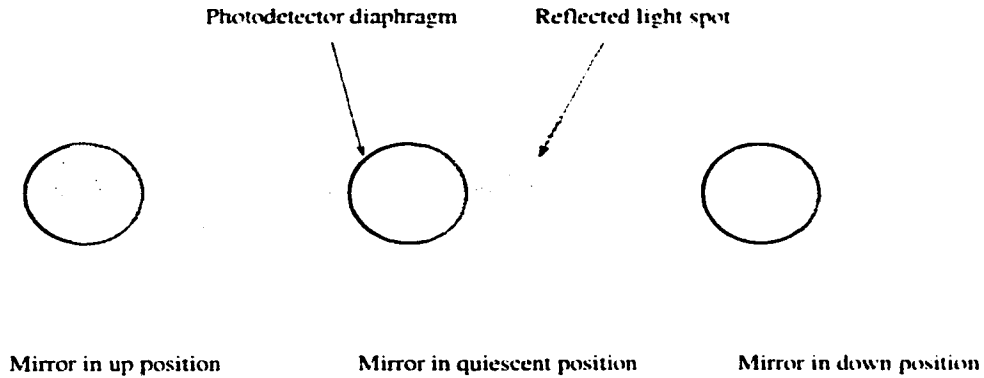


Figure 5.15: Photodetector arrangement for mirror response time measurement.

upper oscilloscope trace in Figure 5.16 displays the detector signal at a driving frequency of 102 Hz, while the lower trace indicates the driving current. After the current switches direction, oscillations are excited and then damped. Eventually the mirror plate settles after about 2.5 ms.

Figure 5.17 shows the signal on a shorter time scale. The measured response time during which the mirror swings from the still stage to its first oscillating peak is about 28 μs . The movement of the mirror can be regarded as damped free-vibration response of the CIC structure. For a system having a single degree of freedom, the equation governing the free-vibrating motion is formulated as [95]:

$$m \frac{d^2 y(t)}{dt^2} + c \frac{dy(t)}{dt} + ky(t) = 0 \quad (5.18)$$

where m , c , and k are the effective mass, damping constant and stiffness of the system respectively; $y(t)$ denotes the displacement at time t . The general solution for Equation (5.18) is

$$y(t) = G e^{st} \quad (5.19)$$

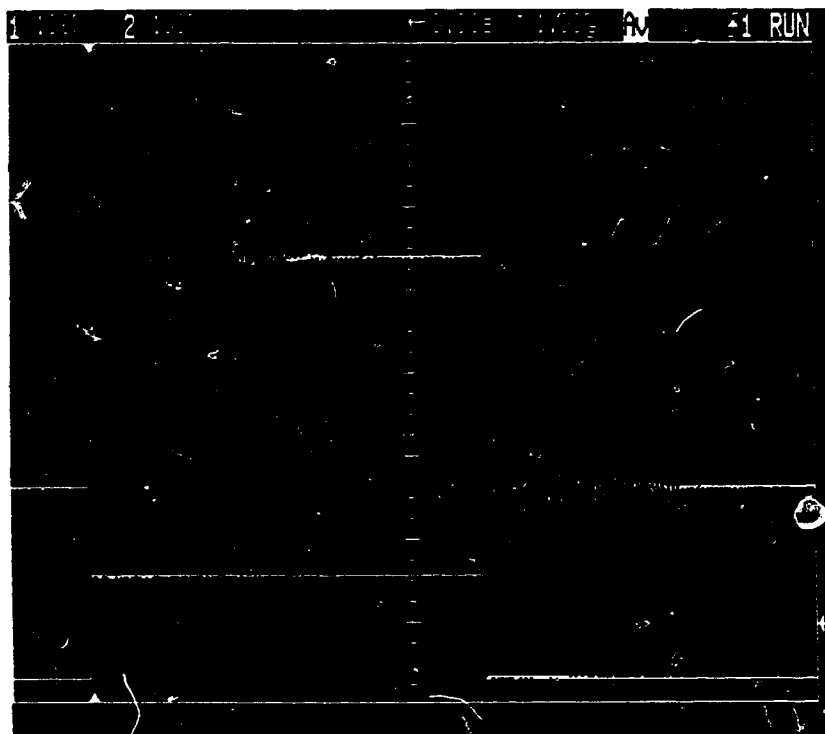


Figure 5.16: Photodetector output (upper trace) as mirror is excited by an AC square wave current at 102 Hz (lower trace).

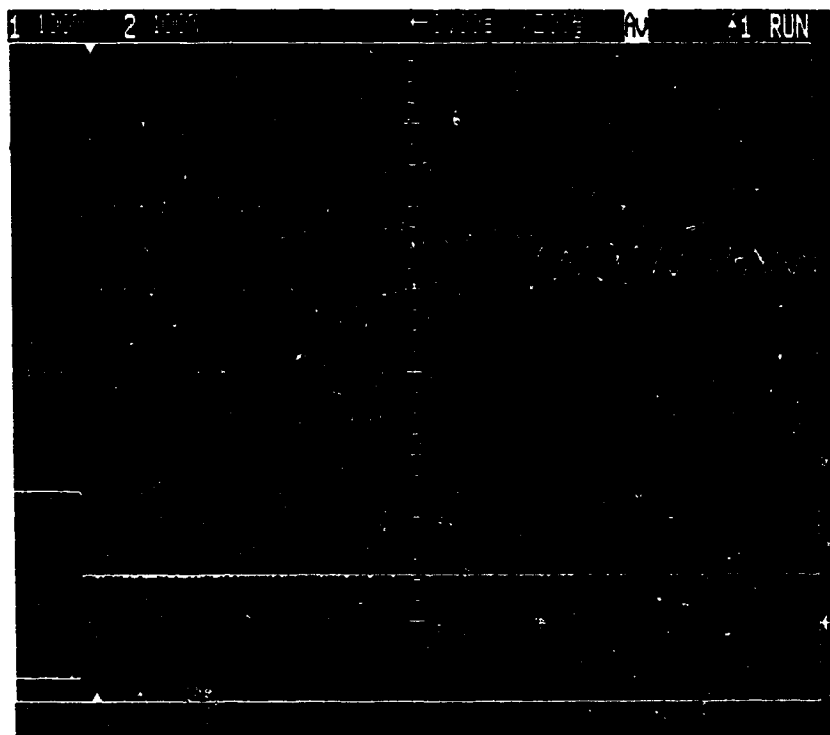


Figure 5.17: Close-up look of Figure 5.16.

where s satisfies

$$s^2 + \frac{c}{m}s + \omega_0^2 = 0 \quad (5.20)$$

with

$$\omega_0^2 = \frac{k}{m} \quad (5.21)$$

ω_0 , the resonant frequency, is the circular frequency at which the system will oscillate without damping.

If damping is present in the system,

$$s = -\frac{c}{2m} \pm \left[\left(\frac{c}{2m} \right)^2 - \omega_0^2 \right]^{\frac{1}{2}} \quad (5.22)$$

and the damping ratio ξ is defined as:

$$\xi = \frac{c}{2m\omega_0} \quad (5.23)$$

For an underdamped system ($\xi < 1$),

$$s = -\xi\omega_0 \pm i\omega_D \quad (5.24)$$

where

$$\omega_D = \omega_0 (1 - \xi^2)^{\frac{1}{2}} \quad (5.25)$$

Thus the solution for Equation (5.18) is

$$y(t) = e^{-\xi\omega_0 t} (A \sin \omega_D t + B \cos \omega_D t) \quad (5.26)$$

where A and B are the constants determined by the initial and boundary conditions.

It is tempting to obtain the device damping ratio from the response shown in Figure 5.17. Reference [95] has given an approximate method using the vibration amplitudes provided the free-vibrating motion is a single exponential decaying harmonic oscillation, as predicted by Equation (5.26). Referring to Figure 5.17, the enveloping curve imposed on the responses is, however, non-exponential, probably due to the beating or interaction between the higher order vibrations [96]. In addition, the vibration amplitude shown in the measurement is not proportional to the actual displacements of the structure. Thus determining the damping ratio using amplitude decay is prone to significant error. However, the damped vibrational frequency can be easily measured using the experimental response. The measured value of the cyclic frequency f_D is 16.875 kHz, which, in combination of the resonance frequency discussed in the next section, can be used to estimate the damping ratio ξ .

Resonant Response

The deflection of an electrostatically actuated device is always a fixed value even under resonant excitation because its free moving distance is determined by the positions of the landing electrodes. The electrostatic torque is inversely proportional to the square of the electrode separation [74], so a usable electrostatic torque often implies limited electrode separation and hence limited deflection. Unlike electrostatically actuated mirror device, a magnetic CIC structure has the potential to be activated at its resonant frequency to achieve large deflection, since its free moving distance is only constrained by the geometry of the etched cavity, which can readily be made quite large. The frequency response around the resonance was measured using the same experimental setup as for the static deflection measurement. Square wave AC currents were applied to excite the oscillation. The reflected beam was fan-shaped and the spread angle and hence the mirror deflection varied with the

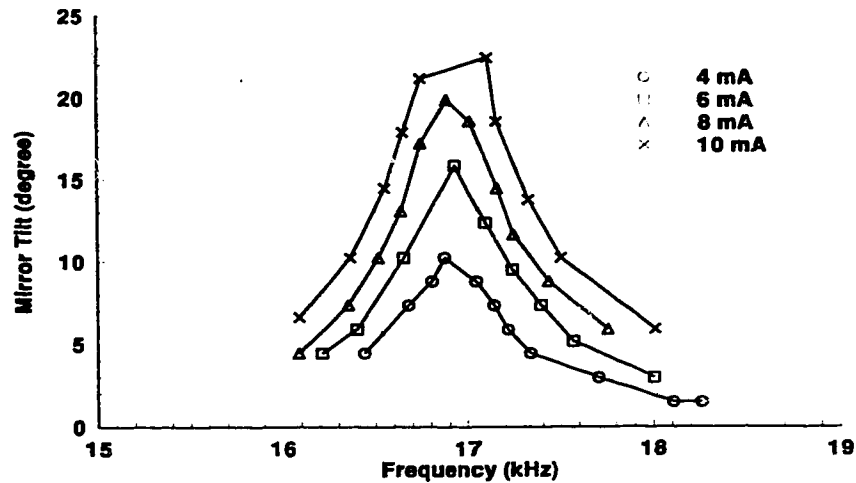


Figure 5.18: Triple CIC structure frequency response.

frequency and the magnitude of the input current.

Figure 5.18 plots the variation of the tilt of the triple structure mirror against the driving frequency at different magnitudes of AC current. The measured resonant frequency f_0 is approximately 17 kHz. Using Equation (5.25) and the value of f_D obtained from the previous section, the damping ratio ξ of the structure is calculated as 0.12. The measured maximum deflections are about 10° , 16° and 20° for the currents of 4 mA, 6 mA, and 8 mA respectively. At 10 mA, the mirror plate strikes the bottom of the etched pit, which has depth of $50 \mu\text{m}$, limiting its deflection to 25° . The measured Q factor of the structure is approximately 35. Figure 5.19 shows the response for a double cantilever structure which has a resonant frequency of 25.3 kHz and a Q of 90.

The triple CIC device has been operated at resonance under driving current of 8

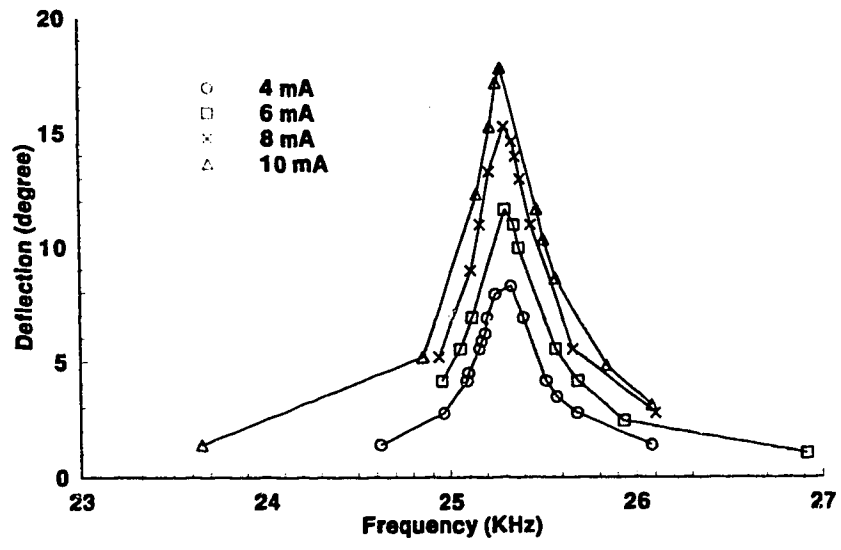


Figure 5.19: Double CIC structure frequency response.

mA continuously for 17 days (2.5×10^{10} oscillations). No visible structure defects and no change in the deflection characteristics were observed afterward.

The device is rich in resonant frequencies. For another triple-CIC structure, Table 5.2 lists some of them. Both sinusoidal and square-wave AC currents of $I_{rms} = 8.0 \text{ mA}$ were used to drive the device. No sinusoidal resonances were observed below 13.2 kHz, while the square wave excitation produces several, which are presumably due to the high order components carried by the AC square wave.

The small resonances near 34.6 kHz labeled orthogonal indicates an oscillation that was in the direction orthogonal to all the other resonances, and represents a lateral oscillation. This may be due to the slight asymmetry in the metal leads of the device: the metal1 to metal2 via is on the arm of the cantilever (see Figure 5.11) rather than at the end of the cantilever, producing a center of mass of the device that is slightly off the geometric line of symmetry. Slight mis-alignment of the external magnetic field with the CIC structure may also contribute to the phenomenon.

Another interesting phenomenon is a dip in the average temperature of the support arms when the device is at its resonance. It has been observed that the average temperature of the support arms of a triple CIC structure, as it was driven through resonance by an AC square-wave current of 10 mA, decreased by approximately 0.5°C at resonance. Figure 5.20 displays the temperature variation of the support arms versus the driven frequency. The temperature values were obtained by measuring the resistance of the aluminum coil using a DMM, which would average out any AC signals associated with large oscillations, such as piezoresistance and back emf effects. At resonance, the mirror plate acts like an electrical fan due to the large magnitude of its deflection and it pushes the ambient air much faster and cools down the device.

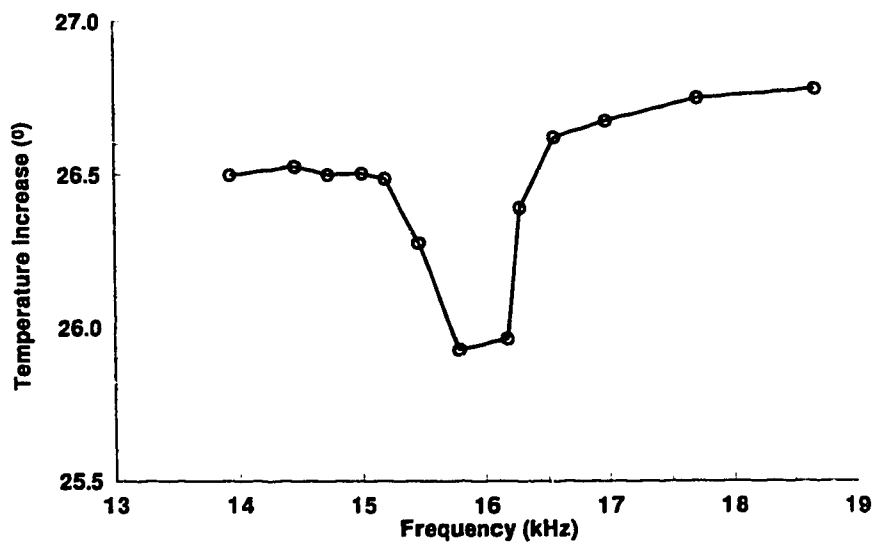


Figure 5.20: Temperature increase of the support arms versus driven frequency.

Table 5.2: Frequency response of a triple-CIC structure ($I_{rms} = 8.0 \text{ mA}$).

Square-wave AC excitation		Sinusoidal AC excitation	
Frequency (kHz)	Deflection ($^\circ$)	Frequency (kHz)	Deflection ($^\circ$)
2.23	4.57		
3.20	6.09		
4.45	4.57		
5.23	9.09		
7.30	3.05		
13.20	10.57	13.23	9.83
15.90	26.57	16.03	20.81
34.60	(orthogonal)	34.34	(orthogonal)
36.50	7.59	36.46	6.09
56.80	3.81	56.78	3.81

5.2.5 Potential Applications

The novel design and actuation techniques of the CIC structures extend their applications beyond the areas covered by the conventional deflectable mirror devices. Those possible applications are summarized in the following:

- Resonator sensor. The resonant frequency of the structure is sensitive to a variety of measurands, such as ambient temperature and pressure and mass of the moving structure. Thus the CIC device can be designed as a temperature or pressure sensor. The sub-nanogram mass sensor discussed in Section 5.1.1 can be replaced by CIC device to eliminate the need for the vibrating table. Inside a thin film deposition chamber, CIC perhaps could be used as an in-situ monitor for the film thickness.

- Large spread-angle optical scanner. Large tilt (more than 22°) has been achieved as the CIC structure is excited at its resonant frequency. The device can be used as a miniature optical scanner, a key component in the single detector imaging systems and the single light source display systems.
- Micro-speakers. The motion of deflecting platform can be used to generate an acoustic wave. The operating principle of the magnetic actuation can be adopted to build miniature speakers on the silicon micro-chips.
- Magnetic field sensor. The bending force of the CIC structure is a function of the external magnetic field. Thus the deflection could probably be used to measure the magnetic field intensity.
- Thin film property extraction. The performance of the CIC structures depends on the mechanical properties of the materials forming the structures. Elaborate design and careful analysis will enable one to obtain the mechanical properties of the thin films, such as Young's modulus and the density.

It should be noted that the applications mentioned above are only several preliminary predictions. This is by no means a complete list for the applications of the CIC structure. On the other hand, the feasibility of magnetic actuation for some of the applications listed here needs further investigation.

Chapter 6

Conclusions and Outlook

6.1 Summary of Contributions

Merger of the bulk micromachining technology and the standard CMOS process has introduced an inexpensive and yet powerful approach for microfabrication of micromechanical structures. The success in the construction of several functional microsensor and microactuator structures has prompted many research groups to investigate the performance, characterization and optimization of the CMOS micromechanical devices. Meanwhile, efforts have been made to expand the application areas covered by the CMOS micromachining techniques by building different structures with new operating principles and new functions. In this regard, the work presented in this thesis contains two major parts: the characterization testing and performance improvement on the existing thermally sensitive structures and the development of a novel magnetically activated device.

6.1.1 Thermally Sensitive Structures

As the first generation of CMOS micromachined devices, thermally sensitive structures have many potential applications in the field of sensing and actuating, ranging from a sensor for gas flow or pressure to a radiation emitter.

For this type of device, thermal isolation and therefore its thermal sensitivity is an important parameter essential for fundamental device operation. Using the temperature coefficient of resistance (TCR) of the polysilicon layer offered by the CMOS process, thermal sensitivity of a structure can be easily calculated by measuring the I-V characteristics of the device. The thermal sensitivity of a suspended bridge structure has been tested at ambient pressures of one and zero (nominal) atmospheres. It was found that for this particular device, its thermal sensitivity in vacuum will be ten times as high as at one atmosphere, implying that some 90% of the heat loss is by conduction through the gas. Thus for some applications requiring high thermal sensitivity, such as a radiation sensor, the ambient gas should be eliminated. Thermal sensitivity can also be enhanced by modifying the physical structure of device. For example, replacing the aluminum wire with relatively low thermally conductive polysilicon or increasing the effective length of the support arms or doing both will decrease the heat leakage from the suspended structure and hence improve its thermal sensitivity.

Another important characteristic for thermally sensitive structures is their response time. Due to the miniature mass it carries, a microdevice subject to an external excitation can respond faster than its larger counterparts. Under excitation by both a constant current (CC) and constant power (CP) step, the time-varying responses of a microbridge structure at ambient pressures of 1 atmosphere and 10^{-4} Torr have been examined carefully by monitoring the resistance of an embedded polysilicon resistor. Excitations of various step amplitudes were applied. The aver-

age temperature of the device increased exponentially with time; the inverse time constant varied with the square of the current step amplitude but was constant with power step amplitude. Generally, device response is much faster at one atmosphere than in vacuum for both types of excitation. For the device under test, the typical values of its time constant under the CC excitation range from 2.49 ms to 4.19 ms at one atmosphere and 12.35 ms to 16.91 ms in a vacuum. Its response time under the CP excitation is about 1.03 ms at one atmosphere and 11.56 ms in a vacuum. An analytic model for the CC excitation has been developed and its predictions are consistent with the observations of the experiment. Thermal response time and thermal sensitivity are interconnected for a particular device: improving one of these properties degrades the other.

6.1.2 Magnetically Actuated Device

Although there are many research activities going on for the development of dynamic (movable) micromachined structures, very little progress has been made to date in this area using CMOS micromachining technology. Almost all the dynamic devices fabricated in CMOS are driven by the forces introduced by the thermal expansion effect [15, 17, 59, 89, 90]. Their performance is greatly limited by the heat transfer mechanism of the structures. The work in this thesis breaks new ground by presenting the method of magnetic actuation in the construction of the CMOS dynamic devices for the first time. The Lorentz force, generated by the interaction between the current flowing through the structure and an external magnetic field, has excellent controllability with respect to its magnitude, direction and response speed. High quality movable devices are expected to be realized using magnetic actuation.

A deflectable mirror device is developed to demonstrate the operating principles of

magnetic actuation. The most challenging aspect of this work involves achieving a usable mirror deflection with reasonable current and magnetic field intensity: the analytic model indicates that, for a simple cantilever structure (Figure 5.7), the mirror deflection angle is about 0.033° with the input current of 10 mA and the external magnetic field of 0.1 T. To enhance the deflection, a cantilever-in-cantilever (CIC) structure is developed. The metal1 and metal2 layers of the CMOS process are used to conduct current around the structure so that the Lorentz forces on the ends of the cantilevers apply a couple resulting in a tilt of the mirror plate. Analytic calculations have pointed out that the deflection angle of the mirror plate is the accumulation of the tilts of all the surrounding cantilevers. The more embedded cantilevers there are, the more the angular deflection. For a triple CIC structure (containing three active cantilevers), the deflection angle of the central cantilever is more than 10 times as large as that of one simple cantilever if the operating conditions and the structure dimensions are the same.

Triple and double CIC structures with a mirror plate as the central cantilever have been fabricated using the CMOS 1.2 μm process offered by Northern Telecom. Both static and dynamic response of the devices were measured using a method of optical reflection. The measured static response shows a good agreement with the predictions of the analytic model. About 2.6° of the mirror tilt has been obtained for the triple CIC device under a current of 26 mA and a magnetic field of 0.12 T. The measured response time of the triple CIC device is approximately 28 μs . The frequency responses of the devices were also measured. The triple CIC device has a resonant frequency of 17 kHz and the double 25.3 kHz. The maximum tilt at the resonance is approximately 25° for the triple CIC and 18° for the double. The measured Q factors for the triple and double CIC structures are 35 and 90 respectively. The triple CIC device has been operated at resonance under a driving current of 8 mA continuously for 17 days (2.5×10^{10} oscillations).

No visible structural defects and no change in the deflection characteristics were observed afterward.

The novel design and activation technique makes the CIC structure an important entry into the field of CMOS micromachined dynamic devices. This work has demonstrated the successful fabrication of deflectable devices, using the standard CMOS process, capable of a highly controllable deflection angle in either direction, a large deflection angle, especially at resonance, a fast time response, and excellent mechanical stability.

6.2 Future Work

Although the standard CMOS micromachining technology has existed for almost a decade, it seems apparent that the commercialization of this technology is still at the preliminary stage. A main reason, in author's opinion, is the contradictory needs and interests between MEMS research groups and the standard IC process developers. For example, the TCR of the polysilicon resistor of the CMOS process has been minimized to improve the performance stability of the IC under a harsh operating environment. A sensor designer would like a high TCR to enhance the sensitivity. In this regard, magnetically actuated devices are more attractive than the thermally sensitive structures. For a dynamic structure driven by Lorentz forces, the mechanical properties of the thin films, the reduction of the residual stresses, and the current capability of the metal leads will be the key factors determining the performance of the device. All of these are well within the interests of an IC process developer.

The drawback of magnetic actuation is the need for a strong external magnetic field. There are at least two possible approaches to this problem:

1. Reduce the free space of the magnet. The free space between the two poles of the magnet used in the experiment is about 35 mm. The necessary free space should be big enough to contain a die which is approximately $3 \times 3 \text{ mm}^2$ in size. It is usually much easier to generate a strong magnetic field in a small free space.
2. Optimize the structure performance. None of the fabricated devices is designed for optimum performance and a number of obvious improvements could be incorporated to make the deflection larger. As indicated by the analysis in Chapter 5, embedding more active cantilevers or reducing the thickness of the support arms or doing both would dramatically enhance the deflection.

Magnetically actuated devices have also offered an excellent opportunity to investigate the piezoresistive characteristics of the polysilicon resistor. In combination with the optical reflection method, one would be able to determine the static deflection, the response time and the frequency response by measuring the resistance of the polysilicon resistor embedded in the structures. Those measurements would provide the basis for the applications as resonator sensors.

Bibliography

- [1] J.B. Angell, S.C. Terry and P.W. Barth. Silicon Micromechanical Devices, Scientific American, April 1983, pp. 44-55.
- [2] Ljubisa Ristic (editor). Sensor Technology and Devices. Ariech House. Norwood, 1994.
- [3] Kurt E. Petersen, Silicon as a Mechanical Material, Proc. IEEE. Vol. 70, no. 5, pp. 420-457, May 1982.
- [4] H.C. Nathanson, W.E. Newell, R.A. Wickstrom and J.R. Davis, Jr., The Resonant Gate Transistor, IEEE Trans. Electron Dev., Vol. ED-14. 1967. pp. 117-121.
- [5] Y.C. Tai and R.S. Muller, Pin Joints, Gears, Springs, Cranks, and Other Novel Micromechanical Structures, Tech. Digest, Transducers '87, 1987, p.853.
- [6] W.S.N. Trimmer and M. Mehregany, Microgears and Turbines Etched from Silicon. Tech. Digest, Transducers '87, 1987. p.853.
- [7] M. Parameswaran, H.P. Baltes and A.M. Robinson, Polysilicon Microbridge Fabrication Using Standard CMOS Technology, Digest of Technical Papers, IEEE Solid-State Sensors and Actuators Workshop, Hilton Head Island, June 1988, pp. 148-150.

- [8] M. Parameswaran. *Microelectronic and Micromechanical Sensors and Actuators in CMOS Technology*. Ph.D.. Thesis. University of Alberta, Canada, 1990.
- [9] M. Parameswaran, H.P. Baltes, Lj. Ristic, A.C. Dhaded, and A.M. Robinson. *A New Approach for the Fabrication of Micromachined Structures*. *Sensors and Actuators*, Vol. 19, pp. 289-307, 1989
- [10] Lj. Ristic, *CMOS Technology: A Base for Micromachining*, *Microelectronic J.*, Vol. 20, 1989, p.153.
- [11] J. W. Gardner, *Microsensors—Principles and Applications*. John Wiley & Sons, Chichester, 1994.
- [12] M. Parameswaran, A.M. Robinson, Lj. Ristic, K. Chau and W. Allegretto. *A CMOS Thermally Isolated Gas Flow Sensor*, *Sensors and Material*, Vol. 2, 1990. p.17.
- [13] M. Parameswaran, Lj. Ristic, A.C. Dhaded and H.P. Baltes, *Sandwiched Oxide Cantilever Beams in Standard CMOS Technology*, *Proc. Canadian Conf. on Electrical and Comp. Eng.*, Vancouver, 1988, p. 781.
- [14] M. Parameswaran, Lj. Ristic, A.C. Dhaded and H.P. Baltes. *Fabrication of Microbridges in Standard Complementary Metal Oxide Semiconductor Technology*, *Can. J. Phys.*, Vol. 67, 1989, p.184.
- [15] M. Parameswaran, Lj. Ristic, A.M. Robinson, K. Chau, and W. Allegretto. *Electrothermal Microactuators in Standard CMOS Process*, *Sensors and Materials*, Vol.2, 1990, p. 197.
- [16] M. Paranjape, *Vertical Hall Magnetic Field Microsensor Development and Implementation in CMOS Technology*, Ph.D., Thesis, University of Alberta, Canada, 1993.

- [17] O. Brand, H. Baltés and U. Baldenweg, Thermally Excited Silicon Oxide Beam and Bridge Resonators in CMOS Technology, IEEE. Trans. on Electron. Devices, Vol. 40, No. 10, October 1993.
- [18] M. Parameswaran and M. Paranjape, Layout Design Rules for Microstructure Fabrication Using Commercially Available CMOS Technology. Sensors and Materials, Vol. 5, No. 2 (1993) 113-123.
- [19] K.D. Bean, Anisotropic Etching of Silicon, IEEE Trans. Electron. Devices. Vol. ED-25, 1978, p.1185.
- [20] M.P. Wu, Q.H. Wu and W.H. Ko, A Study on Deep Etching of Silicon Using Ethylenediamine-Pyrocatechol-Water, Sensors and Actuators, Vol. 9, 1986, p.333.
- [21] U. Schnakenberg, W. Benecke and P. Lange, Digest of Technical Papers. Transducer '91, IEEE Int. Conf. on Solid-State Sensors and Actuators (Transducers '91), 1991. p.815.
- [22] Omega Complete Temperature Measurement Handbook and Encyclopedia, Vol. 26. Stamford, CT, Omega Engineering Inc., 1989. pp. U-1-24.
- [23] T.C. Verster. The Silicon Transistor as a Temperature Sensor, Temperature, Its Measurement and Control in Science and Industry. Vol. 4, ed. H.H. Plumb. Pittsburgh, ISA, pp. 1125-1134.
- [24] E.A. Vittoz, MOS Transistors Operated in the Lateral Bipolar Mode and Their Application in CMOS Technology, IEEE. J. Solid-State Circuits, Vol. SC-18, 1983. pp. 273-279.
- [25] M.G.R. Degrauwe. CMOS Voltage Reference Using Lateral Bipolar Transistors, IEEE J. Solid-State Circuits, Vol. SC-20, 1985, pp. 1151-1157.

- [26] P. Krummenacher and H. Oguey, Smart Temperature Sensor in CMOS Technology. Sensors and Actuators, Vols. A21-A23, 1990, pp. 636-638.
- [27] J.Y. Zhu, W. Rasmussen, S. Richard and D. Cheeke, Ultrastable Integrated CMOS Oscillator, Int. J. Electronics, Vol. 70, 1991, pp. 433-441.
- [28] Neil H.E. Weste and Kamran Eshraghian, Principles of CMOS VLSI Design, Addison-Wesley, Massachusetts, 1985.
- [29] J.Y.W. Seto, The Electrical Properties of Polycrystalline Silicon Films, J. Appl. Phys., Vol. 46, 1975, pp. 5247-5254.
- [30] N.C.C. Lu, L. Gerzberg, C.Y. Lu and J.D. Meindl, Modeling and Optimization of Monolithic Polycrystalline Silicon Resistors, IEEE Trans. Electron. Dev., Vol. ED-28, 1981, pp. 818-830.
- [31] E. Obermeir, P. Kopystynski and R. Niessl, Characteristics of Polysilicon layers and Their Application to Sensors, IEEE Solid-State Sensor Workshop, Hilton Head Is., SC, 1986.
- [32] A.M. Robinson, Mitel 1.5 μm CMOS Process: Characterization Measurements of the Polysilicon Layers for Use in a Microsensor, Report IC95-05, Canadian Microelectronics Corporation, Kingston, Ont., 1995.
- [33] R.R. Schatz, Temperature Coefficient of Resistance of Polysilicon Microresistors, Report of Summer Research (unpublished), Electrical Engineering Department, University of Alberta, 1994.
- [34] D. Jaeggi, H. Baltes and D. Moser, Thermoelectric AC Power Sensor by CMOS Technology, IEEE Electron Device Lett., EDL-13, pp.366-368, 1992.
- [35] R. Lenggenhager, H. Baltes, J. Peer and M. Forster, Thermoelectric Infrared Sensors by CMOS Technology, IEEE Electron Device Lett., EDL-13, pp.454-456, 1992.

- [36] A.M. Robinson, P. Haswell, R.P.W. Lawson and M. Parameswaran, A Thermal Conductivity Microstructural Pressure Sensor Fabricated in Standard Complementary Metal-Oxide Semiconductor, *Rev. Sci. Instrum.* 63 (3), pp. 2026-2029, 1992.
- [37] W. Allegretto, B. Shen, P. Haswell, Z. Lai and A.M. Robinson, Numerical Modeling of a Micromachined Thermal Conductivity Pressure Sensor, *IEEE Tran. CAD IC Systems*, Vol.13, No.10, pp.1247-1256, October 1994.
- [38] C. Hu and S. Kim, Thin Film Dye Laser with Etched Cavity, *Appl. Phys. Lett.*, Vol. 29, 1976, pp.582-589.
- [39] N.R. Swart and A. Nathan, Design Optimisation of Integrated Microhotplates, *Sensors and Actuators A*, 43 (1994) 3-10.
- [40] M. Pirani, *Verh. Dtsch. Phys. Ges.* 8, 686 (1906)
- [41] R. Andrew Wood and Norman A. Foss, Night-vision Cameras Scan and Stare in the Dark, *Laser Focus World*, pp.101-103, June, 1993.
- [42] R. Lenggenhager, H. Baltes and T. Elbel, Thermoelectric Infrared Sensors in CMOS Technology, *Sensors and Actuators A*, 37-38 (1993) pp.216-220.
- [43] Y.P. Xu, R.S. Huang and G.A. Rigby, A Silicon-diode-based Infrared Thermal Detector Array, *Sensors and Actuators A*, 37-37 (1993) 226-230.
- [44] M. Parameswaran, A.M. Robinson, D.L. Blackburn, M. Gaitan and J. Geist. Micromachined Thermal Radiation Emitter from a Commercial CMOS Process, *IEEE Electron Devices Letters*, Vol.12, no.2, 1991, pp.57-59.
- [45] G.H. Chapman, M. Parameswaran and M.J. Syrzycki, A Wafer Scale Dynamic Thermal Scene Generator, 1992 *Proc. Int. Conf. on Wafer Scale Integration*, ed. V.K. Jain and P.W. Wyatt, San Francisco, CA, January 22-25, 1992, pp.300-309.

- [46] C.H. Mastrangelo, Thermal Applications of Microbridges, Ph.D. Thesis, University of California, Berkeley, 1991.
- [47] W. Allegretto, B. Shen, T. Kleckner, A.M. Robinson, Micromachined Polysilicon Power Dissipation: Simulation and Experiment, submitted for publication, July 1995.
- [48] J. Funk, G. Wachutka and H. Baltes, Scaling Laws for Optimized Design of Integrated Thermopiles, Proc. 7th Transducers '93, Yokohama, Japan, pp.742-745.
- [49] P. Haswell and A.M. Robinson, Constant Power Testing System for Polysilicon Microresistor Characterization Measurements, J. Meas. Sci. Technol. 4, 957-961 (1993).
- [50] A. Bejan, Convection Heat Transfer, Wiley-Interscience, New York, 1984.
- [51] H. Von Ubisch, On the Conduction of Heat in Rarefied Gases and Its Manometric Application, Appl. Sci. Res., Vol. A2, pp.364-430, 1951.
- [52] Herbert R. Philipp, The Infrared Optical Properties of SiO_2 and SiO_2 Layers on Silicon, J. Appl. Phys. 50(2), pp. 1053-1056, February 1979.
- [53] C.R. Wylie and L.C. Barrett, Advanced Engineering Mathematics, McGraw-Hill Book Co., New York, 1982, 5th Edition.
- [54] B. Shen, Zhongsheng Lai, A.M. Robinson and W. Allegretto, Thermal Response of CMOS-Micromachined Thermistor Sensors under Constant Power and Constant Current Excitation, Rev. Sci. Instrum. 65 (11), pp.3528-3534, November 1994.
- [55] B. Shen, P. Haswell, Z. Lai and A.M. Robinson, Thermal Response of a CMOS-Micromachined Thermistor Sensor, Proc. CCVLSI '93, Banff, November 1993, Canada, pp.781-787.

- [56] Z. Lai, B. Shen, P. Haswell and A.M. Robinson, Experimental Studies of the Thermal Response Time of the Micromachined Thermistor Sensor in Constant Power Mode, Proc. 7th Transducers '93, Yokohama, Japan, pp. 1004-1007.
- [57] S. Prescesky, M. Parameswaran, A. Rawicz, R.F.B. Turner and U. Reichl, Silicon Micromachining Technology for Sub-Nanogram Discrete Mass Resonant Biosensors, Can. J. Phys. 70, 1178-1183 (1992).
- [58] J.M. Chen and M. Parameswaran, CMOS Micromachined Sub-nanogram Mass Sensor for In-liquid Biomass Measurement, Seventh Canadian Semiconductor Technology Conference, Ottawa, Canada, August 14-18, 1995.
- [59] I. Stiharu, L. Landsberger and M. Paranjape, Micromachined Sub-miniature Electro-thermal Actuator, Seventh Canadian Semiconductor Technology Conference, Ottawa, Canada, August 14-18, 1995.
- [60] D. Moser, O. Brand and H. Baltes, A CMOS Compatible Thermally Excited Silicon Oxide Beam Resonator with Aluminum Mirror, Tech. Digest, Transducers '91, IEEE, New York, 1991, pp. 547-550.
- [61] S. Bouwstra, R. Legtenberg, H.A.C. Tilmans and M. Elwenspoek, Resonating Microbridge Mass Flow Sensor, Sensors and Actuators. Vol. A21-A23, pp. 332-335, 1990.
- [62] T.S.J. Lammerink, M. Elwenspoek, R.H. van Ouwerkerk, S. Bouwstra and J.H.J. Fluitman, Performance of Thermally Excited Resonators, Sensors and Actuators, Vol. A21-A23, pp. 352-356, 1990.
- [63] T.S.J. Lammerink, M. Elwenspoek and J.H.J. Fluitman, Frequency Dependence of Thermal Excitation of Micromechanical Resonators, Sensors and Actuators, Vol. A25-A27, pp. 685-689, 1991.

- [64] T.S.J. Lammerink, M. Elwenspoek and J.H.J. Fluitman, Thermal Actuation of Clamped Silicon Microbeams, *Sensors and Materials*, Vol. 3,4, pp. 217-238, 1992.
- [65] K. Preston, Jr., An Array Optical Spatial Phase Modulator, *Proc. IEEE Int. Solid State Circuits Conf.*, Institute of Electrical and Electronics Engineers, New York, 1968, p.100.
- [66] J.A. van Raalte, A New Schlieren Light Valve for Television Projection, *Appl. Opt.*, 9 (1970), pp. 2225-2230.
- [67] R.N. Thomas, J. Guldberg, H.C. Nathanson and P.R. Malmberg, The Mirror-matrix Tube: a Novel Light Valve for Projection Displays, *IEEE Trans. Electron Devices*, ED-22 (1975), pp. 765-775.
- [68] K.E. Petersen, Micromechanical Light Modulator Array Fabricated on Silicon, *Appl. Phys. Lett.*, 31 (1977), pp. 521-523.
- [69] K.E. Petersen, Silicon Torsional Scanning Mirror, *IBM J. Res. Dev.*, 24 (1980), pp. 631-637.
- [70] Mikromechanik verlängert Lebensdauer. *Markt & Technik*, 15 (1992), pp. 47-48.
- [71] J.B. Sampsel, An Overview of Texas Instruments Digital Micromirror Device (DMD) and Its Application to Projection Displays, *Society for Information Display Internatl. Symposium Digest of Tech. Papers*, Vol. XXIV, pp. 1012-1015, May 1993.
- [72] J.B. Sampsel, The Digital Micromirror Device and Its Application to Projection Displays, *Tech. Digest, 7th Int. Conf. Solid-State Sensors and Actuators (Transducers '93)*, Yokohama, Japan, June 7-10, 1993. pp. 24-27.

- [73] J.M. Younse and D.W. Monk, The Digital Micromirror Device (DMD) and Its Transition to HDTV, Proc. of 13th International Display Research Conf. (Late News Papers), pp. 613-616, August 31 - September 3, 1993.
- [74] V.P. Jaccklin, C. Linder and N.F. de Rooij, Line-Addressable Torsional Micromirrors for Light Modulator Arrays, Sensors and Actuators A, 41-42 (1994) 324-329.
- [75] H. Toshiyoshi, H. Fujita, T. Kawai and T. Ueda, Piezoelectrically Operated Actuators by Quartz Micromachining for Optical Application, Tech. Digest, IEEE MEMS Workshop, Fort Lauderdale, FL, USA, Feb. 1993, pp. 133-138.
- [76] O. Tabata, R. Asashi, N. Fujitsuka, M. Kimura and S. Sugiyama, Electrostatic Driven Optical Chopper Using SOI Wafer, Tech. Digest, 7th Int. Conf. Solid-State Sensors and Actuators (Transducers '93). Yokohama, Japan, June 7-10. 1993, pp. 124-127.
- [77] J.H. Herman and D.J. Clift, Miniature Fabry-Perot Interferometers Micromachined in Silicon for Use in Optical Fiber WDM Systems, Tech. Digest, 6th Int. Conf. Solid-State Sensors and Actuators (Transducers '91), San Francisco, CA, USA, June 1991. pp. 372-375.
- [78] K. Aratani, P.J. French, P.M. Sarro, R.F. Wolffenbuttel and S. Middlehoek, Process and Design Considerations for Surface Micromachined Beams for a Tuneable Interferometer Array in Silicon, Tech. Digest, IEEE MEMS Workshop, Fort Lauderdale, FL, USA, Feb. 1993, pp. 230-235.
- [79] N.F. Raley, D.R. Ciarlo, J.C. Koo, B. Beiriger, J. Trujillo, C. Yu, G. Loomis and R. Chow, A Fabry-Perot Microinterferometer for Visible Wavelengths, Proc. IEEE Solid-State Sensors and Actuators Workshop, Hilton Head Island, SC, USA, 1992, pp. 170-173.

- [80] O. Solgaard, F.S.A. Sandejas and D.M. Bloom, Deformable Grating Optical Modulator, *Opt. Lett.*, 17 (1992), pp. 688-690.
- [81] K. Gustafsson and B. Hök, A Silicon Light Modulator, *J. Phys. E: Sci. Instrum.*, 21 (1988) 680-685.
- [82] R.A. Buser, N.F. de Rooij, H. Tischhauser, A. Domman and G. Stauffert, Biaxial Scanning Mirror Activated by Bimorph Structures for Medical Applications, *Sensors and Actuators A*, 31 (1992) 29-34.
- [83] K.E. Mattsson, Surface Micromachined Scanning Mirrors, *Microelectron. Eng.*, 19 (1992) 199-204.
- [84] E. Obermeier, J. Lin and V. Schlichting, Design and Fabrication of an Electrostatically Driven Microshutter, *Tech. Digest, 7th Int. Conf. Solid-State Sensors and Actuators (Transducers '93)*, Yokohama, Japan, June 7-10, 1993, pp. 132-135.
- [85] J. Mohr, M. Kohl and W. Menz, Micro-optical Switching by Electrostatic Linear Actuators with Large Displacements, *Tech. Digest, 7th Int. Conf. Solid-State Sensors and Actuators (Transducers '93)*, Yokohama, Japan, June 7-10, 1993, pp. 120-123.
- [86] K. Gustafsson and B. Hök, Fiberoptic Switching and Multiplexing with a Micromechanical Scanning mirror, *Tech. Digest, 5th Int. Conf. Solid-State Sensors and Actuators (Transducers '89)*, Montreux, Switzerland, June 25-30, 1987, pp. 212-215.
- [87] T.G. MacDonald, R.M. Boysel and J.B. Sampsel, 4×4 Fiber Optic Crossbar Switch Using the Deformable Mirror Device, *Tech. Digest on Spatial Light Modulators and Applications 1990*, Vol. 14, Optical Society of America, Washington, DC, 1990, pp. 80-83.

- [88] R.W. Cohn, Link Analysis of a Deformable Mirror Device Based Optical Crossbar Switch, *Opt. Eng.*, 31 (1992) 134-140.
- [89] B. Shen and A.M. Robinson, Thermally Activated Mirror Array Built in CMOS Process, Mitel Technique Briefing, University of Alberta, Edmonton, Canada, August 1994.
- [90] J. Bühler, J. Funk, O. Paul, F.-P. Steiner, H. Baltes, Thermally Actuated CMOS Micromirrors, *Sensors and Actuators A* 46-47 (1995) 572-575.
- [91] J. Funk, J. Bühler, J.G. Korvink, H. Baltes, Thermomechanical Modeling of an Actuated Micromirror, *Sensors and Actuators A* 46-47 (1995) 632-636.
- [92] E. Allegretto and A.M. Robinson, Post-Processing and Characterization of Silicon Micromachined Devices, Summer Research Report, Electrical Engineering Department, University of Alberta, May-August, 1994.
- [93] F.P. Beer and E.R. Johnston, Jr., *Mechanics of Materials*, McGraw-Hill Ryerson, Toronto, 1985.
- [94] M. Faucherr, 1.5 μm CMOS Process Overview, Bromont, Quebec, Canada, February 1993.
- [95] R.W. Clough and J. Penzien, *Dynamics of Structures*, McGraw-Hill, New York, 1975.
- [96] Private conversation with Dr. T. Hrudehy.
- [97] D.D. Pollock, *Physics of Engineering Materials*, Prentice-Hall, New Jersey, 1990.
- [98] F.I. Chang, R. Yeh, G. Lin, P.B. Chu, E. Hoffman, E.J.J. Kruglick and K.S.J. Pister, Gas-phase Silicon Micromachining with Xenon Difluoride, SPIE 1995 Symposium on Micromachining and Microfabrication, October 1995.

- [99] E. Hoffman, B. Warneke, E. Kruglick, J. Weigold and K.S.J. Pister, 3D Structures with Piezoresistive Sensors in Standard CMOS, MEMS '95, Amsterdam, The Netherlands, December 1994.
- [100] E.J.J. Kruglick, S. Damle and K.S.J. Pister, Three-dimensional Structures for Micro-optical Mechanical Systems in Standard CMOS, SPIE 1995 Symposium on Micromachining and Microfabrication, October 1995.